Radiochromic film as a tool to study and validate a commercial Monte Carlo dose calculation algorithm for electron radiotherapy

A thesis submitted in fulfilment of the requirements for the degree of Master of Applied Science (Health and Medical Physics)

Eu-Jin Chan

B.Sc. (Applied Physics)

RMIT University

School of Applied Science

College of Science Engineering and Health

RMIT University

15 July 2016

DECLARATION

I certify that except where due acknowledgement has been made, the work is that of the author alone; the work has not been submitted previously, in whole or in part, to qualify for any other academic award; the content of the thesis is the result of work which has been carried out since the official commencement date of the approved research program; any editorial work, paid or unpaid, carried out by a third party is acknowledged; and, ethics procedures and guidelines have been followed.

Eu-Jin Chan

15/07/2016

ACKNOWLEDGEMENTS

I would like to express my deepest gratitude to my manager, Jenny Lydon, for her supervision, support and guidance on this project. She diligently helped me review every step in this thesis. Without Jenny's experience and passion, this project would not have been possible.

I would also like to thank my project supervisors Tomas Kron and Rick Franich for their continuous support and guidance. With their immense knowledge, they helped me in all the time of research and writing of this thesis. A special thanks to Rick for meticulously reviewing every sentence in this thesis.

I would also like to thank the experts who were involved this research project, Catherine Lawford, Francis Gibbons and Nicholas Hardcastle. Without their participation and input, the project could not have been successfully completed.

I must express my very profound gratitude to my parents for providing me with unfailing support and continuous encouragement throughout my years of study. Lastly, I would like to thank my fiancé for her support and having faith in everything I pursue. Your continuous encouragement has driven me to strive and achieve the highest.

This accomplishment would not have been possible without any one of the above. Thank you.

PUBLICATIONS AND PRESENTATIONS

This thesis has generated a publication in the Physics in Medicine and Biology journal and is listed below:

Chan E, Lydon J and Kron T 2015 "On the use of Gafchromic® EBT3 films for validating a commercial electron Monte Carlo dose calculation algorithm", Physics in medicine and biology, 60, 2091. http://dx.doi.org/10.1088/0031-9155/60/5/2091

Two presentations were accepted and presented at the Engineering and Physical Sciences in Medicine (EPSM) conference in 2012 and 2013.

1) Dr Jenny Lydon, Mr EuJin Chan, Mr Jim Cramb, Dr Fran Gibbons, Ms Catherine Lawford, "Clinical Implementation of a Commercial Electron Monte Carlo Algorithm", Engineering and Physical Sciences in Medicine Conference, Gold Coast, QLD, December 2012.
2) E.J.Chan, J. Lydon, T.Kron, "Comparison of measured and Monte Carlo depth doses for oblique incident electron beams", Engineering and Physical Sciences in Medicine Conference, Perth, WA, November 2013.

LIST OF TABLES

LIST OF FIGURES

TABLE OF CONTENTS

ABSTRACT

Radiotherapy is a type of cancer treatment to suppress tumour growth by employing ionising radiation. External beam radiation is the most common form of radiotherapy and uses ionising radiation such as photon and electron beams. Megavoltage electron beams can be used to treat relatively superficial tumours of less than 5 cm depth such as skin, scalp, chest walls, breast, and nodal boost. In the radiotherapy process, the treatment planning system plays an important role in simulating dose distributions in a patient that would be delivered by the treatment machine. Conventional planning algorithms are based on relatively simple beam models: beam profiles are measured in homogeneous media, and modified to approximate changes in field shape and media. Predicting dose becomes difficult with complex treatment geometries such as beam obliquity, small field sizes and tissue inhomogeneities. In these complex patient geometries, the Monte Carlo method is known to be the most accurate to calculate dose distributions. Recently an electron Monte Carlo (eMC) dose calculation algorithm has been incorporated in XiO treatment planning systems (Elekta/CMS XiO). This algorithm is based on the Voxel Monte Carlo (VMC) code which allows fast dose calculations in voxelised heterogeneous media. This study aims to evaluate XiO eMC's capability to accurately predict dose distribution. Simulations with the eMC module were performed for 6, 12 and 18 MeV beams in different beam setups. In addition to standard large uniform fields, the effects of oblique incidence, small field size and inhomogeneous media were investigated in this thesis. A new measuring method was developed for high resolution, absolute dose measurement of these non-standard irradiations using radiochromic film. A portable holder was designed and constructed to hold films vertically in a reproducible setup submerged in a water phantom. The film measurements were performed and compared to the calculated XiO eMC 2D dose distributions using the gamma dose analysis and distance-to-agreement tool from the SNC Patient software (Sun Nuclear Corporation, Melbourne, FL). All 2D comparisons of film and XiO eMC were done by comparing absolute dose per monitor unit (MU). The experimental film method was verified with ionisation chamber measurements and the total

uncertainty for the film measurement method was determined to be ±3% (2σ). In water beyond D_{max}, XiO electron Monte Carlo and EBT3 film agree to within the measurement uncertainties i.e. ± 3% or ± 2 mm for all standard, oblique and circular fields for measurements. Differences between XiO eMC and EBT3 film of up to 9% occur close to the surface for the oblique and circular fields. For the inhomogeneous media, agreement between XiO and film was also within the calculation and measurement uncertainties in the water and lung like regions. Within the rib phantom, XiO was up to 10% higher than film. By comparison, agreement between XiO and film within the denser skull phantom is within the uncertainties. This method has extended the standard set of commissioning measurements to include clinically relevant conditions that focus on specific geometries that are difficult or impossible to measure using ionisation chambers. Radiochromic film in water proved to be a convenient high spatial resolution method to verify electron dose distribution in non-standard conditions including inhomogeneous media.

INTRODUCTION

Treatment planning system (TPS) commissioning and validation is generally performed with ionisation chambers for standard geometry fields. However, an ionisation chamber becomes problematic when measuring complex geometries such as beam obliquity, small field sizes and tissue inhomogeneities. In these complex geometries, the Monte Carlo method is known to be the most accurate to calculate dose distributions. With the introduction of Monte Carlo being implemented in commercial treatment planning systems, the need to validate beam models after commissioning becomes essential. No single detector type is ideal for these measurements where both absolute dose and dose distributions can be determined at the same time. The purpose of this study is to evaluate the capacity of the TPS to accurately predict dose distributions in challenging complex treatment geometries. This work focuses on measurements in clinically relevant conditions that are not part of the standard commissioning measurements. The proposed method is using radiochromic film in water to provide full scatter conditions. A film holder was designed to accurately hold the film vertically below the water surface for reproducible set-up. The measurements are aimed at validating the planning system by direct 2D comparison for complex geometries including inhomogeneities such as lung and bone. This project will provide a better understanding of the ability of advanced Monte Carlo calculations to predict dose in complex radiotherapy treatment scenarios and give reassurance of dose predictions in these treatments.

1.1 Radiation Therapy

Radiotherapy is a type of cancer treatment to suppress tumour growth by employing ionising radiation. The main objective is to destroy tumour cells while sparing surrounding healthy tissue. The principle methods for administering radiotherapy are by external beam therapy and sealed-source therapy which is also known as Brachytherapy. External beam radiation is the most common form of radiotherapy and uses ionising radiation such as photon and electron beams (Williams and Thwaites, 2000). A linear accelerator is generally used to produce high energy

megavoltage X-rays and electron beams. Gamma-rays from a cobalt unit and low energy X-rays from a superficial machine may also be used in radiotherapy. Megavoltage X-rays can deeply penetrate tissues and are used to irradiate deep seated tumours. By combining multiple beam configuration and orientation, dose conformity within the tumour can be achieved.

Megavoltage electron beams on the other hand, can be used to treat relatively superficial tumours of less than 5 cm depth such as skin, scalp, chest walls, breast, and nodal boost (Podgorsak, 2010). Electron beams strongly interact with the medium they traverse, resulting in a shallow penetration depth, a steep dose fall-off and a high surface dose of between 75% to 95% of maximum dose (Khan, 2003). The depth dose of an electron beam has a short build-up region which reaches maximum at depth depending on energy and then the dose drops off steeply with increasing depth as illustrated in Figure 1.1.

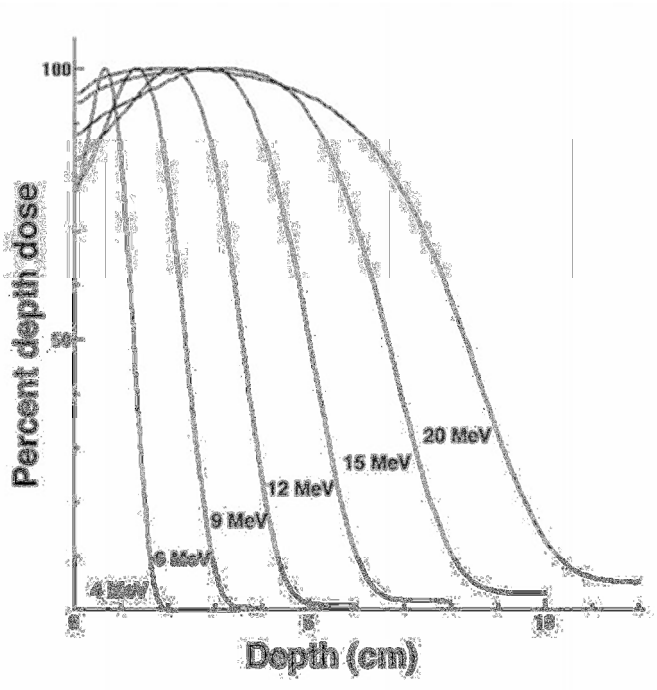

Figure 1.1 Relative depth dose curves for megavoltage electron beams over a range of energies. Figure reproduced from (Podgorsak, 2005).

1.2 Radiotherapy Treatment Process

Patients that require radiation therapy are prescribed a dose based on the type and stage of cancer. After diagnosis, a computed tomography (CT) scan is acquired to

locate the tumour. The CT slices generated from the scan will then be used in the treatment planning stage to generate a 3D model of the patient. A radiotherapy plan consists of the treatment technique, beam energy, number of fractions and duration of treatment. The treatment technique includes the planning target volume with beam weightings assigned to each of the beams. Surrounding organs at risk will also be taken into account by limiting the dose to these structures. A treatment planning system (TPS) calculates dose based on the Hounsfield unit or electron densities of materials that are predominant in radiotherapy such as tissue, bone, and muscle. The treatment plan will be optimised to conform around the target volume and the calculated dose distribution is displayed in a 3-dimensional reconstructed space.

After the planning stage, the treatment delivery accuracy needs to be verified. The delivery accuracy is divided into dosimetric and geometric accuracy. The accuracy of the calculated dose when compared to the beam delivery is known as the dosimetric accuracy. Geometric accuracy relates to patient positioning and immobilisation during treatment. A key component of the delivery of radiation therapy is the independent confirmation to ensure correct and accurate dose delivery (Stern *et al.*, 2011). The monitor unit (MU) setting determines the quantity of radiation delivered to the patient. A monitor unit validation program is generally used as an independent check to verify the MU generated from the TPS. For more complex cases such as Intensity Modulated Radiation Therapy (IMRT) or Volumetric Modulated Arc Therapy (VMAT), an independent quality assurance process that usually involves calculating and delivering the dose to a phantom or a 3D measuring device should be implemented.

During treatment, imaging aids such as Electronic Portal Imaging device (EPID) which uses the primary megavoltage beam or On-Board Imager (OBI) which has its own separate kilo-voltage source attached to the linear accelerator, are used to take images for validation and reproducibility of the treatment setup.

1.3 Treatment Planning Systems

In the radiotherapy process, TPS plays an important role in simulating dose distributions in a patient that would be delivered by the treatment machine.

Theoretical models of electron beams and the physics of beam interactions with matter are the basis of a TPS. The TPS uses analytical models to predict dose distributions using algorithms. Algorithms such as pencil beam (Cygler *et al.*, 1987; Hogstrom, 1985; Shiu and Hogstrom, 1991) and electron Monte Carlo (Ding *et al.*, 2006; Kawrakow *et al.*, 1996; Ma *et al.*, 2002; Ma *et al.*, 1999) are generally used to calculate electron dose distributions.

The Pencil Beam algorithm developed by Hogstrom et.al. (Hogstrom, 1985) has been the most common analytical model used for calculating dose distributions. Until recently, in the Pencil Beam algorithm, the dose distribution is modelled from a collection of forward-directed pencil beam shaped distributions. Due to its simplistic dose calculation algorithm, the kernels are scaled only in the depth direction as the beam travels through regions with different densities. This is valid if the medium consists of water or tissue equivalent densities. Due to the simplifications and approximations used in Pencil Beam algorithm, greater errors are expected in the presence of inhomogeneous media.

Monte Carlo (MC) modelling is considered to be the most accurate approach to modelling the electron beams interacting with matter (Andreo, 1991; Rogers, 1991). This method works on statistical probabilities and models a very large number of particles moving through matter. However, in the past, Monte Carlo was restricted by computational power. MC is made available and commercialised today due to the advancement in computer technology, as well as improvements in the implementation of the MC dose calculation algorithms.

1.4 Current Limitations

Electron radiotherapy is an important modality for cancer treatment. However, electron beams continuously lose energy as they penetrate tissue and as such change their interaction properties with matter. The primary interactions for electrons in the energy range below 50 MeV are collisions with bound atomic electrons, bremsstrahlung or radiative losses and elastic scattering. The consequences of these interactions are energy loss, change in direction and transfer of energy to matter which results in energy absorption and dose deposition. Due to

lateral scatter approximations, this has caused difficulty in predicting dose distributions using conventional dose calculation algorithms (Hogstrom *et al.*, 1981). Large discrepancies of 10% or more have been observed between the Pencil Beam dose calculation algorithm and measurements in inhomogeneous phantoms (Cygler *et al.*, 1987). This is due to the inappropriate treatment of electron transport in inhomogeneous media such as air cavities and bone. The need for accurate dose calculation is crucial to improve the calculated dose distributions in treatment planning systems. In complex patient geometries, the Monte Carlo method is considered to be the most accurate approach for electron dose calculations under all circumstances (Andreo, 1991). Monte Carlo simulation can model electron scattering in inhomogeneous medium more accurately than any analytical dose models (Jiang *et al.*, 2000).

Our institution recently purchased a commercial electron Monte Carlo (eMC) treatment planning system (Elekta/CMS XiO). The XiO eMC algorithm is based on the Voxel Monte Carlo (VMC) model which was modified to accommodate vendor specific features (Kawrakow *et al.*, 1996). The commissioning procedure for a Monte Carlo treatment planning system can be divided into two components; beam data acquisition for beam modelling and the validation of the calculated dose distributions. Measured data such as depth doses, profiles and output factors will be needed to create the beam model. The beam models created for XiO eMC are exclusive to the linear accelerator that is being modelled. There are several reports recommending the scope and content of commissioning and quality assurance for clinical radiotherapy treatment planning systems (Fraass *et al.*, 1998; IAEA, 2004; Mayles *et al.*, 1999). For clinical electron beam dosimetry, it is recommended that beam data measurements are done using cylindrical and plane-parallel ion chambers in a water, or water equivalent phantom (Gerbi *et al.*, 2009).These ionisation chambers require ionisation-to-dose conversion factors such as stopping-power ratios and perturbation factors to determine the dose. One disadvantage is that these conversion factors depend strongly upon electron energy and depth in phantom. This is due to the changes in energy spectra at various depths and the strong energy dependence of the water to air stopping power ratios. The ionisation-to-dose conversion factors inherently introduce uncertainty in the absorbed dose.

Other disadvantages of using ionisation chambers in electron beams include the lack of absorbed dose-to-water calibration factor by the national standards laboratory, the difficulty in water proofing the chamber and eliminating the impact of water pressure on the thin window of plane-parallel chambers.

Patient dose distributions can also differ significantly to those in a flat water phantom due mainly to the effects of oblique incidence, small fields and tissue heterogeneities. Basic electron beam data acquired for the treatment planning systems are applicable to normally incident beams on water or water equivalent homogeneous media. In reality, real patients have curved surfaces and are not very homogeneous. These factors influence the changes in electron scattering, beam penetration and interface effects (Khan *et al.*, 1991). As a result, the treatment planning system does not provide an accurate representation of the calculated dose distributions.

1.5 Thesis Objective

The need to validate the electron Monte Carlo dose calculations in conditions other than the standard measurements for normally incident beam and homogeneous media remains a challenging task to perform. Despite the difficulties, ionisation chambers are recommended for dose measurement because they are portable, easy to use and highly reproducible (Khan *et al.*, 1991). However, for measurements of non-standard fields, ionisation chambers can be problematic. In regions with large dose gradients, spatial resolution is limited by the physical size of the ionisation cavity. For small field sizes, the lack of charged particle equilibrium becomes an issue because Bragg-Gray cavity theory conditions are not valid and therefore the interpretation of ionisation chamber output in terms of dose is difficult. The aim of the study is to develop radiochromic film as an alternative to ionisation chambers for high resolution measurement of dose for non-standard beam geometries. The focus is to extend the standard set of treatment planning system commissioning measurements to include clinically relevant conditions. A procedure for interpreting the results was developed to analyse and compare depth dose profiles and 2-D dose distributions between eMC calculations and film measurements.

BACKGROUND

This chapter mainly focuses on the theoretical foundation of electron interactions and properties in radiation therapy, the Monte Carlo dose calculation algorithm, and radiochromic film. The justification of the project and experimental approach is also discussed with a brief review of the most relevant references or journal articles.

2.1 Electron interactions with matter

When an electron traverses matter, it interacts with the atomic orbital electrons and nuclei by Coulomb interactions which will result in energy loss and scattering. The important interactions between electrons and matter are:

a) Inelastic collisions with orbital electrons (ionisation or excitations)
b) Inelastic collisions with nuclei (Bremsstrahlung)
c) Elastic collisions with orbital electrons (Coulomb scattering)
d) Elastic collisions with nuclei

Energy losses from inelastic electron interactions can be classified into two processes; collisional and radiative losses. Collisional losses involve interactions with orbital electron and a radiative loss results from interactions with atomic nuclei as illustrated in figure 2.1. When an incident electron collides with an orbital electron, ionisation or excitation happens. When ionisation happens, the orbital electron is ejected from the absorber atom creating an ion pair (Podgorsak, 2005). Each time the incident electron ionises an atom, it loses a small amount of energy. However, if the energy is not sufficient to eject an electron from the atom, it is used to raise the orbital electron to a higher-energy state (Khan, 2010). This process is termed excitation. Both excitations and ionisations are part of collisional energy loss.

Radiative losses occur when an incident electron interacts with the nucleus of the absorber atom. The electron would scatter and changes trajectory with a loss in energy. This energy loss is emitted as a photon known as Bremsstrahlung. Occasionally, the passing electron may cause an electron to be ejected from a shell resulting in characteristic X-rays being emitted when an outer shell electron takes its place.

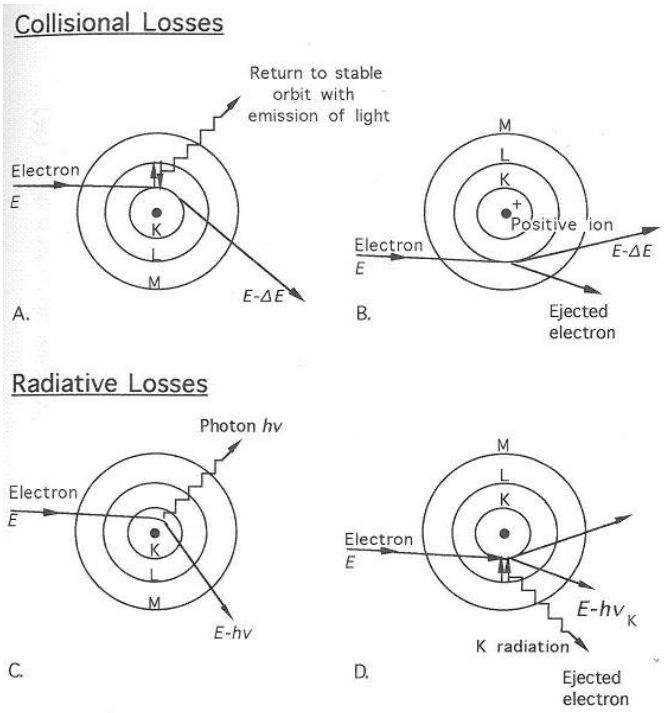

Figure 2.1 Electron interaction process a) excitation, b) ionisation, c) Bremsstrahlung production and d) characteristic radiation. Figure reproduced from (Klevenhagen, 1993).

Elastic collisions are interactions that result in no energy transfer from the incident electron to the orbital electron. The trajectory of the electron is altered by the presence of the orbital electron without the loss of kinetic energy. If the incident electron undergoes an elastic collision with a nucleus, the electron will be deflected towards the nucleus. In the case of an elastic interaction with an orbital electron, the incident electron will be deflected away from the orbital electron. Figure 2.2 shows the interactions between an electron and the nucleus of the absorber medium.

While photon interacts with matter via photoelectric, Compton and pair production processes, charged particle interact by direct ionisation. This occurs if the charged particles have sufficient kinetic energy to produce ionisation as they traverse through matter (Khan, 2010). As the incident electron penetrates through the medium, the energy is lost along the ionisation track. Occasionally, during the interaction process, the ejected electron contains sufficient energy to produce a secondary ionisation track of its own (Khan, 2010). This is also known as a δ ray. As the electrons travel deeper in the medium, the energy is degraded until they reach thermal energies and are then captured by the surrounding atoms (Khan, 2010).

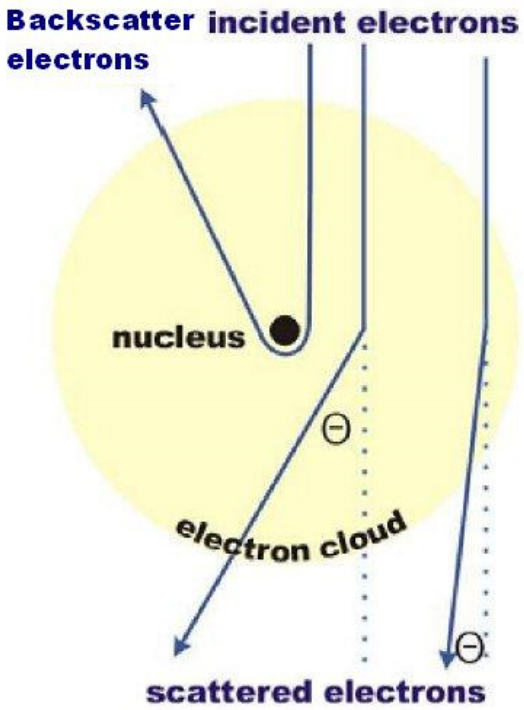

Figure 2.2 Elastic collisions resulting in electrons being deflected from its initial trajectory. Figure reproduced from (Krumeich, 2015).

2.2 Radiotherapy with electron beams

Electron beams that are used clinically are produced from a linear accelerator that uses high frequency electromagnetic waves to accelerate electrons to higher energies. Electrons generated from an electron gun are injected into a waveguide which consists of a series of microwave cavities. Microwaves that are fed into the cavities are generated by a klystron. As the electrons travel through the waveguide, electrons gain energy as they are accelerated through each cavity due to its electric field. As a result, a pencil beam of about 3mm wide exits the waveguide.

Most modern linear accelerators use a bending magnet to ensure that the beam is mono-energetic. A 270 degree bending magnet is generally used to refocus all the electrons to a desired position to maintain a small virtual spot size. An energy slit embedded in the bending magnet is designed to remove electrons that are not within 3% of the nominal peak of the selected electron energy (Zhang *et al.*, 2009). On exiting the bending magnet, the electron beam then strikes an electron scattering foil which spreads the beam and produces uniform electron fluence. After being

scattered by the scattering foil, the beam passes through a monitor chamber which is responsible for monitoring dose rate and beam flatness (Podgorsak, 2005). The electron beam then needs to be collimated multiple times before achieving a flat and symmetrical beam with a well-defined penumbra. It is necessary to further collimate the electron beam beyond the secondary collimators because electrons will increase in angular spread due to scatter as they traverse through air. This is done by attaching an electron applicator together with a shaping aperture at the end. A cross section of the treatment head is shown in figure 2.3.

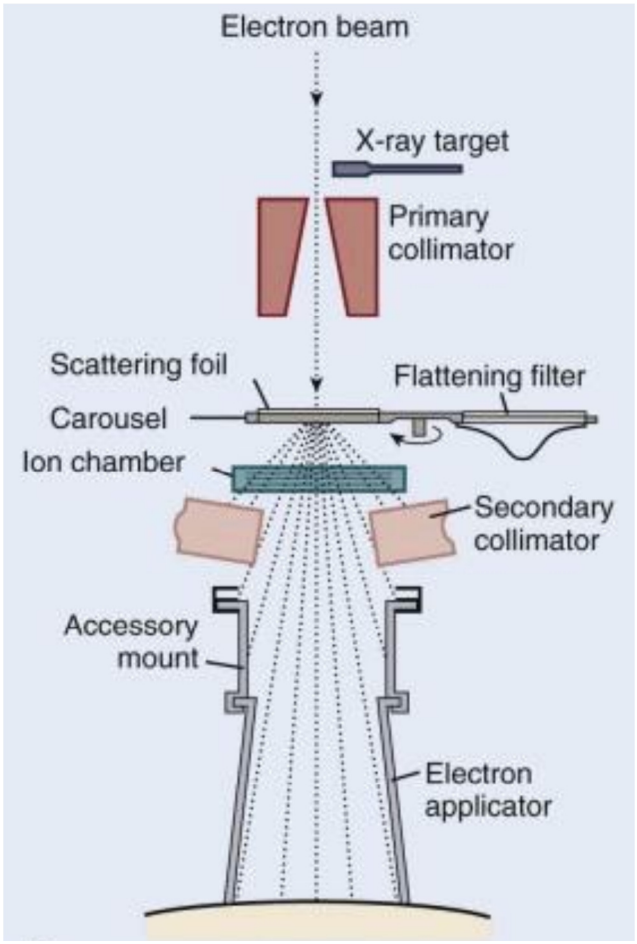

Figure 2.3 Schematic of a linear accelerator treatment head in electron mode. Figure reproduced from (Khan, 2003).

2.3 Electron beam properties

2.3.1 Variation of dose with depth

Electron beams have characteristic variations of dose with depth in water. This is also known as the depth dose curve which is shown in figure 2.4. All beam energies display a similar feature, starting with a dose build up to maximum dose followed by a rapid drop off until it levels off at a low dose which is called the Bremsstrahlung tail (Podgorsak, 2005). As the energy increases, the curve extends further into the medium but the gradient of the drop off is not as steep as the lower energies. This is due to the scattering power being greater at lower energies and at higher beam energies will be less scattered and more forward directed. To characterise an electron beam, the dose parameters used are surface dose, depth of dose maximum (D_{max}), R_{90} and R_{80} which are depths in water at 90% and 80% of the dose maximum, R_{50} which is also used to define the beam quality, practical range (R_p) and the Bremmstrahlung tail which is the X-ray component of the beam. Figure 2.5 illustrates the definition of the parameters. R_{90}, the depth of the 90% dose is also known as the therapeutic range is the most useful treatment depth clinically as dose is often prescribed to that isodose line. Energy choice for electron beams is critical in treatment planning. The dose decreases rapidly beyond the 90% dose level. R_{50}, the depth at 50% dose level is used as a measure of the beam's quality index (IAEA, 2000).

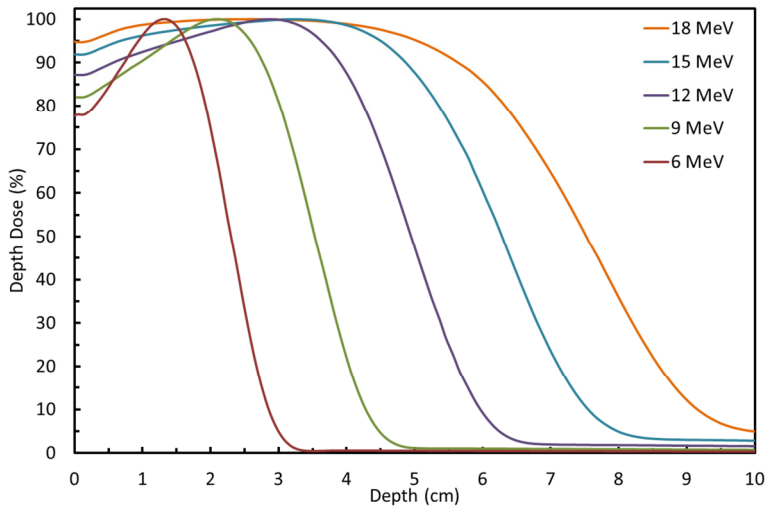

Figure 2.4 Percentage depth dose for electron energy ranging from 6-18 MeV in water at SSD of 100 cm in a 10x10 cm^2 applicator.

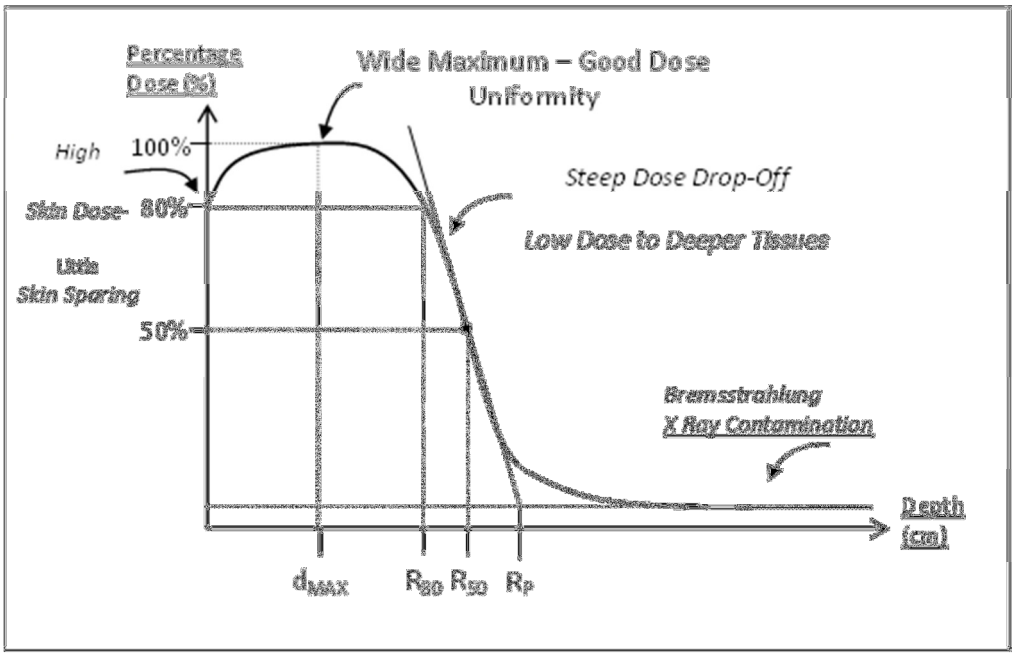

Figure 2.5 Characteristic parameters of the percentage depth dose in water.

2.3.2 Beam energy

Electron beam energy varies as a function of depth. Due to the complexity of the energy spectrum, there is no single energy parameter that will characterise an electron beam. There are several parameters used to describe an electron beam, such as the most probable energy ($E_{p,0}$) on the phantom surface, the mean energy ($\bar{E}_0$), and R_{50}. The most probable energy is related to the practical range (R_p) and its described by the relationship (Paul *et al.*, 1985)

$$E_{p,0} = 0.22 + 1.98R_p + 0.0025R_p^2 \ (MeV) \qquad 2.1$$

As recommended by TG-21 protocol (Paul *et al.*, 1985), the mean energy ($\bar{E}_0$) is related to R_{50} and is described as

$$\bar{E}_0 = 2.33R_{50} \qquad 2.2$$

The mean energy and most probable energy of electrons at a phantom surface are generally used to determine energy dependent parameters such as the stopping-power ratios and the electron fluence correction factors.

2.3.3 Dose in build-up region

Electrons are scattered easily with larger angles at lower energies which causes dose build-up to be rapid over short distances (Khan, 2010). The surface doses for electron beams are typically 80 to 90% of D_{max} dose and increases with increasing electron energy. This differs from photon beams where surface dose decreases with increasing energy and is typically 20% to 30% of D_{max} dose.

2.3.4 Bremsstrahlung contamination

The dose distribution beyond D_{max} has a sharp drop-off and it is due to scattering and continuous energy loss. The low dose tail of the depth dose curve is attributed to Bremsstrahlung produced in the head of the accelerator, in air between the accelerator head and the patient, and in the irradiated medium. The Bremsstrahlung contamination increases with increasing electron energy and is typically in the range of 0.5% to 4%.

2.3.5 Effective source position

Unlike photon beams where the source position is located at the X-ray target, electron beams generated from a linear accelerator appear to originate from an effective source located close to the scattering foils. The location of the effective source is known as the effective, or virtual, source position. The distance between the isocentre of the linear accelerator to the effective source position is known as the effective source-to-surface distance (SSD_{eff}). The position of the effective source determined geometrically will differ from the position derived dosimetrically. There are various methods to determine SSD_{eff}. The commonly used method to derive SSD_{eff} dosimetrically is to measure dose at various distances from the electron applicator by varying the gap between the phantom surface and the applicator (Podgorsak, 2005).

2.3.6 Field size

To determine the radiation width of a beam profile, RW_{50} (Figure 2.6), defined as the width of the profile at half its maximum intensity compared to the intensity value at the beam axis (NCS, 1996), is used.

The field size dependence of the depth dose curve is very low if the field size is large enough to provide lateral scatter equilibrium. However, when the field size decreases to less than the lateral range of secondary scattered electrons, the shape of the depth dose curve is altered. As the field size decreases, the dose gradient is less steep and the depth of D_{max} shifts towards the surface (Khan, 2010). Figure 2.7 shows the variation of the depth dose curve with varying field diameter. Therefore, as a general rule of thumb, the minimum electron field size for lateral scatter equilibrium at central axis is approximated to be E (MeV)/2.5 (cm). For irregular field sizes, the depth dose curve is shown to be very similar to equivalent circular field sizes (Khan, 2003).

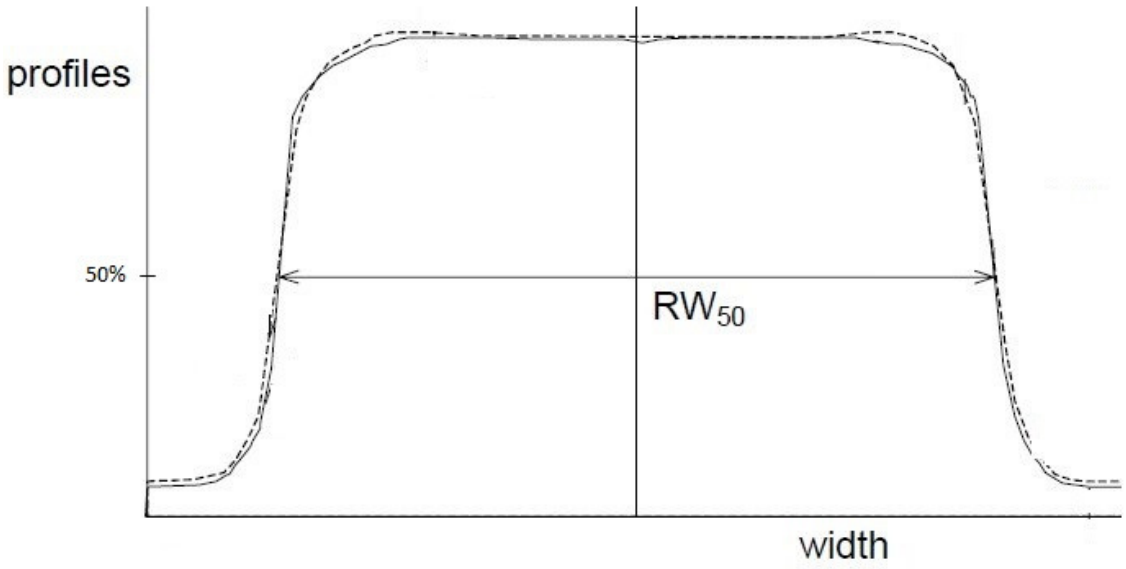

Figure 2.6 Radiation width (RW_{50}) of a beam profile defined at the 50% of the central axis dose. Figure reproduced from (NCS, 1996).

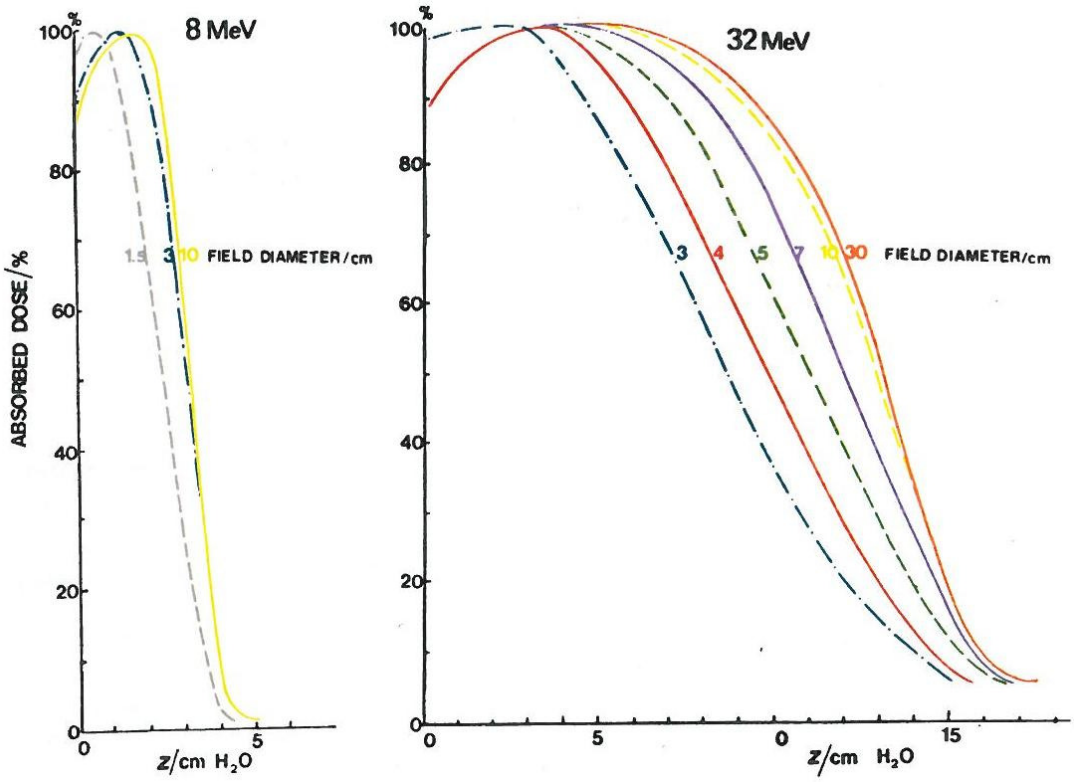

Figure 2.7 Depth dose curve variation with field size for 8 and 32 MeV electron beams. Figure reproduced from (ICRU, 1984a).

2.3.7 Oblique incidence

Angle of incidence of the incident electron beam alters the depth dose curves. This occurs when the treatment applicator is not parallel to the skin surface. As the angle of incidence increases, the slope of the dose gradient and the depth of maximum dose decrease. The effect of oblique incidence is represented by a number of pencil beams incident on an angled surface with each beam overlapping with the adjacent beam. Due to the overlap, the side scatter closer towards the surface increases and therefore increasing dose near the surface. A higher surface dose is observed for lower energy beams while higher energy beams show a slight increase in surface dose (Khan *et al.*, 1985; Ulin and Sternick, 1989). This effect is illustrated in figure 2.8. The position and gradient of the depth dose curve is also affected by obliquely angled electron beams. It has been shown that oblique incidence tends to shift the position of D_{max} toward the surface which decreases the penetration depth (Ekstrand and Dixon, 1982) and at oblique angles greater than 30°, the gradient of the curve decreases. These effects are shown in figure 2.9.

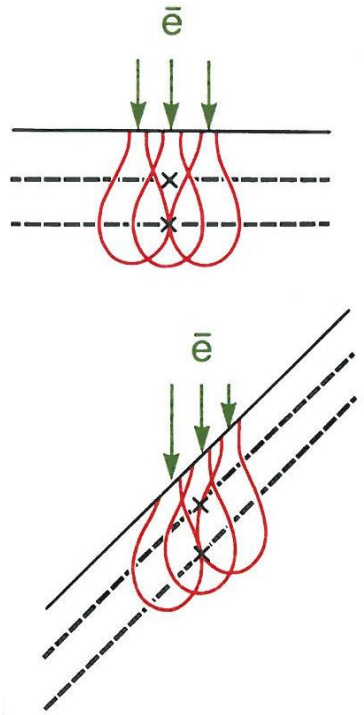

Figure 2.8 Illustration of how oblique incident surface angle impacts electron beams. Figure reproduced from (Khan, 2010).

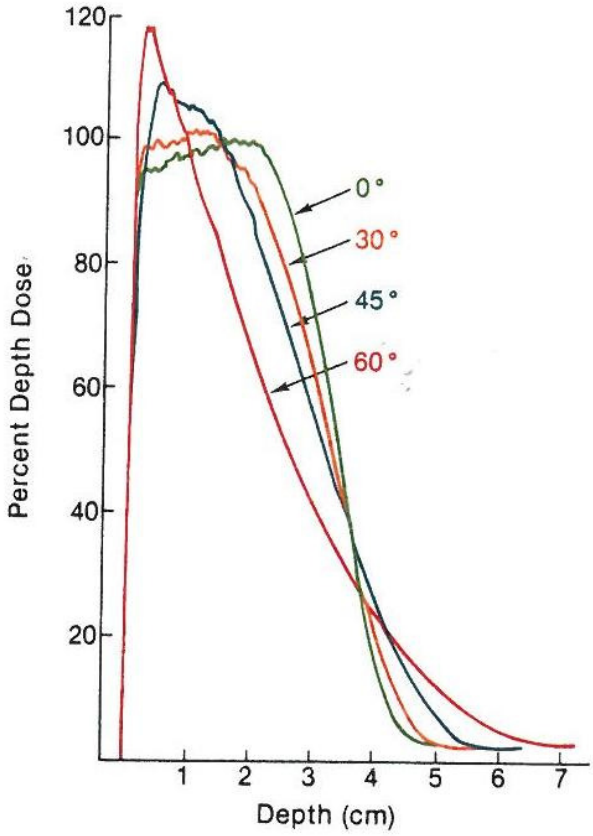

Figure 2.9 Changes in depth dose curve with oblique surface angle for a 9 MeV electron beam. Figure reproduced from (Khan, 2010).

2.3.8 Inhomogeneities

Electron beam dose distribution can be altered in the presence of tissue imhomogeneities such as bone and lung. With the presence of these inhomogeneities, there will be changes in scattering effects, especially at the interface between different media. This is known as interface effects. When the electron beam strikes the interface between the two materials, the scatter perturbation will affect the dose distribution near the interface. The lower density material will receive higher dose due to increased penetration of electrons. This effect can be seen in Figure 2.10. Within the low density region, electrons travel further with fewer scattering events. Hence the depth dose curve does not drop off as steeply in lung when compared to water.

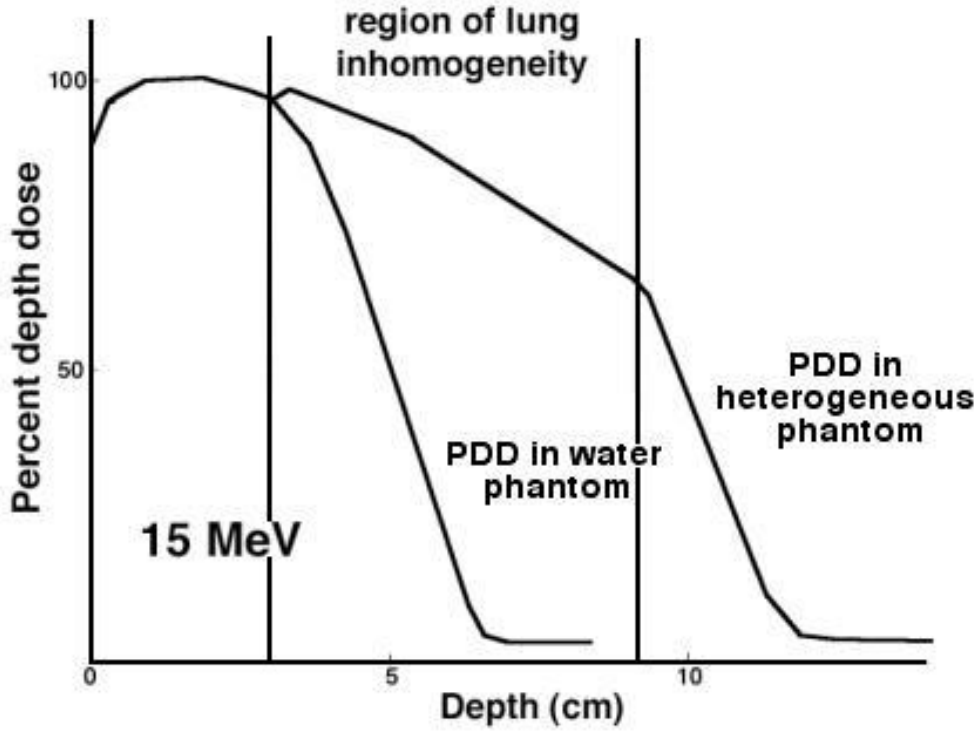

Figure 2.10 Depth dose effect of a 5cm lung inhomogeneity on a 15 MeV electron beam. Figure reproduced from (Podgorsak, 2005).

2.4 Monte Carlo techniques for electron beam radiotherapy treatment planning

2.4.1 Treatment planning dose calculation algorithms

Treatment planning systems (TPS) are used to simulate dose distributions for a radiotherapy prescription. TPSs utilise dose calculation algorithms to predict the dosimetry in a patient. The Pencil Beam algorithm is one of the most commonly used analytical models in radiotherapy dose calculation programs (Hogstrom *et al.*, 1981). Pencil beam algorithms are accurate in predicting dose distribution in situations where the geometry is a homogeneous material or infinite heterogeneous slabs normal to the incident beam. When three dimensional inhomogeneities are introduced to the calculations, the dose distribution was reported to have discrepancies of up to 12% (Mah *et al.*, 1989). The reason for the lack of accuracy is that pencil beam algorithms do not take changes in lateral scatter into account when inhomogeneities are encountered. Improvements have been made in recent years but the gain in accuracy remains limited (Kawrakow *et al.*, 1996).

Monte Carlo based algorithms have the highest accuracy among electron beam algorithms (Doucet *et al.*, 2003). Full Monte Carlo algorithms are capable of simulating every particle interaction in a given volume. They are used to model the effect of each individual event in the transport of radiation through matter (Bielajew and Rogers, 1992). However, this requires an enormous amount of processing power and time. To implement Monte Carlo algorithms in a commercial treatment planning system, a compromise between accuracy and calculation time has to be made. With recent developments to computer hardware, it is now possible to run fast Monte Carlo codes in a reasonable amount of time, generally of the order of a few minutes to under an hour (Ma *et al.*, 2002). However, due to the enormous number of particles that have to be simulated, the computation time can be excessive regardless of hardware advances. To significantly decrease computation time, approximations and simplifications of the transport processes are made to the algorithm whilst maintaining a high degree of accuracy. Several fast Monte Carlo codes have been developed to improve efficiency and decrease the calculation time,

such as Macro Monte Carlo (Neuenschwander *et al.*, 1995), Superposition Monte Carlo (Keall and Hoban, 1996) and Voxel Monte Carlo (Kawrakow *et al.*, 1996). The Macro Monte Carlo code is implemented in the Eclipse Treatment planning system and Voxel Monte Carlo code is implemented in XiO. Only XiO's Voxel Monte Carlo is the subject of this investigation and therefore is discussed in detail here.

2.4.2 Voxel Monte Carlo for electron beams

Monte Carlo models like EGS4 (Nelson *et al.*, 1985) and ETRAN (Seltzer, 1988) are designed to perform full simulations of electron transport in materials for a wide range of energies. The time required to calculate can make it difficult to use these codes in radiation therapy. Voxel Monte Carlo (VMC) (Kawrakow *et al.*, 1996) was developed by introducing simplifications and approximations to the transport algorithm that are applicable in the kinetic energy range from 1 to 30 MeV, i.e. the radiation therapy range.

The basis of the Voxel Monte Carlo algorithm for electron beams starts off with the trace of one electron interaction history, simulated in homogeneous water using multiple elastic and inelastic scattering (Kawrakow, 1997). The particle is scattered due to the collisions it undergoes and loses energy in inelastic collisions. The algorithm uses a simplified probability distribution function for multiple scatter which is a function of scattering power and electron momentum (Kawrakow *et al.*, 1996). The simplified form of the multiple scattering distribution used by the model results in an underestimation of large angle scatter. This was assumed to be insignificant for beam geometries studied in the original work (Kawrakow *et al.*, 1996) which were all normally incident on the phantom. The secondary electron production is also simplified and is described using Møller differential cross section (Kawrakow *et al.*, 1996). The code approximates the sampling of secondary electron energy and is done using a cut off energy (E_C) (Kawrakow *et al.*, 1996). For a given calculation voxel size, the production of secondary electrons are negligible due to the short travel range. Therefore, below this cut off energy, there is no secondary electron production and the incident electrons lose energy in a continuous process.

To improve calculation times, bremsstrahlung produced in the model is immediately discarded. To account for the bremsstrahlung photons generated from electron interactions, a photon background dose taken from the measured dose distribution in a water phantom is added to the calculated dose distribution (Kawrakow *et al.*, 1996). The background photon dose can originate from two sources; the bremsstrahlung photons produced in the patient and contamination photons escaping the head of the linear accelerator. The bremsstrahlung photons produced in the patient are a product of inelastic collisions with nuclei which leads to radiative losses. The photons generated from the head of the linear accelerator are a result of the electron beam interacting with components such as the transmission monitor chamber, scattering foil, collimators and electron applicator.

The continuous energy loss of electrons is simulated by modifying the mass stopping powers provided by the ICRU (ICRU, 1992). These stopping powers include both energy losses due to discrete interactions and energy loss due to continuous processes. The continuous process is the energy loss due to inelastic process where particles with energies below the applied cut off energy are produced (Kawrakow *et al.*, 1996). To obtain the continuous radiation, the stopping power due to interactions is subtracted.

VMC uses history repetition to reduce the number of histories simulated (Fippel, 1999). If two electrons are incident on a homogeneous phantom, the same electron histories are simulated varying only in the initial position and direction (Kawrakow *et al.*, 1996). VMC uses pre-calculated electron history in a water phantom and applies the history to the existing patient geometry. The electron path lengths and scattering angles in heterogeneous medium is rescaled and adjusted based on the total stopping power of the medium.

XiO treatment planning system (Elekta) adopted the VMC model and modified it to accommodate vendor specific features (Kawrakow *et al.*, 1996). XiO electron Monte Carlo (eMC) has eight user-definable parameters for calculations: maximum number of histories, goal mean relative statistical uncertainty (MRSU) and MRSU threshold, dose update interval, random number generator seed, calculation grid size, heterogeneity correction and calculation of dose to medium or dose to water.

The description of these parameters were based on the XiO User Training Guide (ELEKTA, 2010).

2.4.3 Beam Modelling

The XiO eMC source model and algorithm is based on an early version of XVMC (Fippel, 1999). The description of the source model and algorithm used by XiO eMC to simulate the transport of electrons through air is well described by Vandervoort *et al.* (Vandervoort *et al.*, 2014) as summarised below.

To perform Monte Carlo treatment planning, each linear accelerator beam is modelled as a combination of photon and electron sources specific to the applicator and energy combination. The primary electron source uses an energy spectrum based on the Landau distribution (Landau, 1944) and particle transport begins in a plane below the jaws. In the same plane, particle transport for the photon contamination source also begins. By sampling points from a source distribution above the start plane, the initial position and direction of particles are determined. The off-axis particle fluence distribution is modelled by multiplying a radially dependent factor to the particle weight. The particle direction is modified by a scattering angle from an energy dependent Gaussian distribution. To transport electrons through the applicator, simplified air scatter logic is used to change direction at every step. With this process, it is assumed that there is no energy loss or creation of secondary particles. Between the end of the applicator and the patient surface, the step size is a tuneable parameter for different SSDs. Highly scattered electrons are excluded in this region because they are unlikely to contribute to patient dose (ICRU, 1984a). From the top plane of the electron cut-out, an additional electron source is employed to compensate for the approximations in electron transport through the air column. This source is the primary tuneable parameter for adjusting applicator output factors during beam modelling to match measurement. To correct for missing surface dose, another source of highly scattered low-energy electrons is also available if necessary. XVMC is not designed for use with high-Z materials hence particle transport through the accelerator head is not modelled explicitly. Particle interactions with applicator cut-outs are modelled using kernels

precomputed with EGSnrc (Kawrakow *et al.*, 2002). “Transmission kernels” are used to model particles incident on the top surface of the cut-out outside the aperture. “Rim kernels” model electrons incident on top the surface of the cut-out within 0.5 cm of the aperture. Finally, “face kernels” model electron scatter off the interior faces of an aperture. For patient specific cut-outs, the material composition, thickness, distance from the nominal source position of the accelerator to lower surface of the cut-out must be provided (Edimo *et al.*, 2013).

The beam model provides information about the location, direction and energy of incident particles to the patient dose calculation algorithm and is machine specific. This is simplified by using measured data to determine the fluence distributions (Chetty *et al.*, 2007). A set of measured depth doses, axial and transverse profiles and output factors is acquired and the model parameters are adjusted by the manufacturer (ELEKTA) to minimise the difference between measurements and calculations in water. The depth dose curves are used to determine the energy spectrum of the beams and the off-axis variations are accounted for by the lateral profiles. The output factors are used to determine the amount of scatter from the applicator, cut-out and air column in the beam. The quality of the beam model is highly dependent on the quality of measurements.

Advantages of using measurement-driven models are that they do not require data of the linear accelerator head which helps by saving calculation time and disk space (Ma *et al.*, 1997). The beam model is divided into two parts; particle transport though the linear accelerator head and dose calculation in the patient. The particle transport involves Monte Carlo simulation of the accelerator head where beam simulations are based on the interactions of electrons in the linear accelerator head. Elekta models the accelerator head using calculation kernels which takes care of electron transport before the patient. These calculation kernels are full Monte Carlo simulations of the linear accelerator and applicator combinations which are performed beforehand and saved to storage. This provides individual beam models for each energy and applicator. The VMC code starts its calculation only when the beam enters the patient.

2.4.4 Maximum Number of Histories

One particle history of a calculation is the possible path length or the sequence of interactions that could occur until the particle has lost all its energy. Each sequence of energy loss and secondary particle creation is simulated from the primary particle. Once the maximum number of histories is reached, the simulation process will terminate. The maximum number of histories is defaulted to 1.0E+12. By increasing the number of histories, the statistical uncertainty will reduce but the computational time increases. To determine an acceptable isodose distribution, a certain minimum number of histories are required. However, adding extra histories does not necessarily improve the accuracy of the dose distribution, only the statistical uncertainty. For that particular reason, the number of histories was set to the default and the goal mean relative statistical uncertainty parameter was used to terminate the calculation.

2.4.5 Goal Mean relative statistical uncertainty (MRSU) and MRSU Threshold

The goal MRSU is a parameter used to terminate the calculation. The goal MRSU value fixes the largest average uncertainty that is accepted in the final dose calculation and has an allowable range of 0 to 100%. Typically XiO runs 1.0E+8 histories to reach a goal MRSU of 2%. To allow XiO to simulate the maximum number of histories, i.e. 1.0E+12, the goal MRSU must be set to zero. The particle histories will continue to be generated until the goal MRSU parameter is reached. The goal MRSU parameter is defined as:

$$MRSU_{D\geq P} = \sqrt{\frac{1}{N}\sum_{k=1}^{N}\frac{s_k^2}{D_k^2}} \qquad 2.3$$

Where, D is the dose, P is the threshold percentage dose set by the user, N is the number of voxels where dose is greater than or equal to P, s_k^2 is the estimated variance of the mean at voxel *k* and D_k^2 is the squared dose deposited in voxel *k*. The MRSU threshold, P is used to control the voxels that will be included in the MRSU

goal calculations. The MRSU threshold sets the limit to account for dose deposited in the entire computation grid. Not every voxel needs to enter in the calculation of this average. If 50% was chosen for the threshold, voxels where the dose is less than half of the maximum dose deposited will not be included. The sum is computed over the N voxels that satisfy the condition hence saving calculation time. 50% is the default value for P because this allow comparison with the ICCR 2000 benchmark of Monte Carlo codes (Rogers and Mohan, 2000).

Using a small goal MRSU value such as 0.5% or 1% will typically require a large number of histories and would increase the calculation time. The calculation time can be reduced by increasing the goal MRSU. In a clinical environment, a goal MRSU between the range of 1% and 2% is generally acceptable because the balance between calculation time and the variance needs to be met for practical use in a clinical scenario. Decreasing the goal MRSU only means reducing the statistical uncertainty in a voxel. Users need to aware of the statistical variation of individual points that may have dose uncertainties higher than the average. When a dose calculation is performed, there will always be a chance that the computed dose in a particular voxel could be higher or lower than the average dose. To avoid signification errors, dose should be prescribed to a volume rather than to a single point.

2.4.6 Dose Interval Update

The maximum number of histories and Goal MRSU setting are used to determine when to stop the dose calculation. These parameters are not constantly being checked. Dose update interval allows the user to set the number of histories after which the dose distribution is evaluated and updated graphically. This parameter is mainly to reduce total calculation time by checking that the simulation has achieved the termination criteria (goal MRSU) and does not generate unnecessary histories.

2.4.7 Random Number Generator Seed

In Monte Carlo algorithms, the initial interaction of a particle is determined by random numbers. This random number is generated by a separate software program

called the Random Number Generator. A seed number is set by the user to determine the first number sequence generated by the random number generator. The seed will generate a random number sequence and is determined by fixed calculation steps. XiO eMC allows the user the set the seed but it will not influence the quality of the dose calculation.

2.4.8 Calculation Grid Size

A grid for an eMC calculation is defined as a cubic volume in the CT reconstructed slices of a patient. This volume is then divided into individual voxels with user definable dimensions. As the number of voxels in the calculation grid increases, so does the calculation time. If the nominal field size increases with a fixed grid size, relatively more voxels are being included and therefore increasing the overall calculation time. Similarly by increasing the beam energy, the calculation time also increases. If the particle is more energetic, the particle will travel deeper with a longer track hence increasing the number of included voxels. The impact of grid size also affects the statistical uncertainty and dose accuracy. As the grid size increases, volume averaging occurs and therefore reduces the accuracy of steep dose gradients. If the goal MRSU remains unchanged, then the final uncertainty and accuracy of the calculation will remain constant with grid size.

2.4.9 Medium characterisation

Both the XVMC and VMC electron Monte Carlo codes extract interaction properties by directly correlating the collision and radiative stopping powers with the Hounsfield Unit (HU). With this method, material properties vary continuously with HU and there are no arbitrary boundaries between tissue types based on HU. Nor does it require a CT calibration curve (Reynaert *et al.*, 2006).

However, in XiO eMC the conversion from CT number to material properties is done in two stages. Firstly, the CT number is mapped to an electron density table specific to the CT scanner. Then the electron density is mapped to mass density using an internal conversion table. The XiO eMC dose engine uses the same approach as XVMC for the assignment of material properties. The mass density is used to

calculate correction factors that modify electron stopping powers, electron scattering powers and photon attenuation coefficients that are tabulated for water (J. Satterthwaite 2016, personal communication, 19 November). Therefore only data for water is used in the XiO eMC calculation. The media composition is only used to derive correction factors for the water data.

2.4.10 Heterogeneity Correction

XiO eMC offers the option of heterogeneity in the dose calculation module. When *'Yes'* is selected, the electron density of each voxel is determined using the current CT slices. If the option is set to *'No'*, XiO eMC assigns a relative electron density equivalent of 1.0 to every voxel within the patient surface instead of the actual density from the CT image. The relative electron density is the electron density of the material (electrons cm^{-3}) divided by the electron density of water (electrons cm^{-3}). This option is useful when heterogeneity correction tests are performed as part of routine quality assurance checks.

2.4.11 Dose to medium/water calculation

Absorbed dose can be calculated to water or medium with XiO eMC. In the current clinical practice, to compare Monte Carlo simulations of dose-to-medium (D_m) to dose-to-water (D_w), a conversion from D_m to D_w is required. Due to this requirement, when dose to water is selected, the algorithm will calculate dose to a small mass of water within the medium. When dose to medium is selected, the absorbed dose is calculated for that medium based on the material composition. The difference between dose to water and dose to medium calculations is an important issue. There is still debate in the medical physics community about which of these methods is most appropriate (Ma and Li, 2011). Due to the difference in calculated dose between dose to medium and dose to water, users need be aware of these changes as they can directly affect the dose delivered to patients.

2.5 XiO eMC algorithm limitations

Every treatment planning algorithm has its limitations. For XiO eMC (V4.80.03), the limitations that are stated in the training guide (ELEKTA, 2010) are summarised in this paragraph. The source-to-surface distance (SSD) is limited to the range between 100 and 115 cm. At SSDs shorter than 100 cm, dose artefacts may appear due to the scatter simulation from the electron insert. For SSDs beyond 120 cm, the air scatter approximations may create errors. For most clinical cases, the SSD will be within the range of 100 cm – 115 cm. Exceptions may occur with oblique incidence or irregular surfaces which may result in the SSD being slightly outside this range.

High density materials in the patient volume maybe significantly decrease the dose calculation accuracy. This is due to the simplified approximations that are used in the electron transport and the creation of secondary particles. Another limitation is known as voxelisation artefacts or partial volume effects. Due to the limited resolution of the dose grid, the density within the voxels maybe averaged when it lies in the interface between different densities. One major limitation is that computed point doses should never be used for Monitor Unit (MU) calculations (Chetty *et al.*, 2007). Clinical plans should always be verified by the coverage of isodose lines and dose volume histograms (DVH). XiO calculates MUs based on the dose at the beam weight point. This is counter to the recommendations of AAPM TG105 report (Chetty *et al.*, 2007). However, the statistical uncertainty at the beam weight point is significantly smaller than the overall uncertainty for the beam. This means for a goal MRSU of 1 to 2%, the statistical uncertainty for MUs is approximately 0.5 to 1%.

2.6 Radiochromic Film (GafChromic®)

Radiochromic films are dosimeters that depend on the process of permanent colouration when exposed to ionising radiation (Niroomand-Rad *et al.*, 1998). International Specialty Products (ISP, Wayne, NJ) manufactures a self-developing radiochromic film called Gafchromic® EBT. Radiochromic films are based on the polymerisation of microcrystals which results in the film progressively changing

colour. Its optical density change has a correlation to the amount of absorbed dose. Radiochromic films have been widely investigated and it has been shown that the response is independent of fractionation, dose rate and energy (Arjomandy *et al.*, 2010; Su *et al.*, 2007). Depth dose measurements with radiochromic films have also been investigated and have proven the films to be an accurate dosimeter (Arjomandy *et al.*, 2012; O'Reilly *et al.*, 2013; Xu *et al.*, 2009).

The first type of Gafchromic® EBT film, released in 2004 was suitable for use with radiotherapy doses. In 2009, Gafchromic® EBT film was replaced by Gafchromic® EBT2 film that incorporates a yellow marker dye in the active layer between the polyester laminate to allow for non-uniformity corrections and protect the active layer from exposure by UV and visible light (Casanova Borca *et al.*, 2013; Reinhardt *et al.*, 2012). In 2011, ISP released Gafchromic® EBT3 which has significant improvements over the predecessor such as identical polyester laminating layers giving it a symmetrical composition and a matte polyester substrate layer that prevents Newton's Rings formation. Gafchromic® EBT3 film is comprised of a single active layer, 30 μm thick which contains the active layer and marker dye. The active layer is between two 125 μm transparent polyester layers which have matte surfaces. The purpose of the matte surface is maintain a gap between the film surface and the glass window to prevent the formation of Newton's Rings, or interference patterns, when acquiring images using a flatbed scanner. These films provide sub millimetre spatial resolution when read-out by commercial flatbed scanners and are therefore capable of very high resolution dose measurements. Figure 2.11 displays the different layers between EBT, EBT2 and EBT3 film. Gafchromic® EBT3, which replaces the previous EBT2, has been shown to have similar dosimetric properties (Reinhardt *et al.*, 2012). The symmetrical composition completely eliminates the dependence of the response on the direction of exposure (Casanova Borca *et al.*, 2013; Reinhardt *et al.*, 2012). Directional response of film has been studied (Suchowerska *et al.*, 2001) and the findings are that films has low directional response except when irradiating parallel to the central axis if the beam. When film is irradiated parallel rather than perpendicular to the beam, an over response is seen and it has been suggested that the air gap rather than the

orientation of the film that is the cause of the over response (Suchowerska *et al.*, 2001).

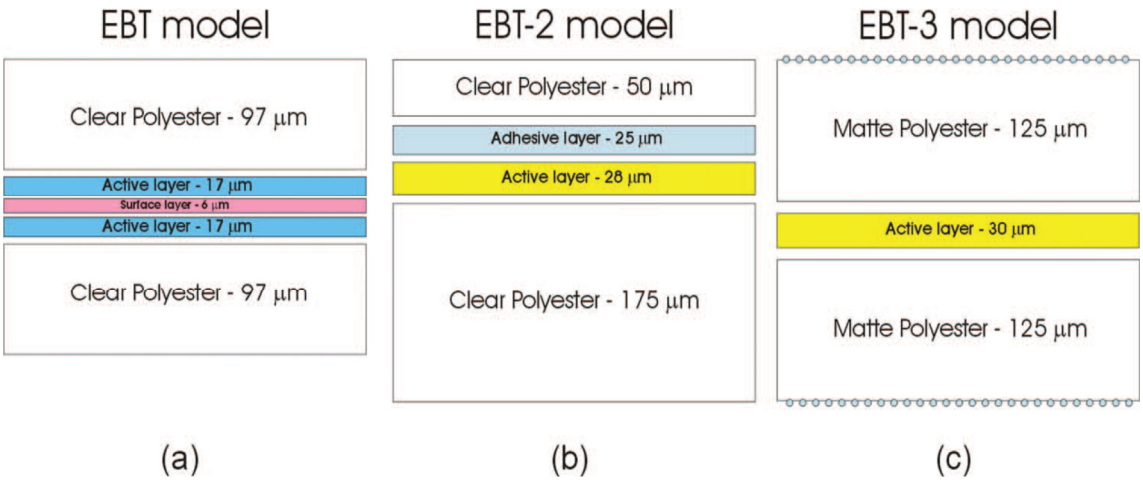

Figure 2.11 Diagram of the Gafchromic® film composition layer for (a) EBT, (b) EBT2 and (c) EBT3. Figure reproduced from (Devic *et al.*, 2012).

There are several possible sources that can influence the accuracy of Gafchromic films when scanned with flatbed scanners. When scanning of irradiated EBT3 films are performed, the polarisation of the transmitted light increases with increasing dose (Schoenfeld *et al.*, 2014). The magnitude of the artefact is dependent on the lateral position of the film on the scan window. There have been a few studies proposing the correction of lateral response artefact (Butson *et al.*, 2011; Paelinck *et al.*, 2007; Poppinga *et al.*, 2014). The change in response over the lateral scan axis was quantified and an increase in dose of up to 14% at maximum lateral position was seen (van Battum *et al.*, 2016). The artefact due to the light polarisation of film and the scanner's optical mirror system can be significantly reduced by setting lateral limits on the scan window restricting it to the central region.

Another source of film uncertainty is the uniformity of EBT3 films. It has been investigated to show that intra-film uniformity increases with increasing dose and was less than 1% for electron beams (Sorriaux *et al.*, 2013). EBT3 film dose response for various radiation types, including photons, electrons and protons, were also investigated and was shown to have a maximum spread 11.5% at doses from 0 to 10 Gy and up to 7.1% at 10 Gy (Sorriaux *et al.*, 2013).

2.6.1 Dose response curve

When radiochromic film is exposed to radiation, the discolouration of the film has a non-linear relationship to the amount of dose delivered. The discolouration effect will have a light attenuating effect which will block visible light from passing through the film. This reduction of light through the film is a measure called optical density (OD). An exponential function can be used to describe the relationship between the dose and OD. Figure 2.12 shows various calibration curves of different energies in a dose range of 0-10 Gy for 6 MV and 18 MV photon beams, 60 MeV and 100 MeV proton beams and 6 MeV electron beam (Sorriaux *et al.*, 2012).

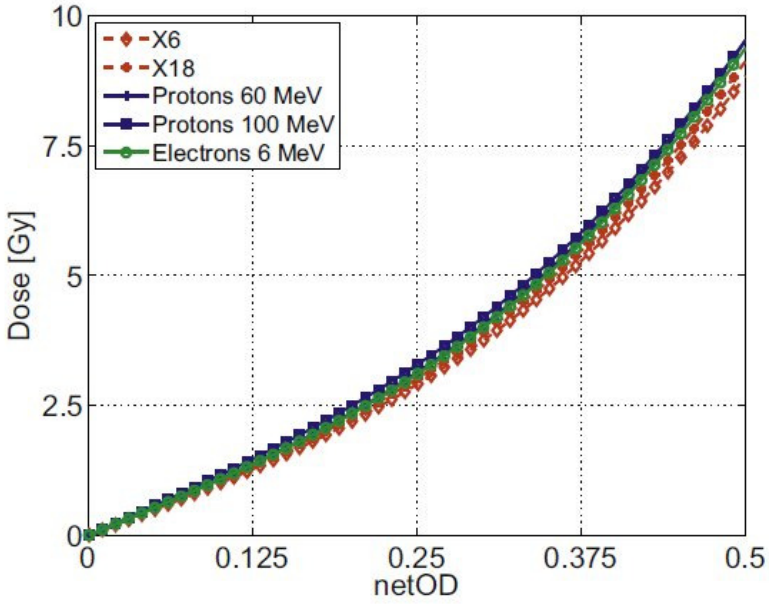

Figure 2.12 Dose VS Optical Density curve for a dose range of 0-10 Gy for 6 and 18 MV photon beams, 60 and 100 MeV proton beams and 6 MeV electron beam. Figure reproduced from (Sorriaux *et al.*, 2012).

Dose response curves are generated by exposing films to different dose levels and scanning them on a flat-bed scanner. Several studies have investigated the use of commercial flatbed scanners for film dosimetry (Devic *et al.*, 2004; Devic *et al.*, 2005; Devic *et al.*, 2006) which are shown to be an accurate tool for scanning. Theses scanners are generally used in the RGB (Red Green Blue) scanning mode. These colour channels exhibit a variation between the calibration curves and it has been

shown that the red channel is more appropriate at the therapeutic dose range (Sorriaux *et al.*, 2012).

2.7 Rationale for objectives

Validation of a Monte Carlo treatment planning system should include assessing the accuracy of the beam model and the radiation transport algorithm in homogeneous and heterogeneous phantoms (Chetty *et al.*, 2007). The beam model validation is to ensure parameters of the incident beam energy are correctly configured to produce dose distribution that is in agreement with the treatment machines. General recommendations are given for tests involving measurements in a homogeneous water phantom (Fraass *et al.*, 1998; IAEA, 2004; Van Dyk *et al.*, 1993), but issues related to non-standard measurements are excluded. These recommendations are generally point dose measurements at various locations within and outside heterogeneity regions and are done by positioning measurement devices such as ionisation chamber or diodes within the phantom. However, with ionisation chambers and diodes, there are disadvantages when using under electronic disequilibrium conditions. Measurement uncertainties such as beam quality dependence, polarity effects, ion recombination effects, and perturbation effects are some of reasons why ionisation chambers and diodes fail to accurately measure non-standard fields (Chetty *et al.*, 2007; Gerbi *et al.*, 2009).

AAPM TG-105 strongly encourages that validation testing of the Monte Carlo algorithm include experiments emphasising electronic disequilibrium effects (Chetty *et al.*, 2007). The use of anthropomorphic phantoms in this case seems feasible for the range of clinical circumstances but this method is generally an end-to-end test, not a commissioning procedure. An end-to-end test mimics the clinical workflow and any discrepancies are a result of the entire process. A commissioning procedure is generally a subset of specialised tests that can identify problems individually. The current state of practice for verifying the transport algorithm in non-standard beam geometries such as oblique incidence, inhomogeneities, and small field measurements are at the discretion of the clinical physicist. In the literature, experimental benchmarks were performed with a variety of slab heterogeneous

phantoms and agreement between Monte Carlo calculations and measurements are observed to be within 2 to 5% (Cygler *et al.*, 2004; Edimo *et al.*, 2013; Hu *et al.*, 2008). However, measurements of dose distribution near inhomogeneous boundaries are lacking due to physical limitations of the measurement device. This study hopes to overcome the ionisation chamber and diode limitations by introducing a measurement method that utilises radiochromic film in water to provide full scatter conditions.

2.8 Experimental Design

Using radiochromic film in water had been explored previously by various investigators (Arjomandy *et al.*, 2012; Xu *et al.*, 2009) and is proven to be an accurate dosimeter. Arjomandy et al. investigated EBT2 film as a depth dose measurement over a wide range of energies and modalities (Arjomandy *et al.*, 2012). Relative depth doses were extracted and excellent agreement of less than 2% was seen with those measured with ionisation chambers. Zhigang Xu et al. evaluated the eclipse electron Monte Carlo dose calculation for small fields and good agreement of within 4% was observed. Both of these methods use radiochromic film submerged in water with the aim to provide a high spatial resolution measurement and no distortion in the high gradient regions. Film analysis for both the studies are similar; using calibration methods recommended by David Lewis (Lewis, 2012) and the dose reported was in relative mode.

This study focuses on a similar approach of using radiochromic films in water but to ensure a reproducible setup, a film holder was designed and manufactured. The film calibration and analysis was done with the aim of measuring in absolute dose mode. A set of beams were setup to investigate standard uniform fields, the effects of oblique incidence, small field sizes and inhomogeneity. The setup includes measurements which are more complicated than measuring in the centre of a wide field at a depth. An opportunity to explore the dose distribution near the inhomogeneity boundaries will be possible with this measurement method.

METHODS

Accurate dose calculation is one of the important aspects between the dose prescription and the dose delivery process. Dose calculation is performed by a treatment planning system (TPS) which needs to be clinically implemented. Implementation of a TPS involves commissioning and validating the beam model under conditions similar to those found in clinic. The commissioning process is the most crucial part as the accuracy of the delivered dose to the patient is dependent on the accuracy of the beam data used. A set of beam data is required by ELEKTA to tune the XiO eMC beam model to match the users beam. The beam data collection is listed in Appendix A. As recommended by AAPM TG-106 (Das *et al.*, 2008a), ionisation chambers, diodes and diamond detectors are well suited for commissioning beam data in a scanning water phantom. The experimental validation process is another crucial component as it deals with how accurately the algorithm performs under different test conditions within a phantom. The types of recommended radiation detectors for validation experiments are described in AAPM TG-105 (Chetty *et al.*, 2007). However, with the recommended list of detectors, it is important to note the variations and associated uncertainties. Ionisation chambers are generally suitable for standard field validation but when used in non-standard fields, non-uniform dose regions may introduce a high degree of uncertainty. This project aims to verify both standard and non-standard fields by experimentation of a novel method for validating dose distributions. Both the commissioning process and experimental validation method are described in this chapter.

3.1 Irradiation Units

The linear accelerator used in this research was a Varian Clinac 21iX (Varian Medical Systems, Inc., Palo Alto, CA) which provides 6 MV and 18 MV photons and nominal electron energies of 6, 9, 12, 15 and 18 MeV. Three (6, 12 and 18 MeV) out of the five electron energies were used in this research. The electron outputs, symmetry and mechanical aspects are checked monthly according to tolerances stated in the AAPM TG-142 report (Klein *et al.*, 2009). The beams are calibrated once a year by an

ionisation chamber and electrometer that have been calibrated at the Australia Radiation Protection and Nuclear Safety Agency (ARPANSA). In addition to the calibration, a yearly independent dosimetry audit, managed by the Australian Clinical Dosimetry Service (ACDS), is performed on the linear accelerators.

3.2 XiO eMC commissioning

A standard set of water measurements were acquired during commissioning with a Varian 21iX linear accelerator (Varian Medical Systems, Inc., Palo Alto, CA). As part of the commissioning process, the XiO eMC calculated doses were compared to measured doses for these standard beams.

The commissioning process of a treatment planning system involves acquiring scanned and non-scanned beam data. The acquisition of the scanned beam data is the gathering of percentage depth dose curves and lateral profiles. The scanned beam data was measured using a Wellhöfer CC13 compact chamber and PPC-05 plane-parallel ionisation chamber in a BluePhantom^2 scanning water phantom (IBA Dosimetry GmbH, Schwarzenbruck, Germany). The depth of the ionisation chamber position was extremely critical in these measurements to obtain accurate data. A radius shift of 0.5 R_{cyl} for cylindrical ionisation chamber reference point of measurement is necessary, where R_{cyl} is the radius of the air cavity. The positioning of the chamber is used to avoid the need for fluence gradient correction (IAEA, 2000). For the parallel plate ionisation chamber, the reference point of measurement is taken to be on the inner surface of the entrance window. Scanning method recommendations were adopted from AAPM TG-106 protocol (Das *et al.*, 2008a). The non-scanned beam data required for XiO eMC are the output factors taken at a reference depth for each electron energy and applicator. The list of required beam data for XiO eMC beam model is specified in the user manual and is documented in appendix A.

3.2.1 Percentage depth dose

Percentage depth dose were taken with a fixed SSD of 100cm. The percentage depth ionisation curves were scanned for all energies using a PPC-05 plane-parallel

ionisation chamber, for all electron applicators. In addition to the standard fields, the percentage depth dose for a 5 x 5 cm^2 square cut-out centred in a 15 x 15 cm^2 applicator and an open 40 x 40 cm^2 field with no applicator were collected as part of the requirements. The scan was performed upwards to the surface of the water along the central axis to avoid the water ripple effects. Water ripple could cause the depth dose curve to have jagged edges and is more noticeable in the lower energies. The scanning beam data was repeated for every applicator at extended SSD of 110cm and 115cm. The percent depth ionisation curve was converted to depth dose curves using correction factors and restricted stopping power ratios from the TRS 398 protocol (IAEA, 2000). The PDD beam data was processed with the least squares smoothing routine.

3.2.2 Lateral profiles

Lateral profiles at the depth of 0.5 cm, depth of maximum dose (D_{max}), depth at 90% (R_{90}), 80% (R_{80}), 50% (R_{50}), 20% (R_{20}) of D_{max} and the practical range (R_P) + 2 cm were scanned for all energies and electron applicators. The lateral profiles of a 5 x 5 cm^2 square cut-out centred in a 15 x 15 cm^2 applicator and an open 40 x 40 cm^2 field with no applicator were acquired. The 40 x 40 cm^2 field scans are required for modelling the particle fluence incident upon the applicators (Vandervoort *et al.*, 2014). The choice of chamber is critical for profile measurements due the effect of volume averaging when measuring in the high gradient penumbra region. It is recommended by AAPM TG-106 that a small volume detector is preferred for profiles. Both in-plane and cross-plane profiles were acquired using a CC13 compact ionisation chamber. During linear accelerator commissioning, in-plane and cross-plane scans were acquired and both the symmetries were found to be less than 1%. There is a difference between the in-plane and cross-plane profiles in the shoulder. However, the difference was insignificant and therefore only cross-plane profiles were used for beam modelling. The lateral profiles were smoothed using a median smoothing function that preserves the gradient, then centred and made symmetric. The mean values of both sides were used to calculate the symmetric curve. The profiles were made symmetric because the beam model does not reproduce beam asymmetry.

The beam symmetry for the linear accelerators used in this work was maintained at less than 2%.

3.2.3 Output Factors

For each electron energy, a single reference depth of D_{max} was chosen to measure the output factor. The output factor is defined as the ratio of dose at D_{max} for a given applicator to the dose at D_{max} for the reference applicator of 10 x 10 cm^2. The factors can be measured either in a water phantom or in solid phantom with a PPC-05 plane-parallel ionisation chamber. During commissioning, the factors were measured in the BluePhantom^2 water phantom for consistency. The output factors were measured for every field and SSD listed for PDD and profiles measurement.

3.2.4 Model Validation

The beam models were created by Elekta using the acquired beam data during commissioning. It is necessary to perform validation measurements of the Monte Carlo algorithm to evaluate how accurately the algorithm performs under different test conditions. The evaluation of beam model accuracy was performed by comparing the calculated and measured depth dose and profiles in a homogeneous water phantom for a range of field sizes. The cut-out factors were measured and compared to XiO eMC for each energy and range of applicators. The cut-out shapes validated include circular, ovals, squares and rectangles with field sizes ranging from 3 cm to 16 cm in diameter or length.

Recommendations for TPS validation tests are generally in homogeneous and heterogeneous phantoms; however issues related to electronic disequilibrium are excluded. Experimental validations should also be performed in more clinically relevant situations (Chetty *et al.*, 2007). This thesis explores the possibility of validating the electron Monte Carlo dose distributions in conditions other than the standard measurements.

3.3 Film holder design

This section covers the development of the water phantom, the design and construction of the various components made for this project. The original idea for using radiochromic films in water to validate 2D dose distributions was introduced by Xu, Z. et al. (Xu *et al.*, 2009). Xu, Z. et al. evaluated the electron Monte Carlo dose calculation algorithm in the Eclipse treatment planning system. The old rule of thumb (beam energy in MeV / 2.5 in centimetres) to approximate the limiting cut-out size of an electron field was investigated for small circular fields. In the study, Xu, Z. et al. compared eMC calculations and relative measurements of depth doses and isodose distributions using EBT film in water. However, in this work, a more reproducible setup was designed and constructed to hold the films vertically in water.

All measurements were done in water to avoid air gaps that may be present when using solid water phantoms. A small portable water phantom, as shown in figure 3.1, was designed and constructed to hold film in a highly reproducible setup. It contains a U-Shaped holder made from PMMA to support the film in a vertical orientation. The film holder is suspended in water by the support of two rail holders. The film sits in a slit of less than 1 mm in the middle of the U-shaped holder. The U-shaped holder measures 29.5 x 29 cm and fits a full sized EBT3 film. The measurement setup is shown in figure 3.2. This phantom allows the film to measure the 2D dose distribution in a transverse plane. To align the film edge to the water surface, first the SSD to the film is set using a calibrated front pointer as shown in figure 3.3. Then the tank is offset longitudinally to set the water level to the end of the calibrated front pointer by using the treatment couch. This is to ensure that both the water level and the edge of the EBT3 film are at the desired SSD. The reproducibility of the film setup is ±0.5 mm or less.

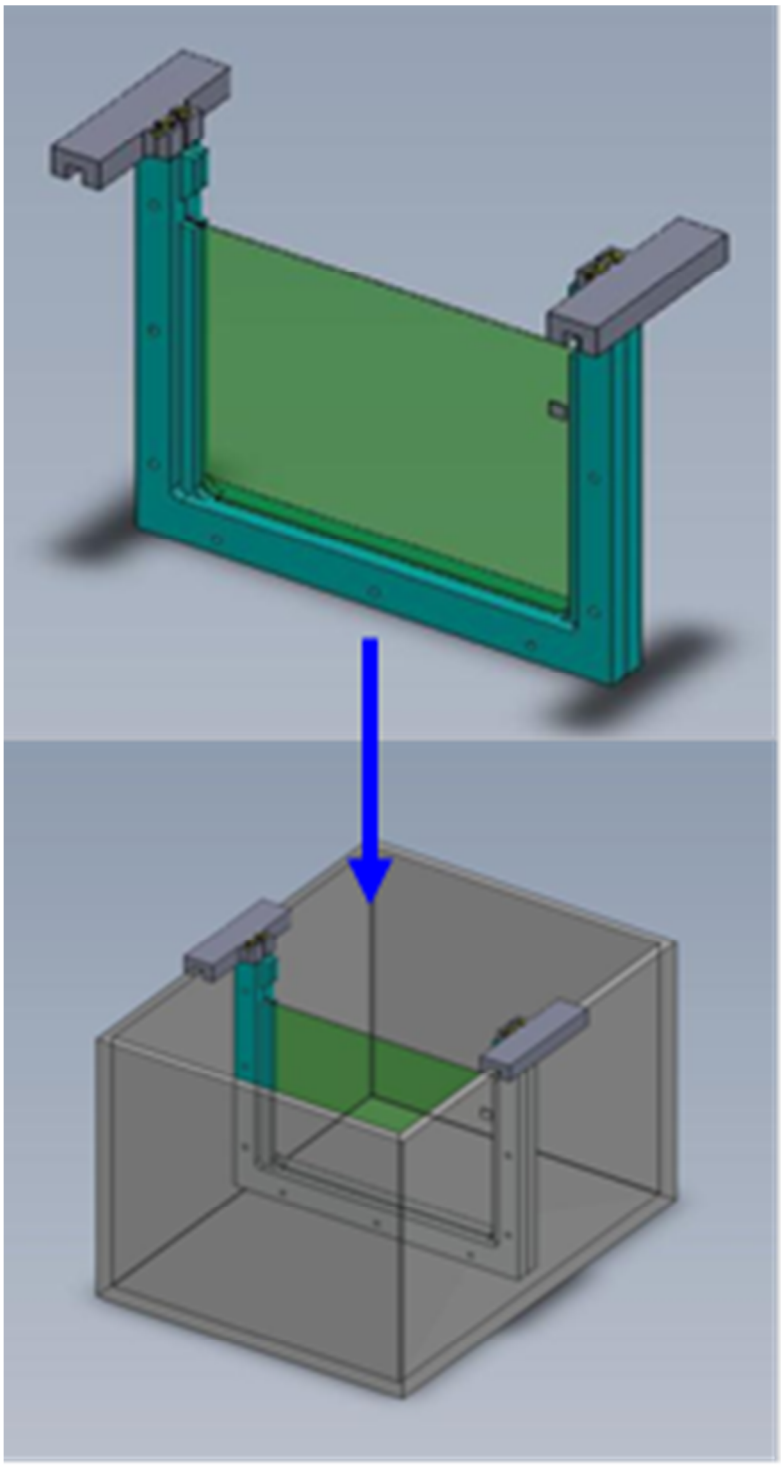

Figure 3.1 U-Shaped holder and water phantom to support radiochromic film.

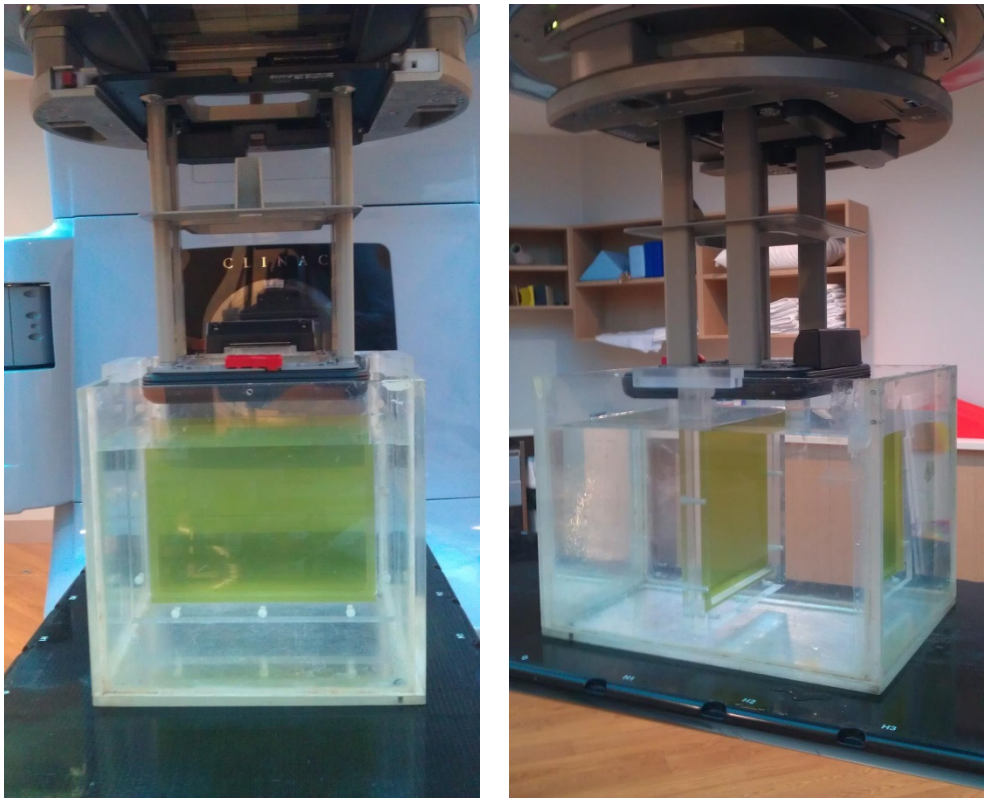

Figure 3.2 U-Shaped holder measurement setup with a Varian 21iX linear accelerator.

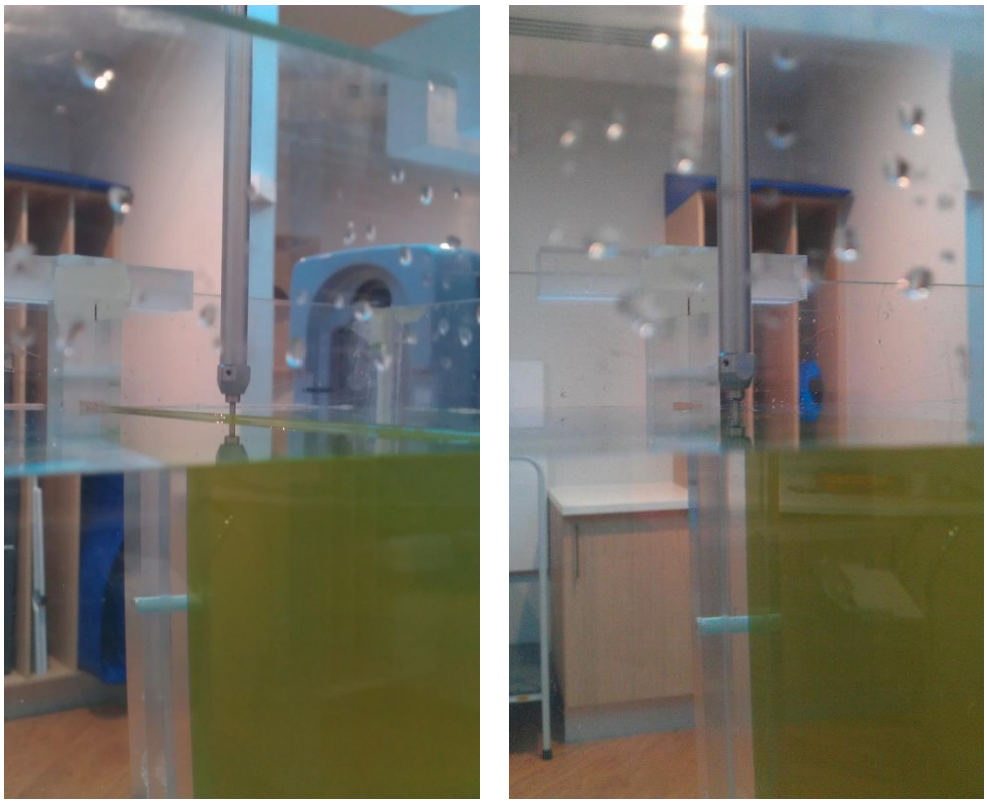

Figure 3.3 Aligning the film edge to the water surface at source-to-surface distance of 100 cm.

3.4 Film Calibration

To establish the dose response calibration curve for electron beams, films from batch #A01231204 were cut to 4x4 cm size. The pieces of film were marked on the top right hand corner to keep track of the orientation. It is important to note the film orientation as the scanner response varies with different orientation (Reinhardt *et al.*, 2012). Electron beams from a Varian 21iX linear accelerator were used to irradiate the films. Doses ranging from 10 to 600 cGy were delivered with a 12 MeV, 10 x 10 cm^2 field and at a depth of dose maximum (2.9cm) in a CIRS Plastic Water® phantom (Computerized Imaging Reference Systems, Inc., Norfolk, VA). The water equivalence of Plastic Water had previously been established by comparing doses measured in Plastic Water with doses in real water, according to TRS398 (IAEA, 2000). For the 12 MeV electron beam used for calibration, doses agreed to within 0.4%. Using a 12 MeV electron beam is suitable for defining the calibration curve due to the region of low dose gradient at depth of maximum dose extending over a greater depth than the lower energies. 12 MeV is also in the middle of the energy range that is investigated for this work. Repeat calibration measurements from the same batch of film were performed to determine the uncertainty in the film measurement at doses ranging from 10 to 600 cGy.

Calibration films were scanned on the same side consistently with the help of the same orientation marker on the top right hand corner of the films. This is to eliminate any orientation dependence whilst scanning. As shown in figure 3.4, the films were lined up in two rows, five films in each row, along the centre of the scan plane. After scanning the calibration films, a region of interest in the centre of the film is selected and the absolute dose values were assigned respectively based on the measured linear accelerator output at the time of film calibration (see section 3.3.1). An example of the calibration curve generated by the SNC software is shown in figure 3.5. The red curve represents the linear plot between the calibration points and the green curve represents the exponential fitted curve. SNC Patient software uses the exponential fitted calibration curve to convert the scanner response to dose.

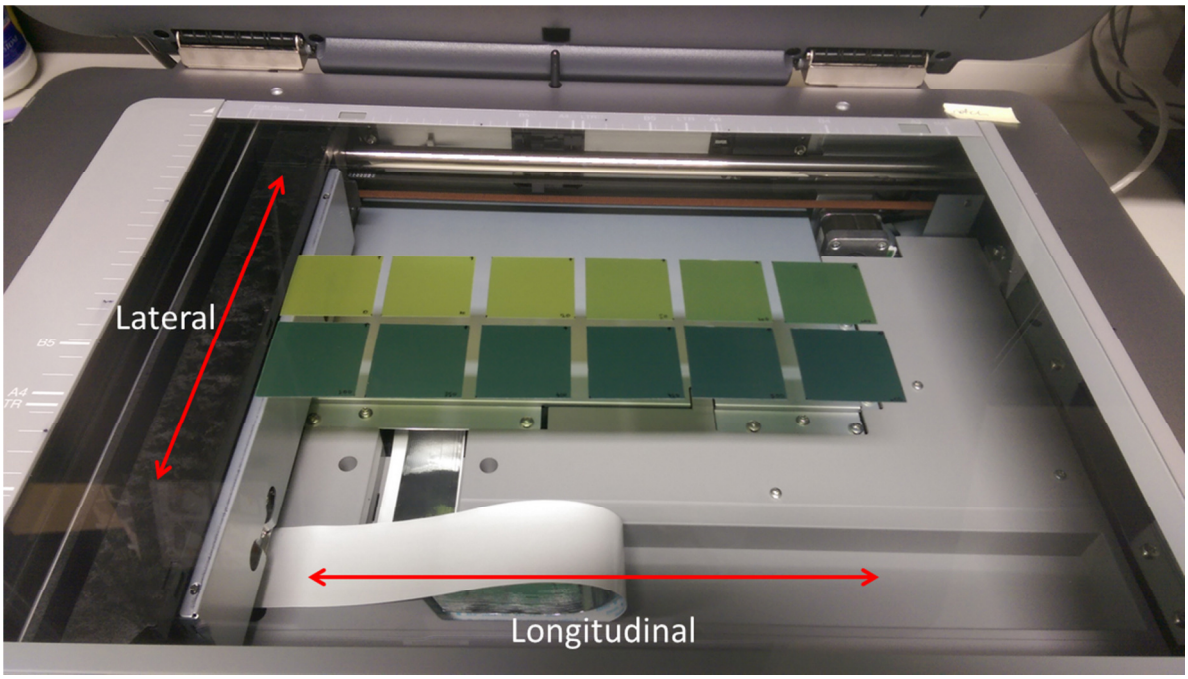

Figure 3.4 Calibration films on an EPSON 10000XL flatbed scanner.

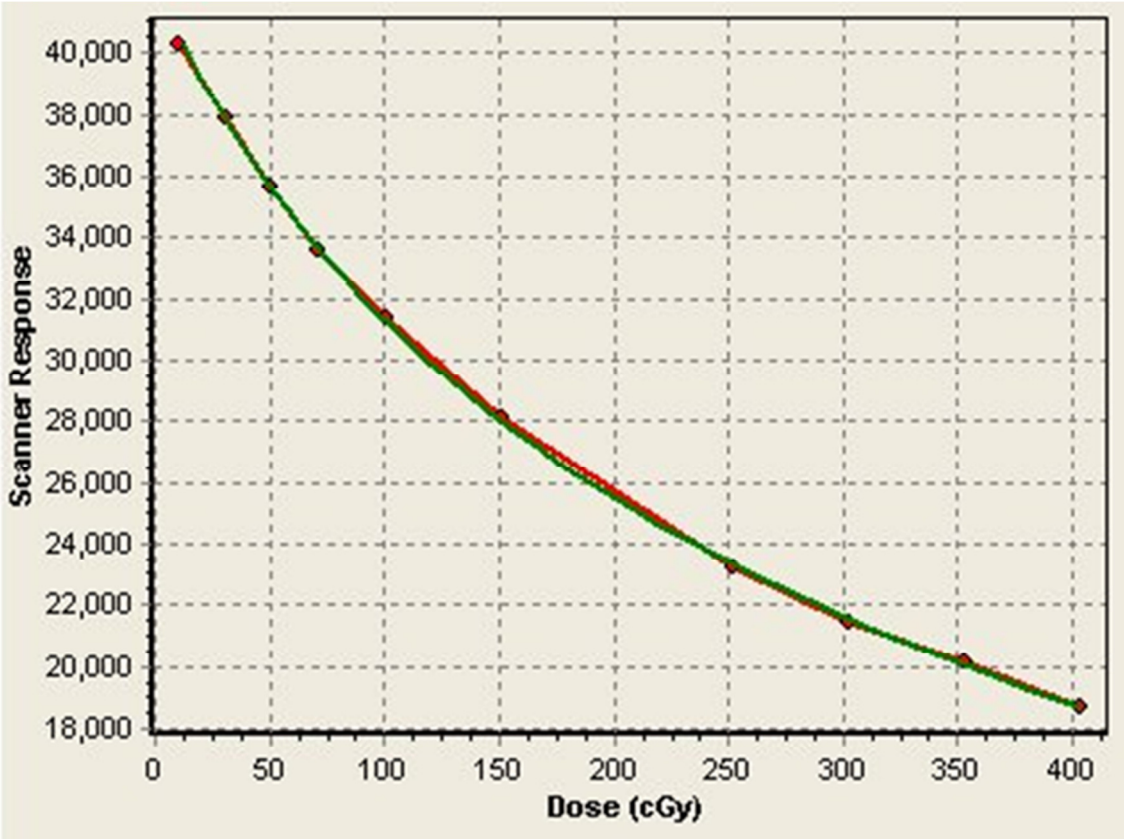

Figure 3.5 GafChromic® EBT3 calibration curves generated by SNC Patient software. The red curve represents the linear interpolation between calibration points and the green curve represents the exponential fitted curve.

3.4.1 Linear Accelerator Output

Linear accelerator output can fluctuate daily. To correct for the linear accelerator variation of dose delivered during calibration, the absolute dose-to-water was determined in accordance to TRS398 protocol (IAEA, 2000). The linear accelerator was calibrated to deliver 1 cGy/MU to the depth of dose maximum for all electron energies. The output for 12 MeV, 10 x 10 cm^2 field with standard insert was determined using a Wellhöfer PPC-05 plane-parallel ionisation chamber connected to a DOSE1 electrometer (IBA Dosimetry GmbH, Schwarzenbruck, Germany). Measurements were done at a reference depth of 2.9cm. The chamber's calibration factor is traceable to Australian Radiation Protection and Nuclear Safety Agency (ARPANSA) which is the National Standards Laboratory. The ionisation chamber was placed in Solid Water with a PMMA build-up cap. Ambient temperature (T) and pressure (P) corrections were applied to the measured charge (nC). A temperature and pressure correction factor (C_{TP}) is calculated using equation 3.1.

$$C_{TP} = \frac{273.2 + T\ (°C)}{293.2\ (°C)} \frac{101.3kPa}{P\ (kPa)} \tag{3.1}$$

To determine the linear accelerator output, the absolute dose delivered per monitor unit (cGy/MU) at depth of maximum dose is calculated using equation 3.2.

$$Output(Dmax) = M \times C_{TP} \times TCF_{water}(Z_{ref}) \times PCF \times \frac{100}{PDD_{Z_{ref}}} \tag{3.2}$$

Where,

$Output(Dmax)$ is the absolute dose delivered per monitor unit at the depth of maximum dose.

M is the electrometer reading (nC).

C_{TP} is the temperature and pressure correction factor.

$TCF_{water}(Z_{ref})$ is defined as the total correction factor at Z_{ref} which consists of the dose to water cross calibration factor ($N_{dw}Q_{cross}$) at the measured energy, ionisation chamber response ($k_Q Q_{cross}$) and polarity (K_p) and recombination (K_s) ionisation chamber corrections.

PCF is the phantom correction factor for using solid water instead of water.
$PDD_{Z_{ref}}$ is the percentage depth dose at reference depth (Z_{ref}).

This is an important step to reduce the impact of linac variations in output on film uncertainties. Since a fixed amount of MUs were delivered, the absolute dose to film can be adjusted based on the linear accelerator's output during film calibration.

3.5 Film Handling and Scanning

Radiochromic films will begin to develop as soon as they are irradiated and will continue to develop with time. Irradiated films were given a minimum of 48 hours to stabilise before scanning.

To minimise the effect of post exposure changes in the film, calibration and measurement films were exposed within a 2 hour interval. Irradiated films were scanned with an EPSON Expression 10000XL (EPSON Deutschland GmbH, Meerbusch, Germany) flatbed scanner using methods described by Lewis (Lewis, 2012). Scans were performed in transmission mode with a resolution of 75 dpi and no colour correction was applied. 48-bit RGB scanned images were saved in Sun Nuclear Patient (Sun Nuclear Corporation, Melbourne, FL) software film format. Scanning of the film was done via an Epson Scan v3.49E (Seiko Epson Corporation, Suwa, Nagano, Japan) software. Films were aligned on the scanner using reference points marked on film and scanner surrounds. The SNC Patient Film QA module was used to scan and import the films. The EPSON software is launched automatically from the Film QA module during the scanning process. The scanned film image is saved as a SNC Patient film dose file format (.flm).

Seven preview scans were taken to allow the scanner to stabilise (Ferreira *et al.*, 2009) and films were placed consistently in the middle of the scan window in landscape orientation to minimize the effects of non-uniformity of scanner response (Sorriaux *et al.*, 2012). The lateral response of a flatbed scanner was previously investigated and showed differences of up to 11% when films are scanned at the edges (Menegotti *et al.*, 2008). To assess the effects of possible film heterogeneities and any non-uniformity of scanner response, unexposed films were scanned in the standard orientation and also rotated by 180°. The same scanner and analysis

settings as in the rest of this work were used. The red colour channel was selected to import the film as it has been shown to have the highest sensitivity to dose (Casanova Borca *et al.*, 2013; Ferreira *et al.*, 2009; Cygler *et al.*, 1987).

3.6 Film Analysis

Comparisons of calculated XiO eMC dose planes with radiochromic film measurements were done using SNC Patient™ software version 6.2.3 (Sun Nuclear Corporation, Melbourne, FL) and depth dose profile comparisons were done in Microsoft Excel (Microsoft, Redmond, WA). To fine tune the alignment of the film and calculated 2D dose distributions, the 'Calc Shift' option in SNC Patient software was used. The highest resolution of the scanned films is 1 mm and the calculated dose was shifted along the X and Y axis by ± 1 mm to achieve the highest passing rate.

All 2D comparisons of EBT3 and XiO eMC were done by comparing absolute dose per monitor unit (MU). The SNC Patient software gamma dose analysis was used to compare the overall 2D dose distributions and the distance-to-agreement (DTA) tool was used to compare doses in regions with steep gradients (Venselaar *et al.*, 2001). Gamma analysis is a measure between measurement and calculation points in both dose and physical distance in space (Low *et al.*, 1998). Gamma analysis combines dose difference (DD) and DTA criteria to calculate a dimensionless metric for each point in the evaluated distribution (Hussein *et al.*, 2013). A gamma of less than 1 indicates that the points lie within either the DD or DTA passing criteria. For a given DD/DTA criteria, the fraction of points that achieve a gamma < 1 is calculated and reported as a percentage of points that passed. A threshold is set where the minimum dose percent value must be met for the point to be included in the analysis. The purpose of this threshold is to exclude low dose regions or out of field doses during comparison and a typical value of 10% was used for all gamma comparisons. For standard fields, the gamma evaluation criteria were set to 2% and 2 mm. For the non-standard fields, the gamma evaluation criteria were set to 3% and 3 mm. These criteria align with TRS430 recommendations for simple and complex geometries respectively (IAEA, 2004).

3.7 Film method validation

3.7.1 Ionisation chamber and EBT3 film comparison

The film measurement method was validated by comparing EBT3 film measurements and ionisation chamber measurements taken in a Scanditronics Wellhöfer BluePhantom^2 scanning water phantom using the OmniPro^{TM} Accept 7.1a scanning software (IBA Dosimetry GmbH, Schwarzenbruck, Germany).

A lateral profile from the EBT3 film measurement was used to compare CC13 ionisation chamber. Measurements were performed with a 12 MeV electron beam defined by a 10 x 10 cm^2 square field at 100 cm SSD.

The accuracy of the film calibration method was verified by comparing EBT3 depth dose profiles from films irradiated parallel to the beam axis in the portable water phantom, to measurements with a PPC05 parallel plate ionisation chamber. The acquired depth ionisation data were converted to depth doses with the OmniPro^{TM} software using the IAEA TRS398 protocol (Williams and Thwaites, 2000). Ionisation chamber and EBT3 depth doses were compared in terms of absolute dose (cGy/MU) for 6, 12 and 18 MeV for a 10x10 cm^2 field at 100 and 105 cm SSD.

3.7.2 Effect of film rotation

In addition to the cross-plane measurements, an in-plane measurement was performed by rotating the water phantom and film by 90° and irradiated with a 45° gantry beam angle. Figure 3.6 a) shows the film being irradiated by a 45° angle beam with no tank rotation. Figure 3.6 b) shows the water tank setup rotated by 90° irradiated with the same 45° angle beam. The central axis depth dose curves for both orientations were compared. This validation method verifies that the radiochromic film reveals no difference when measuring in both cross-plane and in-plane orientations.

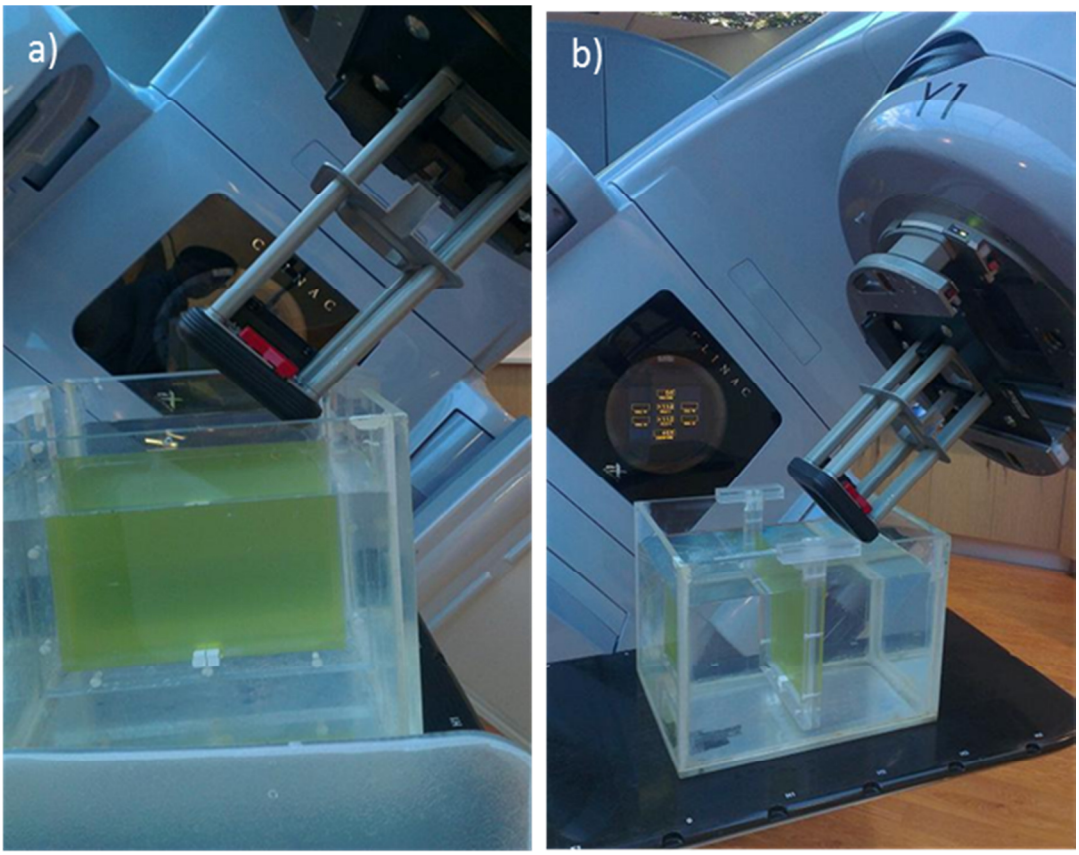

Figure 3.6 a) 45° gantry angle beam irradiating EBT3 film in the cross-plane orientation. b) EBT3 film positioned in the in-plane orientation irradiated by the same 45° gantry angle beam.

3.7.3 Film scanning validation

The variation of optical density within the scan window was investigated for the EPSON 10000XL scanner used in this project. A piece of unexposed film was scanned in the middle and at the edges of the scanning window. The difference in optical density was recorded.

3.8 Uncertainty of Methods

This section identifies the reproducibility of the film measurement and processing method. The measurement and scanning uncertainty was investigated and is described below. All uncertainty results were analysed and extracted from SNC Patient™ software.

3.8.1 Scanner uncertainty

Scanner reproducibility was investigated. The scanning reproducibility was analysed with a single film that was irradiated with 400 MUs using a 6 MeV beam, 3 cm diameter applicator insert in a 6 x 6 cm^2 electron applicator. Five consecutive scans were performed for the single film at the centre of the scanning window and for each individual scan the dose and depths at D_{max}, R_{90}, R_{50} and RW_{50} were recorded.

3.8.2 Measurement uncertainty

The reproducibility of the method was investigated by comparing five films irradiated in identical conditions in the same measurement session. The measurement was irradiated with 400 MUs using a 6 MeV beam, 3 cm diameter applicator insert in a 6 x 6 cm^2 electron applicator. Each film was scanned once in the centre of the scanning window. The dose and depths at D_{max}, R_{90}, R_{50} and RW_{50} were recorded for five films. The measurement uncertainty includes the reproducibility of irradiations and the reproducibility of the scanner.

3.8.3 2D Gamma Analysis uncertainty

The reproducibility of SNC Patient™ software 2D analysis results was investigated. The film software analysis process was performed using the five films from the measurement uncertainty investigation (section 3.8.2). XiO eMC 2-D dose distribution for a 6 MeV beam, 3 cm diameter insert in a 6 x 6 cm^2 electron applicator was used to perform the 2D analysis. The SNC Patient™ software reported gamma passing percentages were recorded.

3.9 CT number and Relative Electron Density

To correct for tissue heterogeneities for CT based treatment planning, the relationship between the CT number and electron density must be established (Saw *et al.*, 2005). Electron beams used are in the mega-electron volt (MeV) range and interact with matter principally by ionisation and excitation. XiO uses Monte Carlo algorithm to calculate dose deposited in tissue. As described in section 2.4.9, Monte

Carlo simulations can take tissue inhomogeneity into account by mapping CT numbers to an electron density table. Hence, a CT number (HU) to relative electron density conversion curve is needed for medium characterisation. The conversion is generally established by scanning a tissue characterisation phantom such as the CIRS Model 062 (CIRS Tissue Simulation Technology, Norfolk, VA). As shown in the figure 3.7, the CIRS phantom with multiple inserts of different simulated tissue composition and the corresponding scanned CT image. To determine the mean CT values and their standard deviation, regions of interest were drawn within each insert.

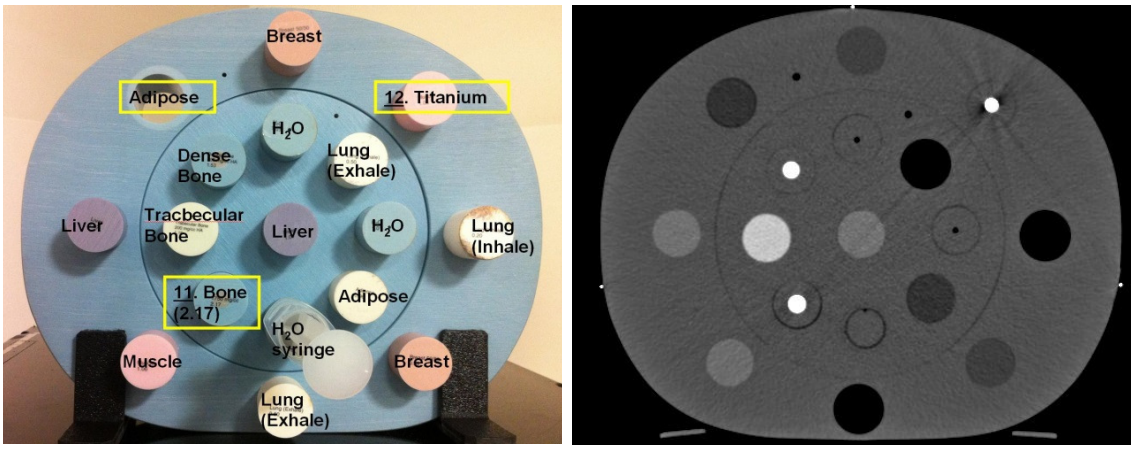

Figure 3.7 Tissue characterisation phantom CIRS Model 062 (left) and axial CT image of the phantom (right) taken at 140 kVp tube voltage.

To determine the RED for heterogeneity calculations, the materials (cork, Perspex and Teflon) used to create the configurations in figure 3.8 were scanned in a water phantom with a Brilliance Big Bore CT scanner. The scanning parameters were set to 4 x 0.75 collimation, field of view (FOV) of 180 mm and 3 mm increment. The average CT numbers were extracted from each material and were fitted to the CT to RED curve.

3.10 Film measurement and comparison

To extend the standard set of commissioning measurements to include clinically relevant conditions, measurements of standard fields, oblique incidence, small circular fields and inhomogeneity were designed to focus on specific geometries that are difficult or impossible to assess using ionisation chambers. Measurements were

performed with electron energies of 6, 12 and 18 MeV from a Varian 21iX linear accelerator (SN #4907).

In regions of shallow dose gradient, the dose comparison is straightforward. However, in steep dose gradient regions, the dose difference is sensitive to small spatial offsets (Low *et al.*, 1998). The DTA component of the gamma analysis was used to compare steep dose gradient regions like penumbras and depth dose curves. The concept of distance to agreement (DTA) was developed by Van Dyk (Van Dyk *et al.*, 1993) to compare high dose gradient regions. DTA is a measure of the nearest point in the measured distribution that is within a dose tolerance criterion.

Point dose comparison was done at depth of maximum dose (D_{max}). The XiO point doses used in the comparison includes the uncertainty of 1% as specified by the MRSU parameter. DTA was used to analyse doses at the depths of 90% (R_{90}) and 50% (R_{50}) of the maximum dose. The calculated and measured radiological widths (RW_{50}) were also compared at D_{max}.

3.10.1 Standard field measurements

For film holder validation purposes, standard fields were measured using a 10 x 10 cm^2 electron applicator at 100 cm SSD and a 6 x 6 cm^2 electron applicator at 105 cm SSD.

3.10.2 Obliquity measurements

Obliquity measurements were performed using gantry angles of 0°, 25° and 45°. The standard applicator insert with a field size of 6 x 6 cm^2 at SSD of 100 cm was used. To provide clearance for the electron applicator at gantry angle of 45°, the water phantom had to be offset laterally as shown in figure 3.6(a).

3.10.3 Small circular fields

For small fields, circular Cerrobend inserts of 2, 3, and 6 cm diameter (figure 3.8) were made in-house and the actual aperture size was verified with XiO printouts at 100 cm SSD. Measurements using the 2 and 3 cm diameter applicator inserts were

performed with a 6 MeV beam. Measurements using the 3 and 6 cm diameter applicator inserts were performed with 12 and 18 MeV beams.

3.10.4 Inhomogeneity measurements

Inhomogeneity measurements were performed with 3 materials (figure 3.8); cork mimicking lung, Perspex mimicking rib bone, and Teflon mimicking skull bone. The physical densities and relative electron densities (determined experimentally in section 3.9) of the materials can be found in Table 3.1.

These materials were cut into sizes as shown in table 3.1 and are positioned by sticking them on both sides of the film using adhesive tape that left no marks on the film (Figure 3.8). The inhomogeneity phantoms were irradiated with a 10 x 10 cm^2 field for rib and lung configuration and 6 x 6 cm^2 field for skull bone configuration at 100cm SSD.

Since the film is calibrated for dose-to-water but XiO eMC calculates dose-to-medium, a conversion from film dose-to-water to "film derived" dose-to-medium was performed using mass collision stopping power ratios for the rib bone and skull phantom to enable better interpretation of the result. As described in AAPM TG21 (Paul *et al.*, 1985), dose-to-water is related to dose-to-medium by

$$D_{water} = D_{medium}(\bar{S}/\rho)^{water}_{medium} \qquad 3.3$$

where $(\bar{S}/\rho)^{water}_{medium}$ is the ratio of the average unrestricted mass stopping power of water to the medium in question.

A mean electron energy of 3 MeV was assumed in all regions. The stopping power varies according to the electron energy spectrum and is a function of depth. This conversion has been described by Aubry *et al.* (Aubry *et al.*, 2011). Without a full Monte Carlo simulation, an approximation of the mean energy was made using the method described in AAPM TG21 (Paul *et al.*, 1985). This approximation has been shown to overestimate the beam energy at depth (Ding and Rogers, 1996). However, there is negligible change in collision mass stopping power ratios of medium to water (calculated using Table A.8, (Khan, 2003)) over the energy range of 1-4 MeV. This

ensures that this approximation is not highly sensitive to choice of energy at depth. Stopping power ratios were calculated for skull bone and for rib bone using the experimental surrogates for these materials i.e. Teflon and Perspex respectively. The surrogates were chosen as they have relative electron densities that closely match the biological materials. No stopping power ratio corrections are applied to the measurements in cork (lung) since the stopping power are equivalent to those in water (Aubry *et al.*, 2011).

Table 3.1 Physical dimensions and density of the materials used in the inhomogeneity measurements.

Materials	Dimensions: Height x Width x Length (cm)	Physical Density (g/cm^3)	CT number (HU)	Relative Electron Density
Teflon	1 x 8 x 3	2.2	913.75	1.61
Perspex	1 x 1 x 3	1.18	109.66	1.13
Cork	5 x 8 x 3	0.24	-656.94	0.34

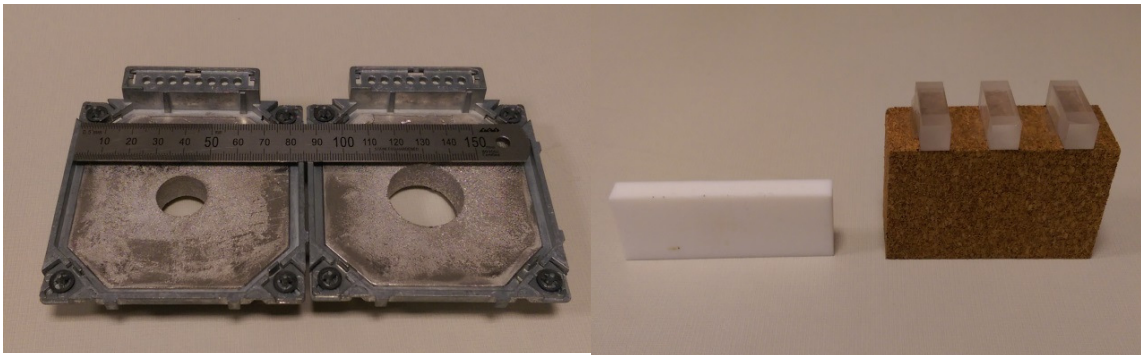

Figure 3.8 Circular field applicator insert of 2 and 3 cm diameter (left) and cork, Perspex and Teflon materials used for inhomogeneity measurements (right).

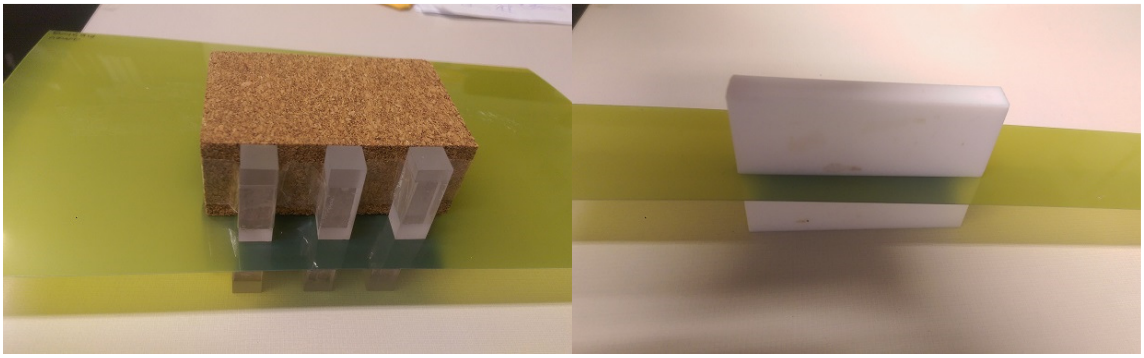

Figure 3.9 Ribs and lung (left) and skull (right) phantom fixed on both sides of the EBT3 film for inhomogeneity measurements.

3.11 Treatment planning calculations

To simulate the measurement setup in XiO, a water equivalent phantom of 30 x 30 x 30 cm was created for the standard field, obliquity and small circular field measurements. For the inhomogeneity measurements, the same configuration of cork, Perspex and Teflon materials were created with the dimensions as shown in Figure 3.10. The relative electron density (RED) assigned to each of these materials are specified in table 3.1.

The XiO eMC algorithm V4.80.03 was used for all calculations. The XiO eMC dose calculation parameters, as described in section 2.4, were established at the time of commissioning and are listed in table 3.2. Whilst the MRSU of 2% is used clinically, for the purpose of this work, a goal MRSU of 1% was used to reduce the statistical uncertainty. Dose to water was calculated for all field geometries to mimic the dose delivered to the film which is calibrated to provide dose to water. Depth doses for all electron energies (6, 9, 12, 15 and 18 MeV) were calculated for the reference field size of 10 x 10 cm^2 at 100 cm SSD. The calculated depth doses for the reference field were compared against ionisation chamber depth dose measurements.

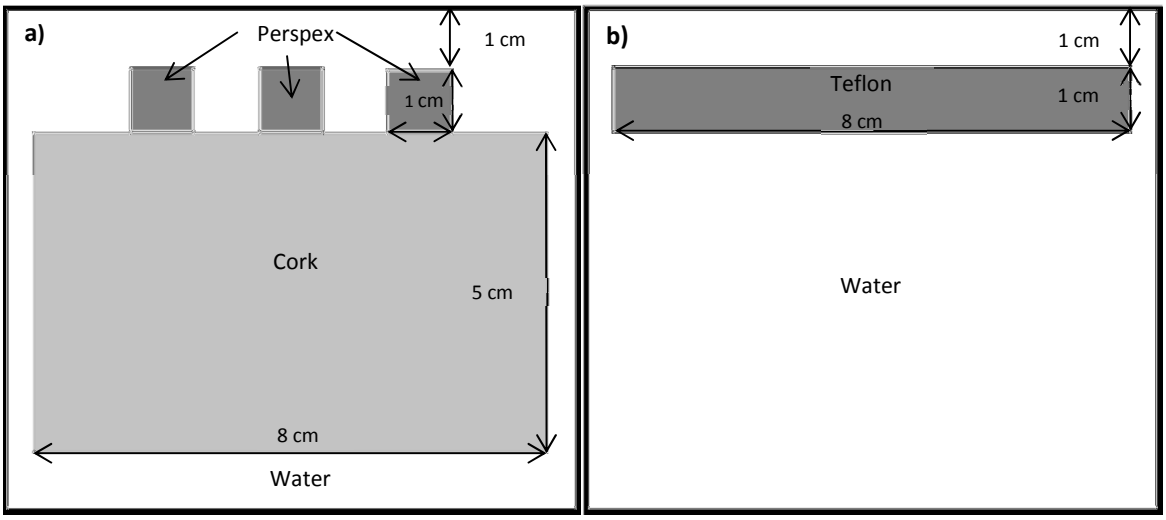

Figure 3.10 Phantom configurations created in XiO for (*a*) Rib and lung phantom consisting of Perspex and cork and (*b*) skull phantom made from Teflon.

Table 3.2 XiO eMC and dose calculation parameters used clinically.

Parameter	Values
Maximum number of histories	1.00E+12
Goal MRSU	2%
MRSU threshold	50%
Dose update interval	500000
Random number generator seed	1802
Calculation grid size	0.2 cm
Calculated absorbed dose	Water/ Medium

Calculations were performed for three out of the five electron energies available at our institution (6, 12 and 18 MeV). For standard field calculations, beams were created for a 10 x 10 cm^2 field at 100 cm SSD. For oblique beams, the dose for a 6 x 6 cm^2 field at 105 cm SSD for gantry angles of 0°, 25° and 45° was calculated. Calculations of small circular field sizes were performed for 2 and 3 cm diameter inserts for 6 MeV and 3 and 6 cm diameter inserts for 12 and 18 MeV using a 6 × 6 cm^2 electron applicator at 100 cm SSD. Inhomogeneity calculations were done for two configurations as shown in figure 3.10. Figure 3.10 (*a*) is a water phantom containing heterogeneities mimicking ribs overlying lung tissue. Figure 3.10 (*b*) contains a heterogeneity mimicking the bone underlying the scalp. The inhomogeneity materials were placed at a depth 1 cm from the surface of the phantom. For the inhomogeneity calculations, the grid size was reduced to 0.1 cm to provide better spatial resolution and interpretation at the interface. Dose-to-medium was also calculated within the other materials for comparison with XiO converted dose-to-water and film derived dose-to-medium.

The calculated 2D distributions were exported to file (.txt) from XiO and directly imported to SNC Patient software using the CMS XiO file format option.

RESULTS

4.1 XiO eMC commissioning and validation

The XiO eMC beam models were generated from the measured beam data by ELEKTA CMS software. The PDD curves were used to determine the energy spectrum of each beam. The measured output factors were used to match applicator output factors during beam modelling. The computed dose distributions were matched to measured data and reports were generated for each energy and applicator at 100 cm SSD and at extended SSD of 110 cm. An example of the report is shown in Appendix B. ELEKTA claims that the generated beam models achieve 2% / 2 mm accuracy throughout most of the dose distributions. This section aims to validate the accuracy of the beam model by comparing the measured and XiO calculated depth dose curves and profiles. The depth dose curves are normalised to 100% at the maximum and profiles at D_{max} are normalised to their central axis value. Only 6, 12 and 18 MeV depth dose curves and profiles of a 10 x 10 cm^2 field defined by an electron applicator are included in this section. For validation purposes, all XiO doses were calculated with dose-to-water in a 30 cm^3 homogeneous phantom created in XiO. The calculation voxel size used in this study was 0.2 cm^3. The statistical uncertainty was set to 1% and the number of histories of 1.00 E+12 was used in all the calculations.

4.1.1 Percentage depth dose

Figure 4.1 shows the measured and XiO calculated percent depth dose curves for a field defined by a 10 x 10 cm^2 applicator for electron beam energies of 6, 12 and 18 MeV. Beyond the depth of maximum dose, excellent agreement of less than 0.5 mm between measured and calculated is seen across all electron energies. Discrepancies between measurements and calculations are observed near the surface and this could be due to the lack of resolution from the PPC05 ionisation chamber.

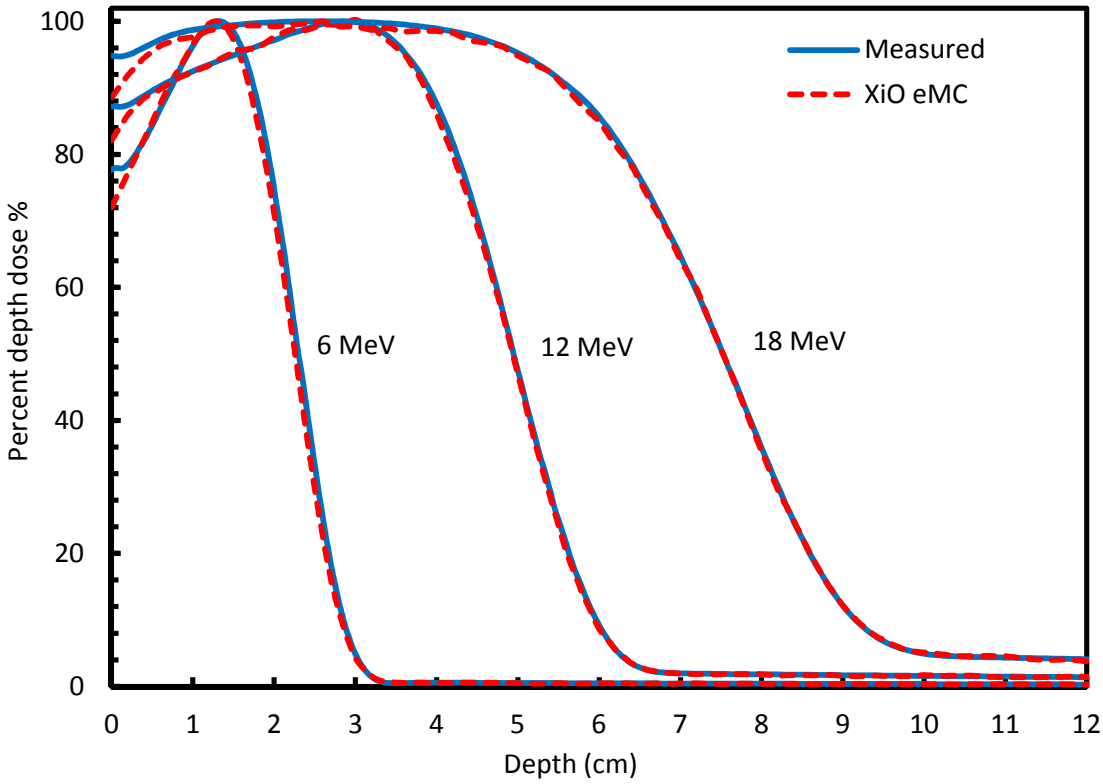

Figure 4.1 Comparison of measured and eMC calculated central axis depth dose curves for electron beam energies of 6, 12, and 18 MeV defined by a 10 x 10 cm^2 electron applicator.

4.1.2 Lateral Profiles

The lateral dose profiles were acquired at various depths specified in the beam data collection list (Appendix A) and were compared to the water tank measurements. In-plane profiles were excluded as Blue Phantom 2 scans show that the in-plane and cross-plane symmetry to be similar, where the difference between the two is very minimal at the shoulder of the profiles. Figures 4.2 (a) – (c) shows the comparison between measured and XiO calculated cross-plane dose profiles for 6, 12 and 18 MeV defined by a 10 x 10 cm^2 field. The profiles were measured and calculated at SSD of 100 cm. The measured and XiO calculated dose profiles are in good agreement of less than 1 mm at the penumbra region.

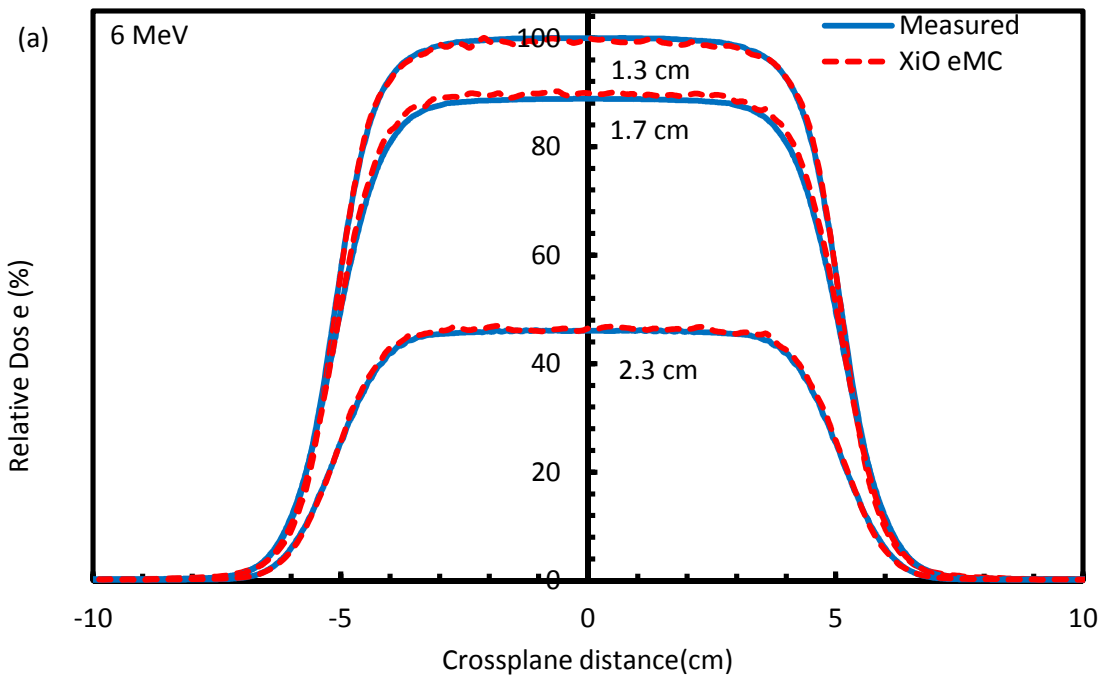
(a)
6 MeV
Measured
XiO eMC
1.3 cm
1.7 cm
2.3 cm
Relative Dos e (%)
100
80
60
40
20
0
-10
-5
0
5
10
Crossplane distance(cm)

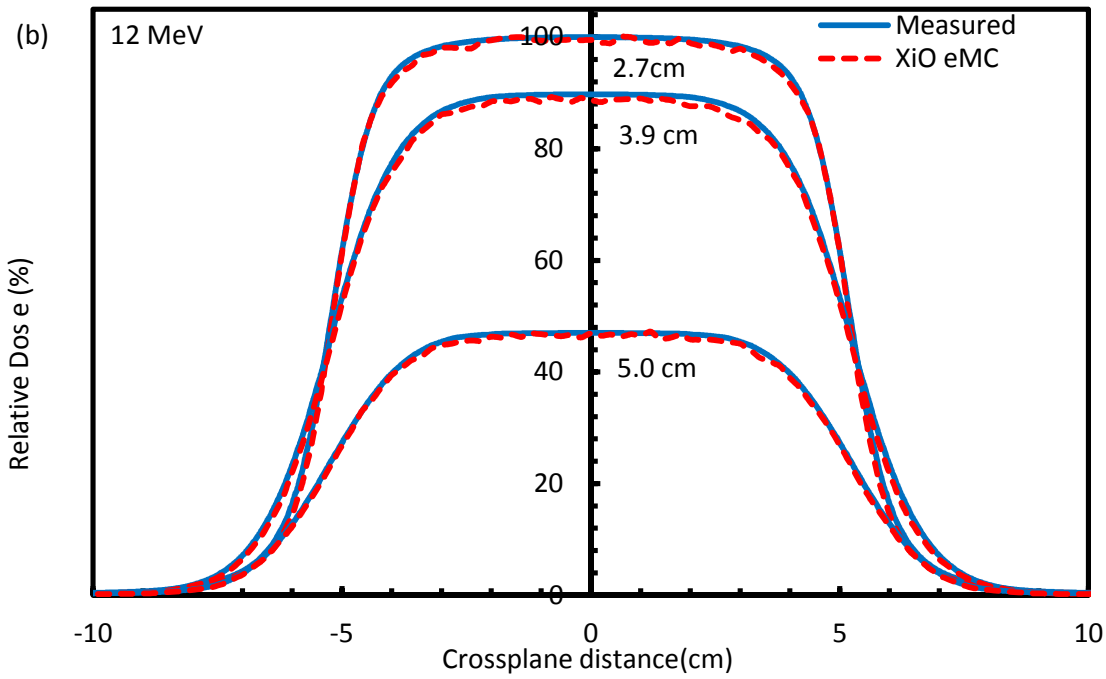
(b)
12 MeV
Measured
XiO eMC
2.7cm
3.9 cm
5.0 cm
Relative Dos e (%)
100
80
60
40
20
0
-10
-5
0
5
10
Crossplane distance(cm)

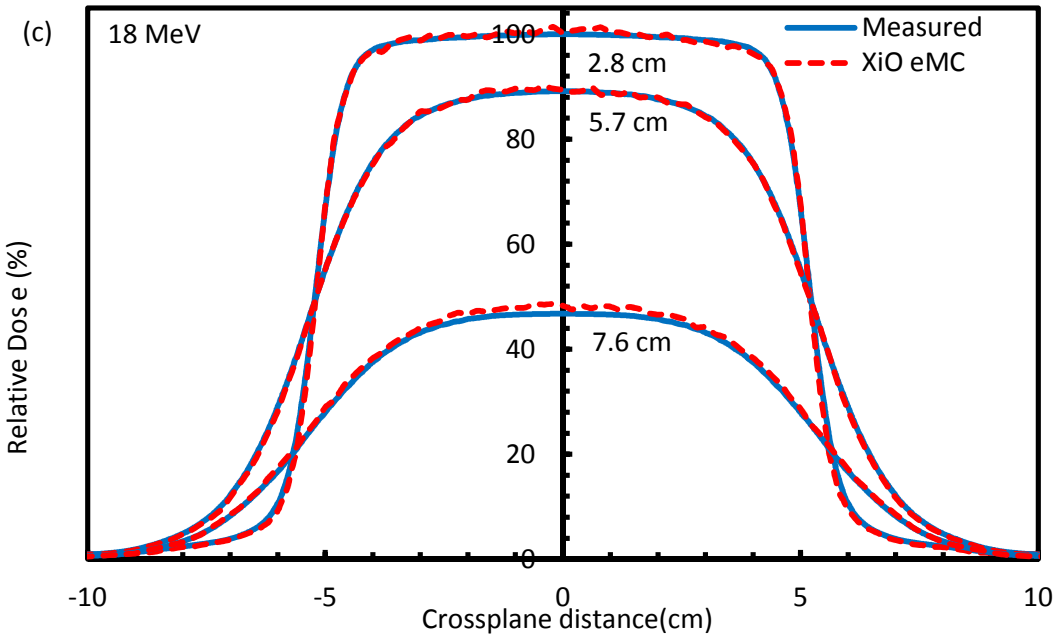

Figure 4.2 Comparison of measured and calculated XiO cross-plane dose profiles at depths of D_{max}, R_{90}, and R_{50} for (a) 6 MeV, (b) 12 MeV and (c) 18 MeV with a 10 x 10 cm^2 applicator defined field.

4.1.3 Output factors

The output was measured and the accuracy was validated at the depth of dose maximum for all electron energies with a range of circular, oval and square cut-out shapes. The output factors were single measurements; however, they were compared to reference data measured on two matched linear accelerators within the organisation. The agreement between measured and reference data are within -0.2 ± 1.0% (2SD). Good agreement is seen overall between measured and calculated output factors. There is a slight increase in output factor for the 6 MeV beam from 6 cm to 7 cm field size where the applicator size changes from 6 x 6 cm to 10 x 10 cm. This is due to the greater sensitivity to changing applicator scatter at this energy. The same jaw sizes are used for the 6 x 6 cm and 10 x 10 cm applicator. Only circular field output factors are shown in figures 4.3 (a) – (c) for 6, 12 and 18 MeV. The results obtained for the other energies and cut-out shapes are similar in comparison. The calculation voxel size of 2 mm was used in all cases. The statistical uncertainty in the calculation was less than 1%. The agreement between calculated and measured output factors are all within 2% except for the smaller field sizes for energies above 12 MeV.

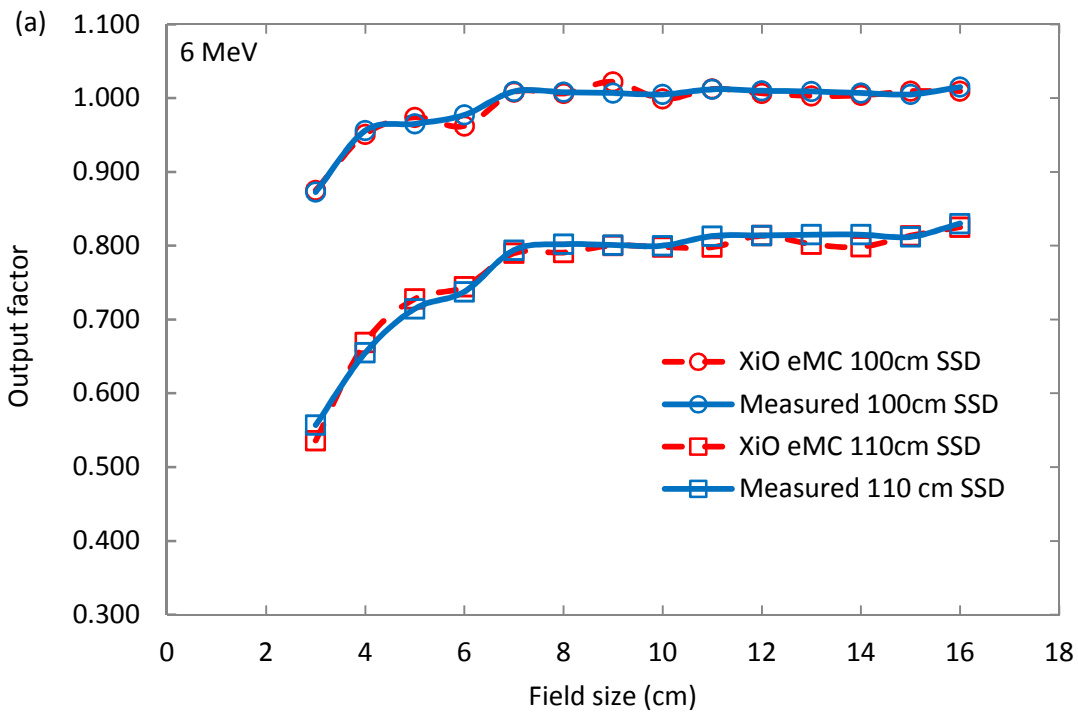
(a)
6 MeV
Output factor
1.100
1.000
0.900
0.800
0.700
0.600
0.500
0.400
0.300
0
2
4
6
8
10
12
14
16
18
Field size (cm)
XiO eMC 100cm SSD
Measured 100cm SSD
XiO eMC 110cm SSD
Measured 110 cm SSD

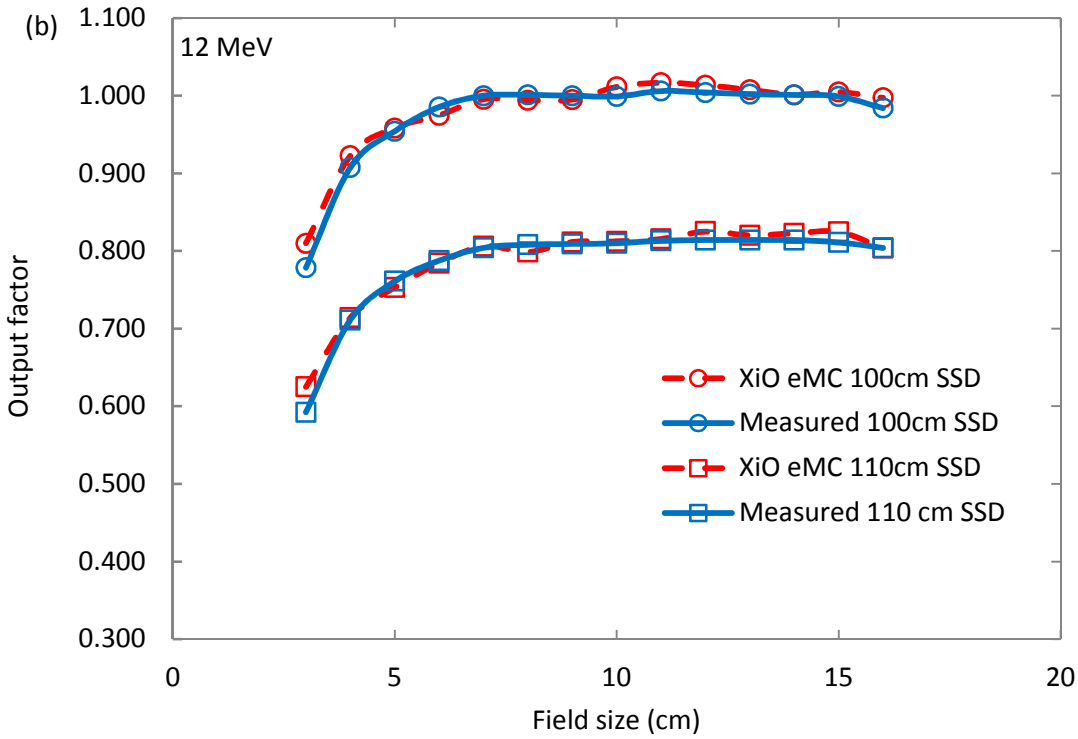
(b)
12 MeV
Output factor
1.100
1.000
0.900
0.800
0.700
0.600
0.500
0.400
0.300
0
5
10
15
20
Field size (cm)
XiO eMC 100cm SSD
Measured 100cm SSD
XiO eMC 110cm SSD
Measured 110 cm SSD

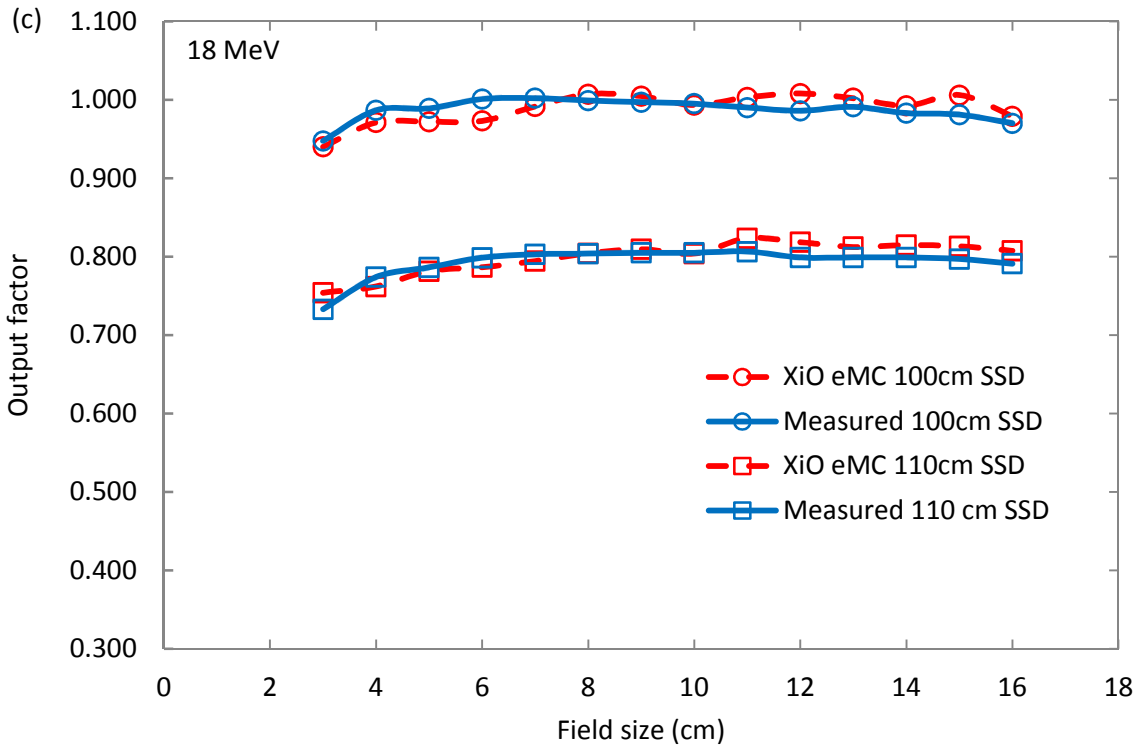

Figure 4.3 Comparison of measured and calculated output factors for 100 and 110 cm SSDs for (a) 6, (b) 12 and (c) 18 MeV electron beam.

4.2 Film Calibration

During film calibration, the linear accelerator output for the 12MeV beam was measured and yielded a result of 1.009 cGy/MU. The film was irradiated with a range from 10 to 600 MU. Figure 4.4 shows the dose response curve averaged from the two repetitions which was scanned using the red channel. Repeat calibrations from the same batch of film showed that the uncertainty in film response at doses of 10 and 600 cGy are ±10% (2σ) and ±2% (2σ) respectively. When the uncertainty in scanner response and the uncertainty in the calibration doses, measured according to TRS 398, are taken into account the total uncertainty in the film measurement at 10 and 600 cGy is ±12% (2σ) and ±4% (2σ) respectively. This is similar to results reported by Sorriaux *et al.,* the total uncertainty is close to ±3% (2σ) at 200cGy for 6MeV electrons with EBT3 (Sorriaux *et al.*, 2013). Similarly to Sorriaux *et al.*, only two repetitions of electron calibration with the same batch of films were performed whereas three repetitions would have improved the estimate of the uncertainty.

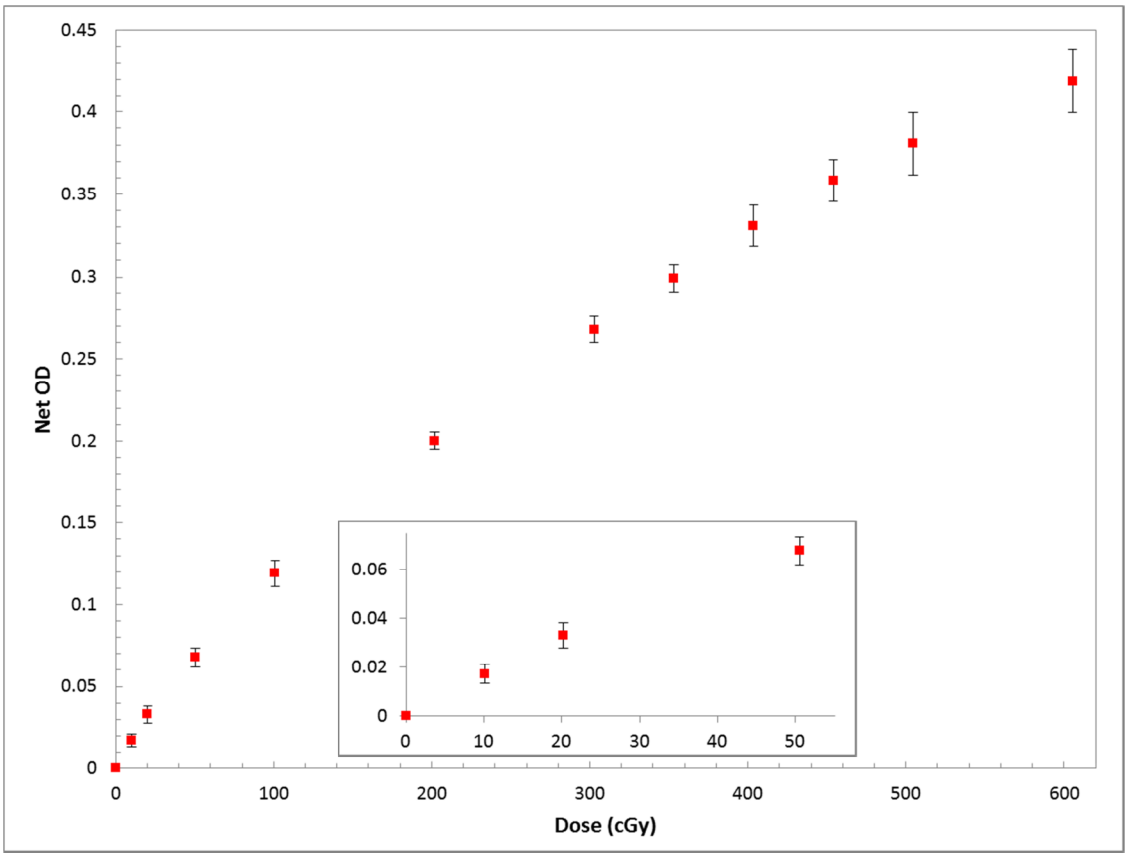

Figure 4.4 Dose response curve of Gafchromic® EBT3 film in the red channel. Dose dependent error bars of ±2σ are shown.

4.3 Film method validation

4.3.1 Ionisation chamber and EBT3 film comparison

To confirm the validity of the film dose distribution, a lateral profile film measurement was compared to water tank measurements using a CC13 ionisation chamber. Measurements were performed with a 12 MeV electron beam defined by a 10 x 10 cm^2 square field at 100 cm SSD. The results are presented in figure 4.5. The lateral profiles agree to within 0.5mm within the penumbra region.

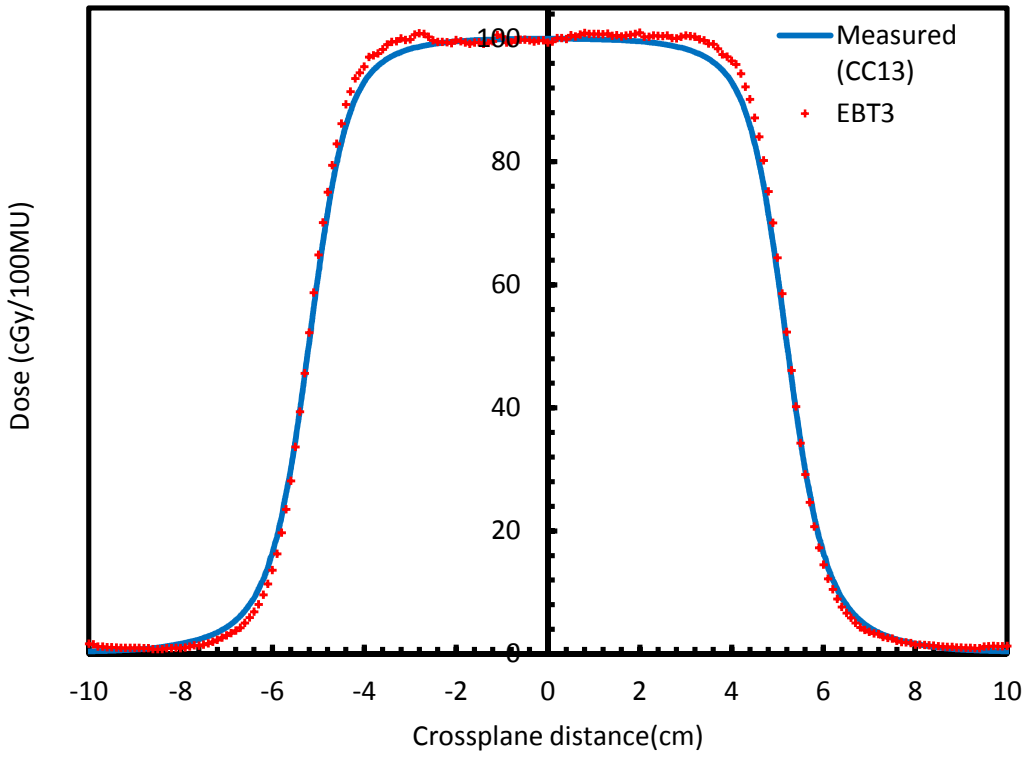

Figure 4.5 Comparison of a lateral profile at D_{max} between CC13 ionisation chamber and film for a 10 x 10 cm^2 field with standard insert at 100 cm SSD.

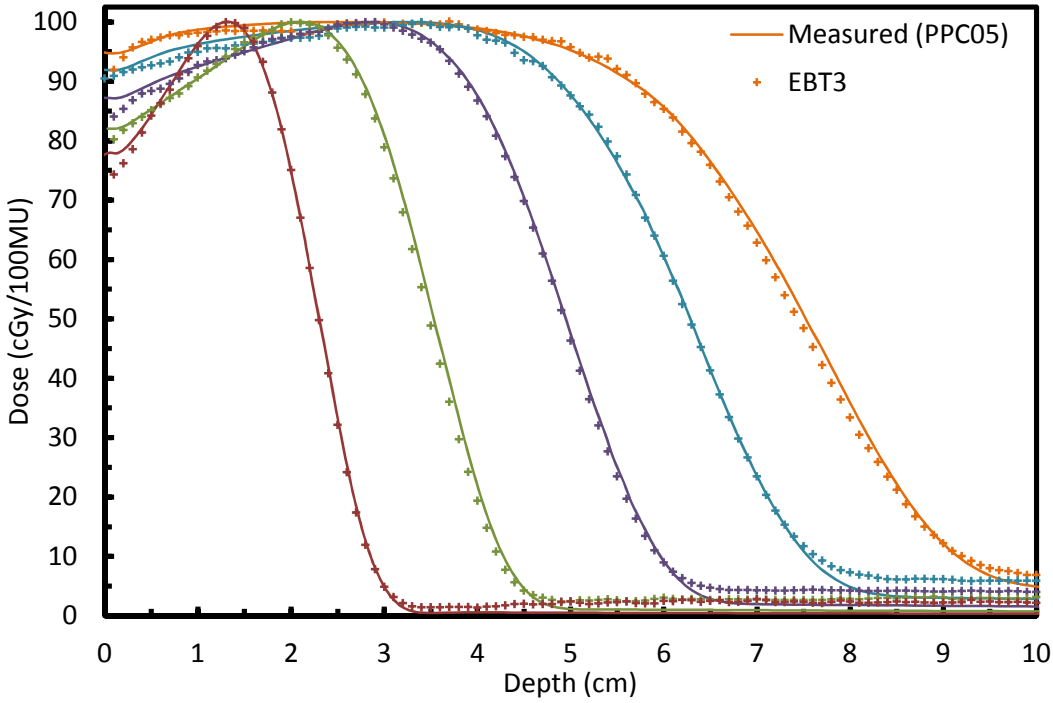

Figure 4.6 Depth dose profile comparison between PPC05 ionisation chamber and film for 6, 9, 12, 15 and 18 MeV in a 10 x 10 cm^2 field with standard insert at 100 cm SSD.

A similar comparison was performed for the depth dose profile. The water tank measurements were taken using a PPC05 plane parallel ionisation chamber. The film was placed vertically using the water tank setup method mentioned in section 3.2. Figure 4.6 shows the depth dose comparison between PPC05 ionisation chamber and EBT3 film. The agreement between EBT3 and PPC05 absolute depth dose profiles were within 2% or 2 mm. Slightly larger difference of up to 3% were seen in the region around D_{max} and near the surface. Discrepancies of up to 2% of the max dose were also observed at the low dose Bremsstrahlung tail.

There is almost 100% difference of local dose seen in the low dose Bremsstrahlung tail of figure 4.6. Sorriaux *et al.* showed a difference in EBT3 response between electrons and photons at low dose, with photon response being consistent with the findings of this work for the same dose level (Sorriaux *et al.*, 2013). This is a likely explanation of why EBT3 doses are almost double the PPC05 doses in the Bremsstrahlung tail when a calibration curve based on electron doses is used in this region.

4.3.2 Effect of film rotation

The effect of film orientation was investigated by irradiating two pieces of film, one in the cross-plane and the other in the in-plane orientation with a 12 MeV at 45° beam angle defined by a by a 10 x 10 cm^2 field. The central axis depth doses were extracted from both films and plotted on the same graph, normalising at the maximum dose. The relative depth dose comparison in figure 4.7 shows good agreement to within 2% or 0.5 mm between the transverse and sagittal orientation. This is of the same order as the combined measurement and scanning uncertainty, indicating that there is very little orientation dependence and radiochromic film attenuation is very similar to water.

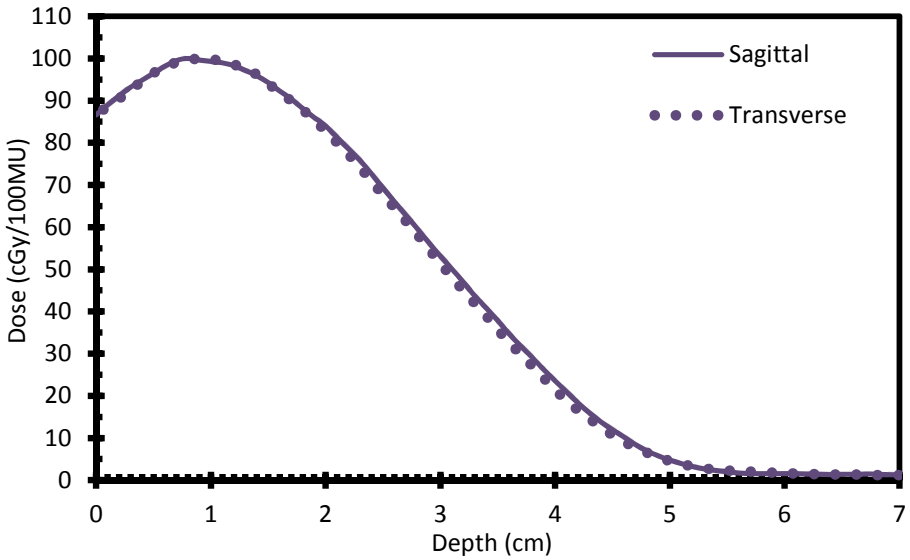

Figure 4.7 Depth dose comparisons between cross-plane and in-plane film orientation irradiated with a 12 MeV at 45° beam angle defined by a 10 x 10 cm^2 field.

4.3.3 Film scanning validation

The variation of optical density for unexposed film was found to be less than 0.5%. A very small variation in scanner response in the direction orthogonal to the scan direction was observed. This variation was 0.02% per mm, or a maximum of less than 2% for the largest fields scanned in this work. Both of these effects are small and are accounted for in the overall uncertainty of the measurement and scanning process.

4.4 Uncertainty of Methods analysis

The reproducibility of the film measurement and processing method was investigated. The scanner, measurement and software analysis uncertainty is reported in this section. All uncertainty results were calculated to 2 standard deviation (2σ).

4.4.1 Scanner uncertainty

The scanning component of the analysis method was investigated with a single film scanned five consecutive times. The mean and uncertainty of the dose at D_{max} for this film was 356.97 ± 1.11 cGy (2σ) or 356.97 cGy ± 0.31% (2σ). This represents the

uncertainty on the dose measurement due to the scanning process. All distance measurements from the five scans, namely D_{max}, R_{90}, R_{50} and RW_{50}, were identical to within 0.1 cm i.e. the resolution of the SNC Patient software.

4.4.2 Measurement uncertainty

The reproducibility of the measurement was assessed by comparing five films irradiated under identical conditions in the same measurement session. The mean and uncertainty of the dose at D_{max} was observed to be 356.95 ± 1.86 cGy (2σ) or 356.95 cGy ± 0.52% (2σ). Results from the repeat calibration showed that the uncertainty in film response at low doses of 10cGy to 20cGy is close to ±9.5% (2σ) whilst the uncertainty at doses of 200 to 600 cGy is ±2.5% (2σ).

Measurements of D_{max}, R_{90} and R_{50} were 1.22 ± 0.09 cm (2σ), 1.66 ± 0.06 cm (2σ) and 2.26 ± 0.05 cm (2σ) respectively. The mean and uncertainty of RW_{50} was 2.90 ± 0.02 cm (2σ). These results represent the combined measurement and scanning uncertainty.

4.4.3 Total uncertainty

The total uncertainty in the film measurements includes the scanner and measurement uncertainties discussed above as well as the uncertainty in the calibration doses. These were measured using a parallel plane chamber according to TRS398 protocol with an uncertainty of 1.4% (IAEA, 2000).

Therefore the total uncertainty in the film measurements at doses of 10 to 20 cGy is ±10% (2σ) whilst the total uncertainty at doses of 200 to 600 cGy is ±3% (2σ).

4.4.4 2D Gamma Analysis uncertainty

The reproducibility of the reported gamma passing percentage was determined by comparing five films irradiated under identical conditions with the same XiO 2D computed data. The mean gamma passing percentage was 97.4 ± 1.15% (2σ).This result represents the overall uncertainty of the measurement, scanning and analysis.

4.5 CT number and Relative Electron Density

As required by XiO treatment planning system for dose calculations, the mean CT vs. RED curve was acquired during commissioning. The relative electron density (RED) is defined as the electron density (e/cm^3) for a particular medium divided by the electron density of water (3.343 E+23 e/cm^3). Figure 4.8 shows the CT to RED conversion curve generated independently at the time of commissioning for a Philips Brilliance Big Bore CT scanner (Philips Medical Systems, Cleveland, OH). The data points represent the mean CT number for the corresponding RED. There are two noticeable gradients of the linear fit on the conversion curve, one from RED of 0 to 1.15 and the other from 1.15 to 2.00. The non-linearity of the CT to RED curve is observed at the transition from water to muscle and bone densities. This is due to the change in atomic number which affects the proportion of beam attenuation by Compton versus photoelectric interactions (Khan, 2003). CT numbers bear a linear relationship with attenuation coefficients but not linear in the entire range of tissue densities and material compositions.

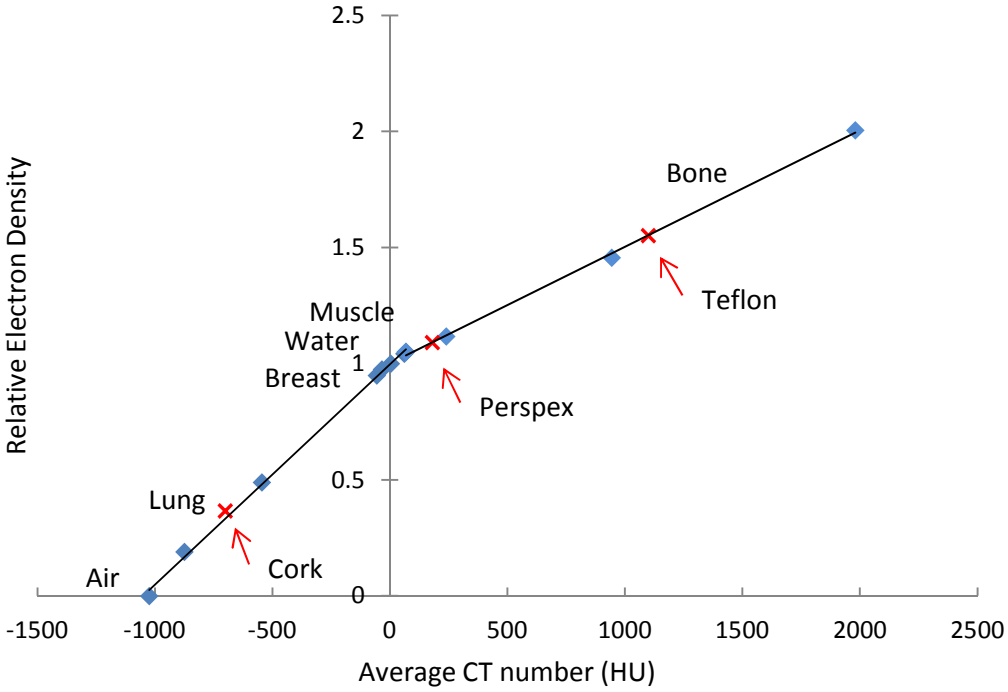

Figure 4.8 CT number to Relative Electron Density curve of materials in the CIRS Model 062 phantom for a Philips Brilliance Big Bore CT scanner. Red crosses indicate the calculated relative electron density of the materials used for inhomogeneity measurements.

The average CT numbers were extracted from the CT scans of the cork, Perspex and Teflon materials. The first trend line ranging from -1000 HU to 150 HU yield an equation of y = 0.001x + 1.00 and the second trend line ranging from 150 HU to 2000 HU yield an equation of y = 0.0006x + 1.07. The RED of the cork, Perspex and Teflon materials are calculated by the respective linear equation. As shown in table 3.1, the average CT numbers of -656.94 HU (cork), 109.66 HU (Perspex) and 913.75 HU (Teflon) yield a RED of 0.34, 1.13 and 1.61 respectively. The RED numbers were used to override the density of the phantom configuration created in the XiO treatment planning system.

4.6 Film measurement and comparison

Three of the five commissioned electron beam energies were investigated in this study. The electron Monte Carlo calculated depth doses and lateral profiles (1D) and dose distributions (2D) were compared to measurements with EBT3 film.

The reported percentage differences are calculated by comparing the dose difference at a point between measured and calculated which is normalised to the maximum dose. The agreement between XiO calculated and film measured depth doses were quantitatively assessed by determining the DTA at the depths of R90 and R50 on the central axis. The depth at R90 is known as the therapeutic range and it is often used to prescribe dose. R50 is the depth used to characterise the electron beam energy. DTA is used to compare the depth doses as steep dose gradients may result in a large percentage difference that is caused by a small difference in depth. The lateral profiles are analysed by comparing the radiological widths (the distance between 50% of the maximum dose) between XiO calculated and measured film profiles. To illustrate the difference between the dose distributions, a comparison of 2-D dose distribution and dose difference maps were used. Each dose difference map shows the film measured dose minus the XiO calculated dose. In the dose difference maps, blue indicates measured film is lower than calculated XiO dose and red indicates that film is higher than calculated XiO dose. The scales next to the 2-D dose distribution represent the dose levels in cGy and the scales next to the dose

difference maps represent the absolute dose difference between film measurement and XiO calculated dose distribution.

"Gamma" as described in chapter 3 allows a method for excluding dose-differences that are due to small spatial offsets in steep dose gradient regions, when those small offsets can be regarded as clinically insignificant. Gamma values of ≤ 1 constitute a pass. One indicator of overall agreement between two dose distributions is the number of pixels passing the gamma criteria. Figure 4.9 (a) shows the XiO dose distribution of 12 MeV, 45° oblique incident with blue regions indicate where the failing points lie when compared to film. The comparison criteria are 3% / 3 mm. In this example 4944 out of a total of 5212 points, passed the gamma criteria, yielding a gamma passing ratio of 94.9%. Figure 4.9 (b) shows these points in the form of a histogram with points that achieved a gamma value of less than 1 (green) and failing points where gamma is more than 1 (red). The comparison in figure 4.9 allow the differences to be observed, and calculating the gamma passing ratio gives a quantitative indicator of the magnitude of the agreement (or disagreement). In the AAPM TG-119 report, confidence limits were produced as baseline expectation for planar dose distributions. Recommended action levels for planar dose distributions expressed in terms of percentage points passing gamma criteria of 3%/3 mm is 90% for per-field measurements (Ezzell *et al.*, 2009).

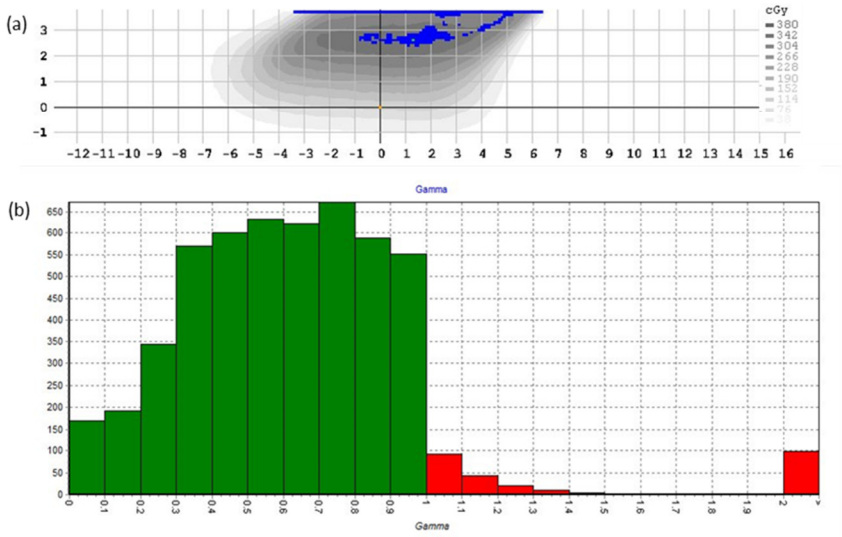

Figure 4.9 (a) XiO dose distribution of 12 MeV, 45° oblique incident with blue regions indicate where the failing points lie when compared to film. Comparison criteria are 3% / 3 mm. (b) A gamma histogram showing the number of passing points (green) and failing points (red).

4.6.1 Standard field measurements

Standard field central axis depth dose curves in figure 4.10 show good overall agreement. Surface dose agreed to within 0.5% for all beams for the 10 x 10 cm field at 100 cm SSD and agreement is mostly within 2%/2 mm beyond D_{max}. However, slightly larger dose difference of up to 3% is seen in the region around D_{max} for the 18 MeV, 10 x 10 cm^2 field. Figure 4.11 shows the comparison of film and XiO 2-D dose distribution and dose difference maps for 6, 12 and 18 MeV, 6 x 6 cm^2 and 10 x 10 cm^2 fields at 105 cm and 100 cm SSD respectively. It is observed that all measured film profiles were consistently narrower than the profiles from XiO. The left side of figure 4.11 shows the comparison between film and XiO 2D isodose distributions. The isodose distributions show good agreement to within 2 mm.

The right side of figure 4.11 shows the planar dose difference map for the isodose comparison on the left of the figure. For the 6 MeV beams, the largest differences were observed where the dose gradient shows the steepest fall-off. For all beams, differences are apparent at the edges of the field. These differences are a result of the limitation of the SNC Patient software that only allows shifts of 1 mm and above when matching dose distributions. This will be discussed further in Chapter 5. Dose prediction in the build-up region for XiO is not as accurate because depth doses are closely matched at D_{max} and beyond rather than in the build-up region during beam modelling. The gamma passing rates are above 90% for all fields except the 18 MeV, 10 x 10 cm^2 field which obtained a gamma passing rate of 85.6%.

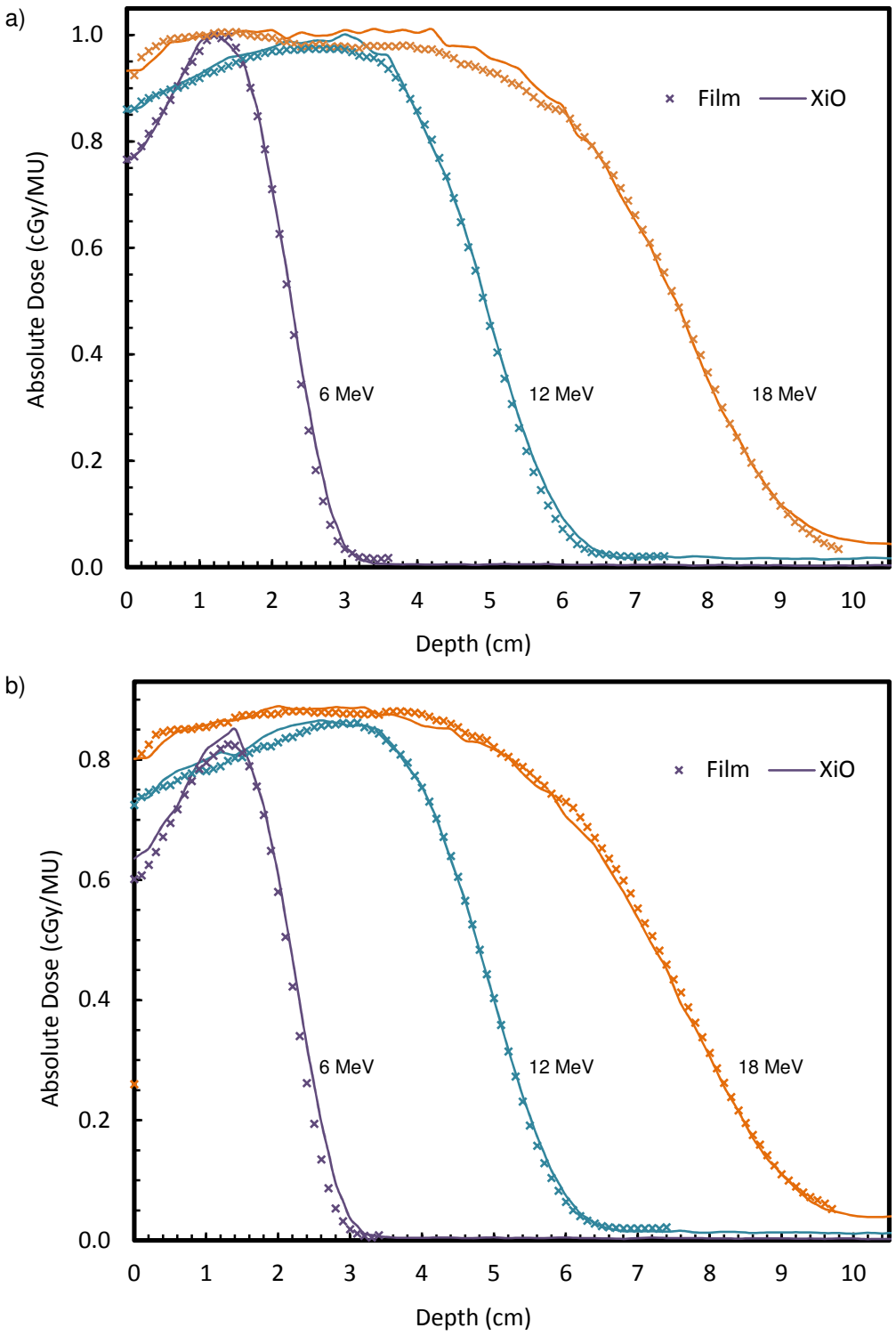

Figure 4.10 Comparison of film and XiO depth doses for 6, 12 and 18 MeV electron beams for (a) 10 x 10 cm^2 field, 100cm SSD and (b) 6 x 6 cm^2 field, 105 cm SSD.

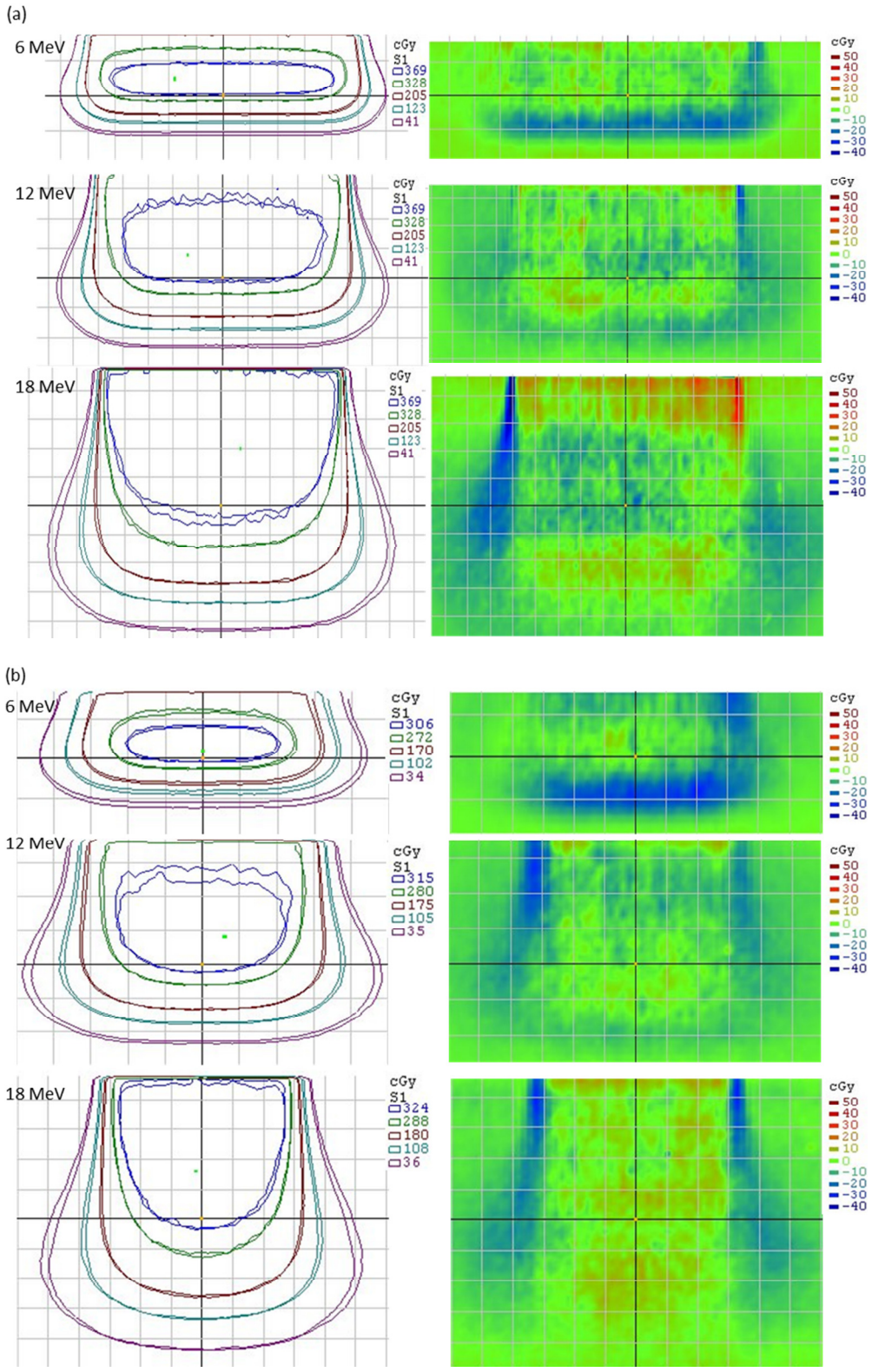

Figure 4.11 Standard field comparison of film and XiO 2-D isodose distribution (left) and dose difference maps (right) for 6 MeV, 12 MeV and 18 MeV, (a) 10 × 10 cm^2 at 100cm SSD and (b) 6 × 6 cm^2 field at 105 cm SSD. Blue represents film lower than calculated XiO dose and red represents film higher than calculated XiO dose. Grid size is 1 x 1 cm^2.

4.6.2 Obliquity measurements

Oblique field depth dose curves are shown in figure 4.12 which compares film and XiO central axis depth doses at 105cm SSD for 6, 12 and 18 MeV with a 25° and 45° beam angle. Agreement is mostly within 2% or 2 mm beyond D_{max}. However, larger differences are seen in the build-up region and D_{max} for the 45° beam angle, where the XiO dose is always higher than film dose for all energies. The largest difference of up to 8.9% is seen for 6 MeV. The XiO dose difference is observed to decrease with increasing beam energy. The largest oblique field radiological width difference of 1.1 mm was seen for the 12 MeV, 45° beam angle. Overall, the radiological widths were within 1 mm for all oblique fields.

Figure 4.13 shows the comparison between film and XiO 2-D dose distribution and dose difference maps for 6, 12 and 18 MeV electron beam, 105 cm SSD at 25° and 45° incident beam angle. The isodose lines show good consistency between measurements and calculations. Gamma passing rates are above 90% for a 3% / 3 mm gamma comparison criterion.

The dose difference map shown in figure 4.13 highlights where the differences are and failing points lie mostly in the build-up region and D_{max}. Minimal differences were observed at 25° incident beam angle as the gamma passing rates were well above 97%. However, for the 45° incident beam angle, large dose differences of up to 9% are seen in the build-up and D_{max} region. This is indicated by the blue region in figure 4.13 (b) where XiO dose is higher than film dose.

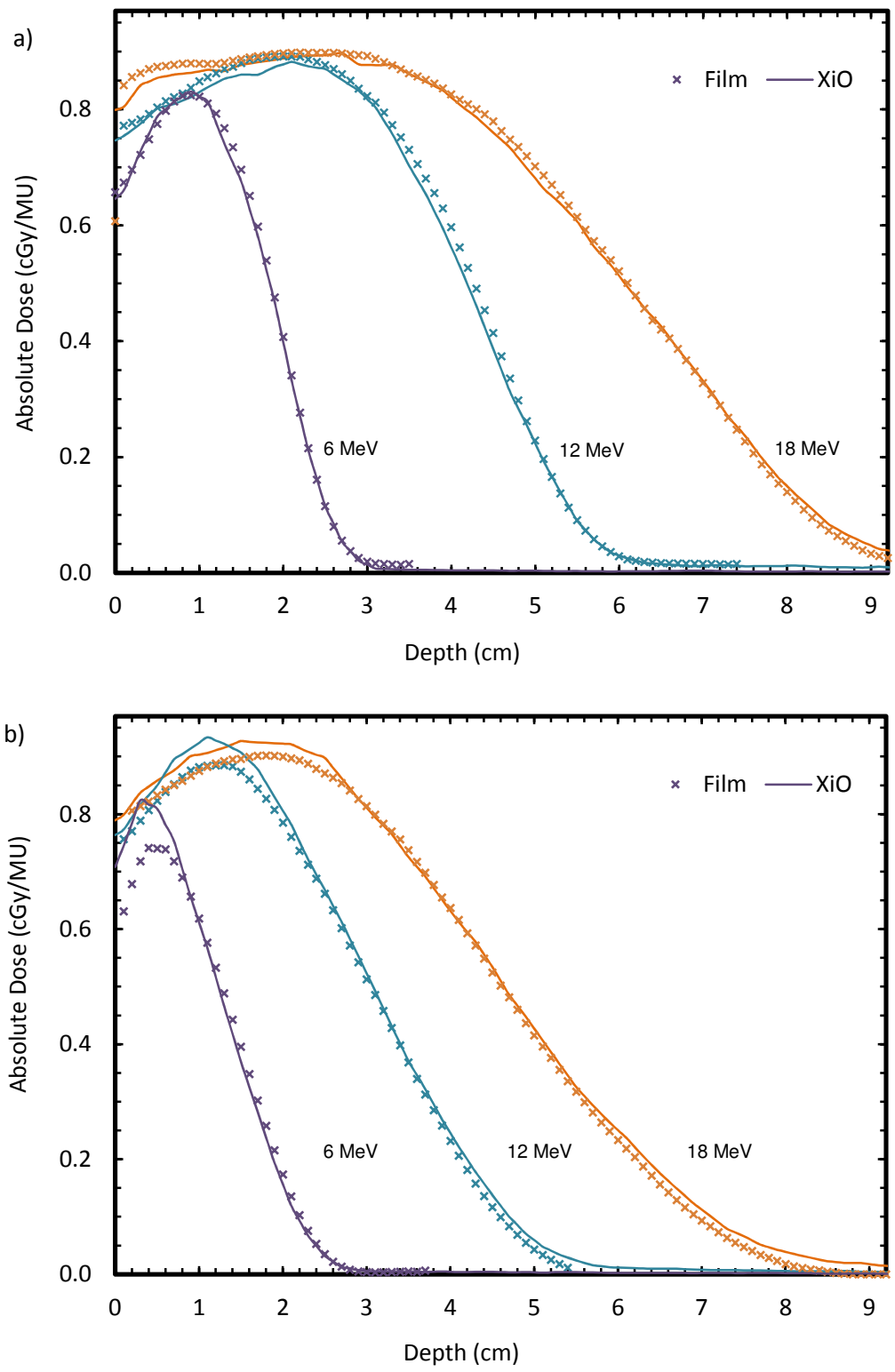

Figure 4.12 Comparison of film and XiO depth doses for 6, 12 and 18 MeV electron beam with 6 x 6 cm^2 field, 105cm SSD at a) 25° and b) 45° incident beam angle.

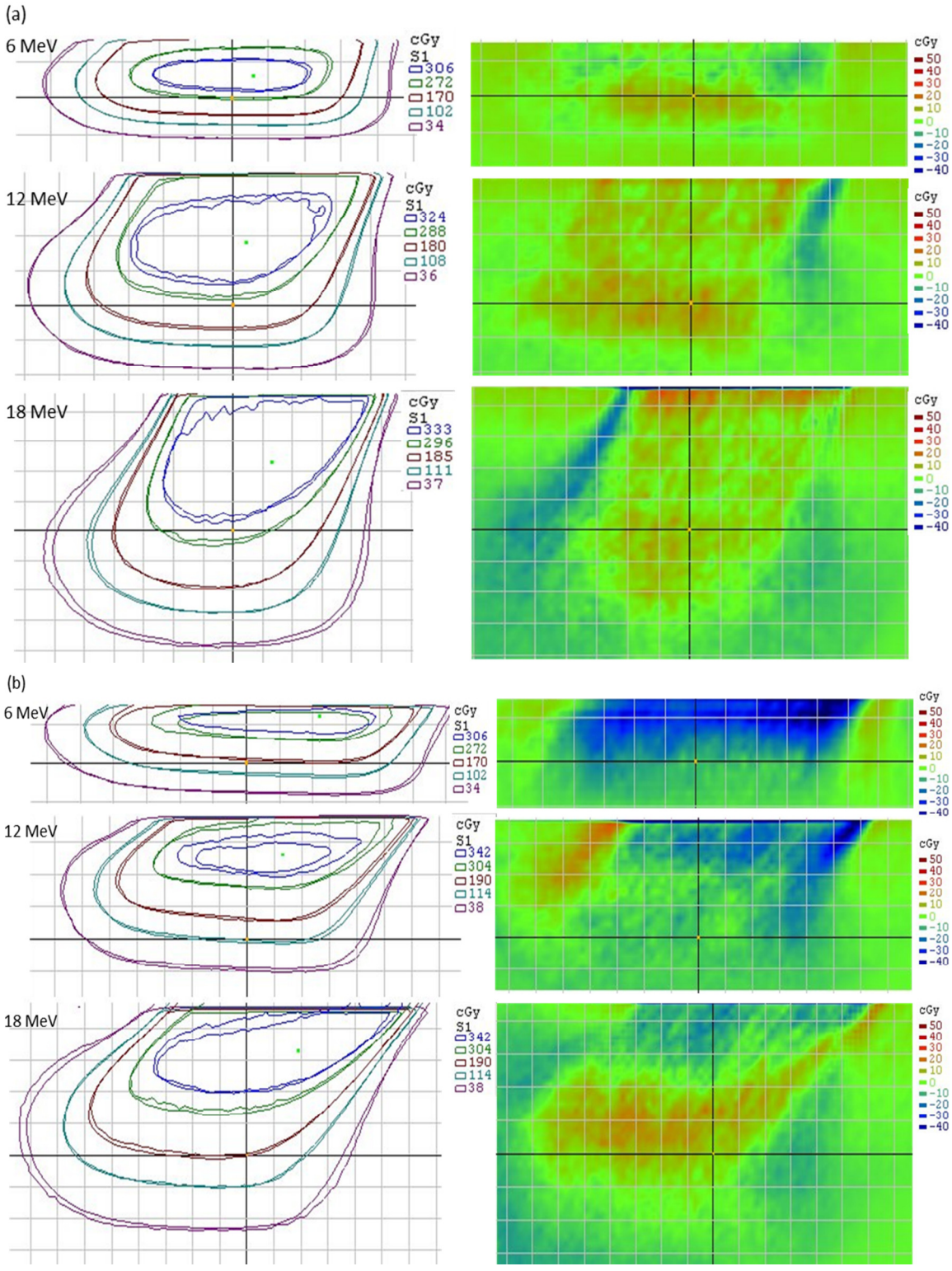

Figure 4.13 Oblique field comparison of film and XiO 2-D isodose distribution (left) and dose difference map (right) for 6 MeV, 12 MeV and 18 MeV, 6 × 6 cm^2 field, 105 cm SSD at (a) 25° and (b) 45° incident beam angle. Blue represents film lower than calculated XiO dose and red represents film higher than calculated XiO dose. Grid size is 1 x 1 cm^2.

4.6.3 Small Circular fields

Figures 4.14 and 4.15 show the comparison between film and XiO central axis depth doses for 2, 3 and 6 cm circular fields at 100 cm SSD for 6, 12 and 18 MeV beams. Overall, excellent agreement of within 1 % and 1 mm beyond the nominal D_{max} is observed. The largest difference for small circular field measurements is again apparent in the build-up region up to D_{max} where the dose difference of up to 5% for the 12 and 18 MeV beams were seen when compared to film. Overall, the film measured radiological widths for small circular fields were within 1 mm of XiO calculations.

Figures 4.16, 4.17 and 4.18 show the 2D dose distributions and dose difference maps for circular fields of 2, 3 and 6 cm diameter. Overall, good agreement is seen for the 6 MeV, 2 and 3 cm diameter field sizes. The largest dose difference of up to 5% for small circular field measurements is seen for the 12 and 18 MeV beam. Again, the differences are apparent in the build-up region, D_{max} and field edges. In figure 4.17(c), the lowest isodose line (40 cGy) shows the largest difference and is illustrated by the blue regions of the dose difference map indicating that dose to film is lower than calculated XiO dose. In figure 4.18(b), the dose difference in the build-up region is seen by the red regions of the dose difference map indicating that dose to film is higher than calculated XiO dose.

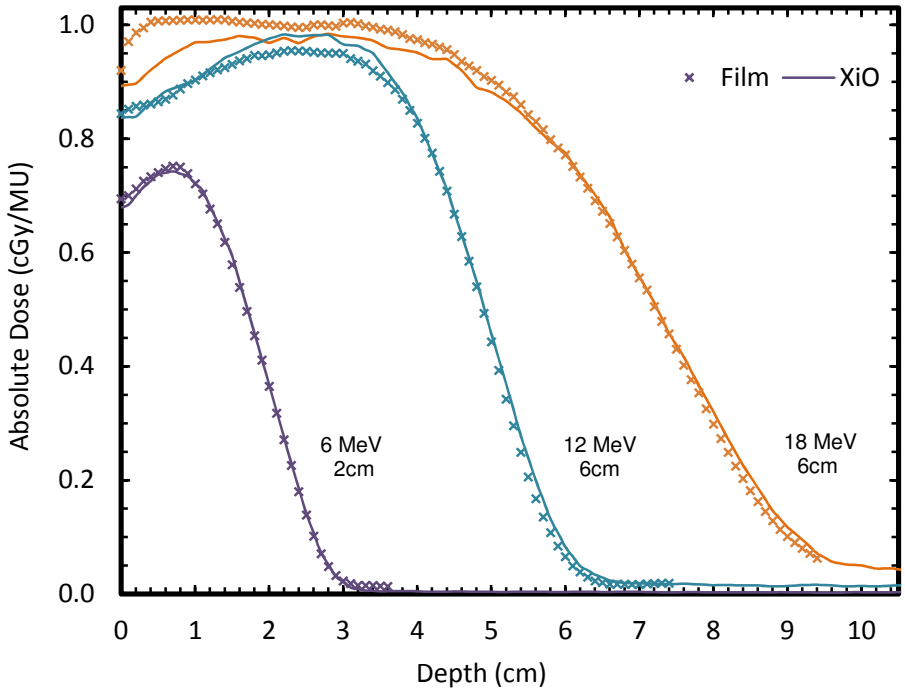

Figure 4.14 Comparison of film and XiO depth doses for 6, 12 and 18 MeV electron beam using 2 and 6 cm diameter circular fields at 100 cm SSD.

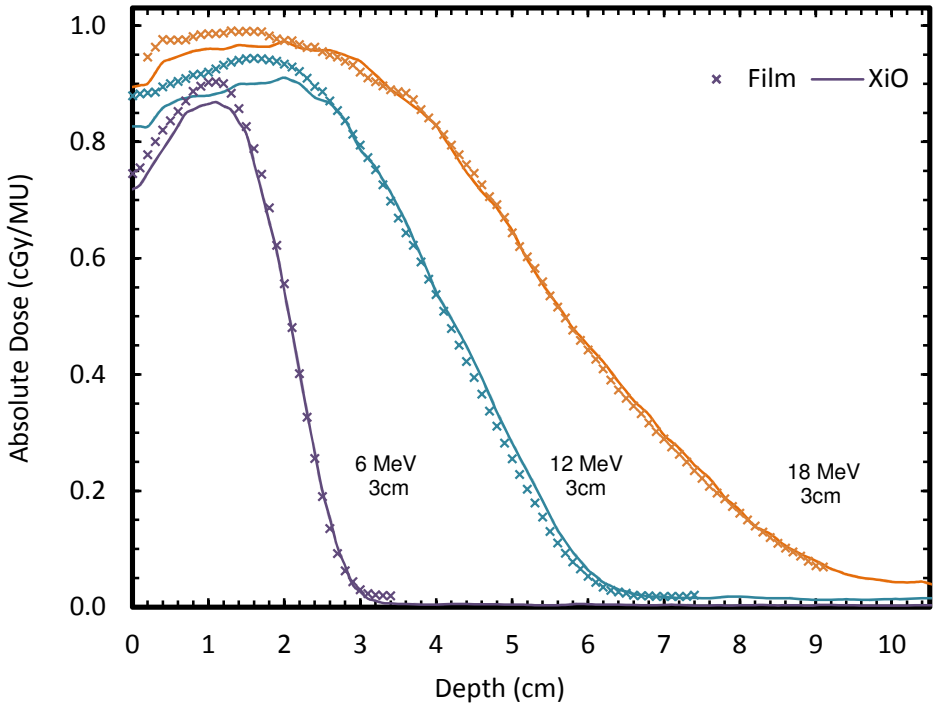

Figure 4.15 Comparison of film and XiO depth doses for 6, 12 and 18 MeV electron beam using 3 cm diameter circular fields at 100 cm SSD.

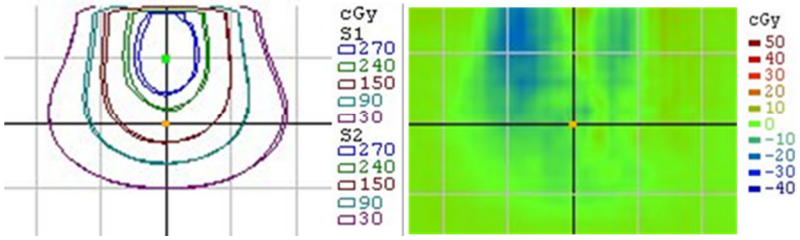

Figure 4.16 Small field comparison of film and XiO 2-D isodose distribution (left) and dose difference map (right) for 6 MeV, 2 cm diameter circular field at 100 cm SSD. Blue represents film lower than calculated XiO dose. Grid size is 1 x 1 cm^2.

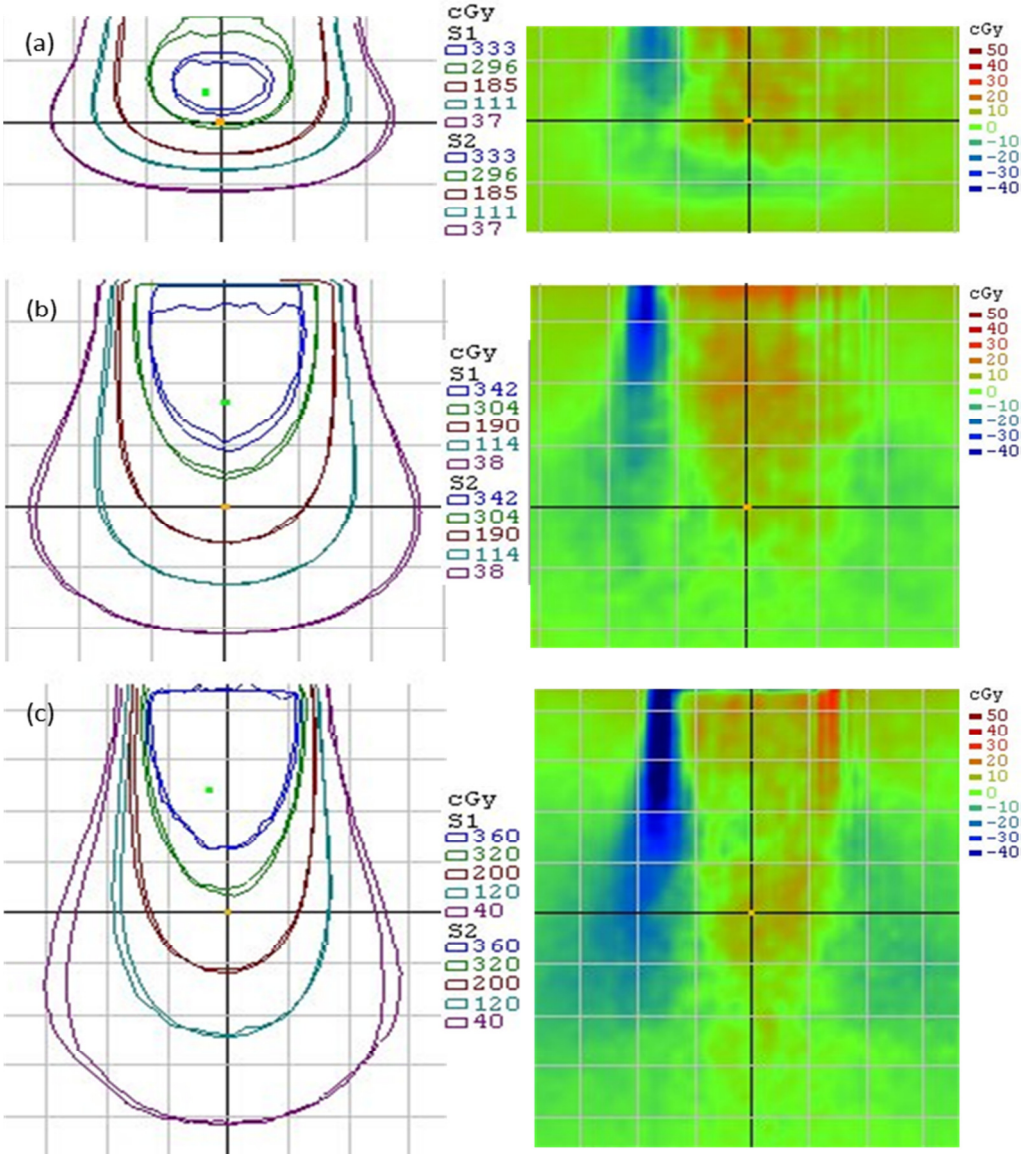

Figure 4.17 Small field comparison of film and XiO 2-D isodose distribution (left) and dose difference map (right) for (a) 6 MeV, (b) 12 and (c) 18 MeV, 3 cm diameter circular field at 100 cm SSD. Blue represents film is lower than calculated XiO dose and red represents film is higher than calculated XiO dose. Grid size is 1 x 1 cm^2.

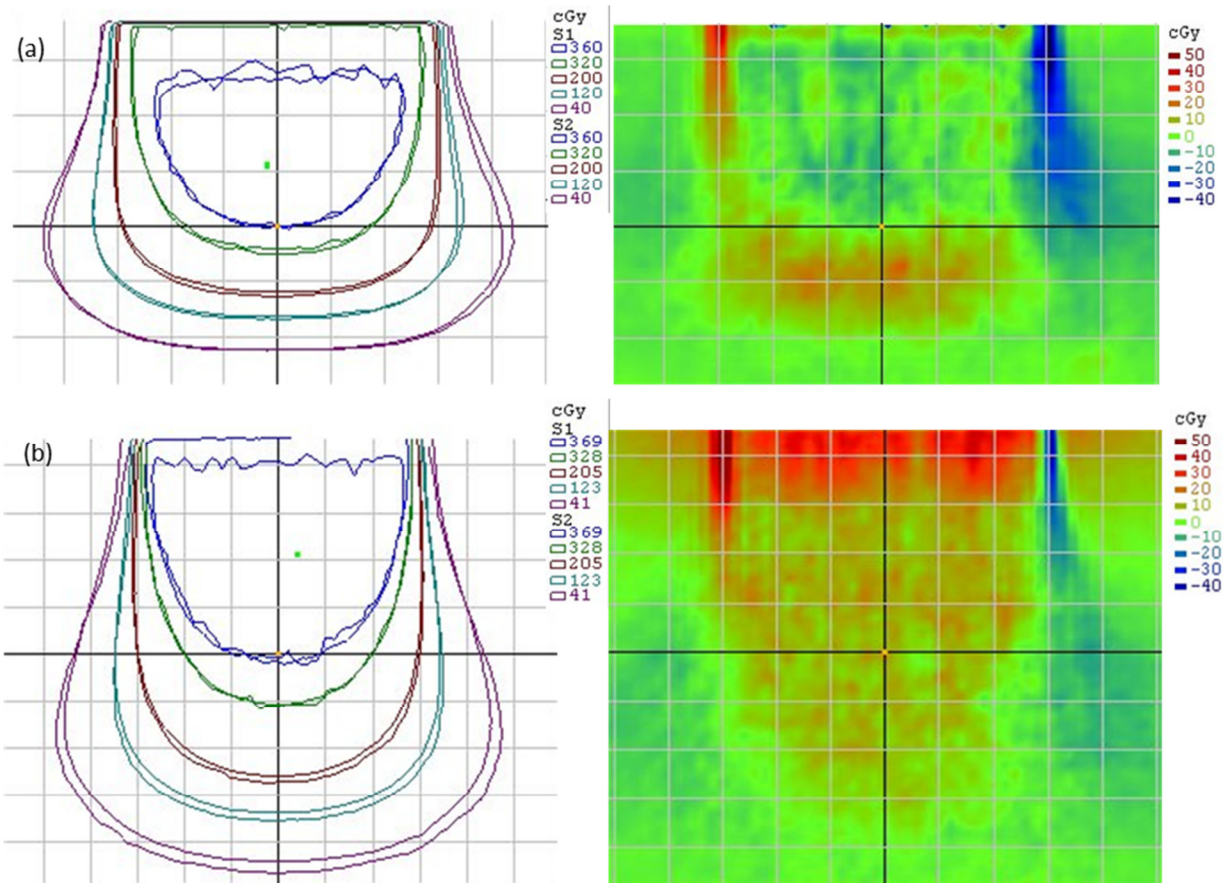

Figure 4.18 Small field comparison of film and XiO 2-D isodose distribution (left) and dose difference map (right) for (a) 12 MeV and (b) 18 MeV, 6 cm diameter circular field at 100 cm SSD. Blue represents film lower than calculated XiO dose and red represents film higher than calculated XiO dose. Grid size is 1 x 1 cm^2.

4.6.4 Inhomogeneity measurements

Figure 4.19 shows the central axis depth dose comparison between film, XiO dose-to-water and XiO dose-to-medium. The phantom materials of Perspex and cork that mimics ribs and lung are represented by the shaded areas on the depth dose curve. The 1 cm rib phantom is located at 1 cm depth in water followed by the 5 cm lung phantom. Figure 4.20 shows the central axis depth dose comparison between film, XiO dose-to-water, XiO dose-to-medium and "film derived" dose-to-medium. The Teflon material that mimics a skull is represented by the shaded area on the depth dose curve. The 1 cm skull phantom is located at 1 cm depth in water. Interpretation of the dose-to-water and dose-to-medium results is discussed in detail in chapter 5.

Figure 4.19 shows that XiO dose-to-water and XiO dose-to-medium agrees very closely in most regions with the exception of within the rib phantom. Here, XiO dose-to-medium is up to 2.5% lower than XiO dose-to-water – as would be expected with higher energy absorption in high density bone leading to lower absorbed dose (in the same volume). Within the rib, the film measurements of dose-to-water, is up to 6.6% lower than XiO dose-to-water. Up to 1 cm beyond the rib, the film measured dose is 5.9% higher than XiO dose-to-water. In both of these cases, differences outside the uncertainty of measured and calculated doses are observed. The "film derived" dose-to-medium is also shown in figure 4.19 and when compared to XiO dose-to-medium, a difference of up to 7.2% is observed within the rib phantom. In the lung phantom, a difference of up to 2.5% is seen between "film derived" dose-to-medium and XiO dose-to-medium.

Figure 4.20 again shows very close agreement between XiO dose-to-water and XiO dose-to-medium in regions of water. However, larger differences are seen in the high density Teflon of the skull phantom. Within the bone, XiO dose-to-medium is up to 13% lower than XiO dose-to-water. The film measurement agrees with XiO dose-to-medium to within the uncertainty of both measured and calculated dose in all regions. The "film derived" dose-to-medium is also shown in figure 4.20 and when compared to XiO dose-to-medium, a difference of up to 3.6% is observed at D_{max}.

Figure 4.21 shows the 2D dose distribution and Gamma dose difference maps for the film measurement and XiO dose-to-water results in the rib and lung and skull

phantoms. Film and XiO agree to within 7% inside the heterogeneities. Differences are predominantly near the interface between materials. These differences can be seen clearly on the dose difference maps in Figure 4.21.

Finally XiO dose-to-water and XiO dose-to-medium 2D dose distributions were compared for the skull phantom and are shown in Figure 4.22. Overall, there is good agreement between the two except for the region containing the skull phantom. The XiO dose-to-medium within the skull phantom is 10% lower than XiO dose-to-water. The Gamma criterion is set to 3%/3 mm. Figure 4.22 also shows the Gamma dose difference map where the blue regions indicate that dose-to-medium is lower than dose-to-water.

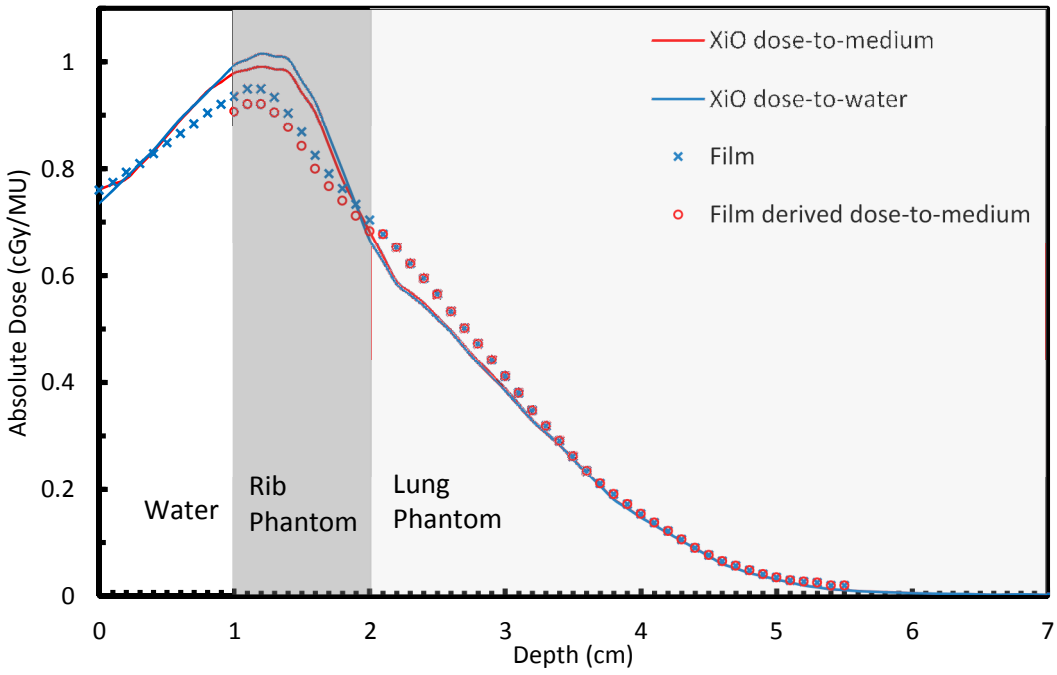

Figure 4.19 Comparison of XiO dose-to-medium, XiO dose-to-water and film and "film derived" dose-to-medium depth doses in the rib and lung phantom for a 6 MeV 10 x 10 cm^2 field at 100 cm SSD.

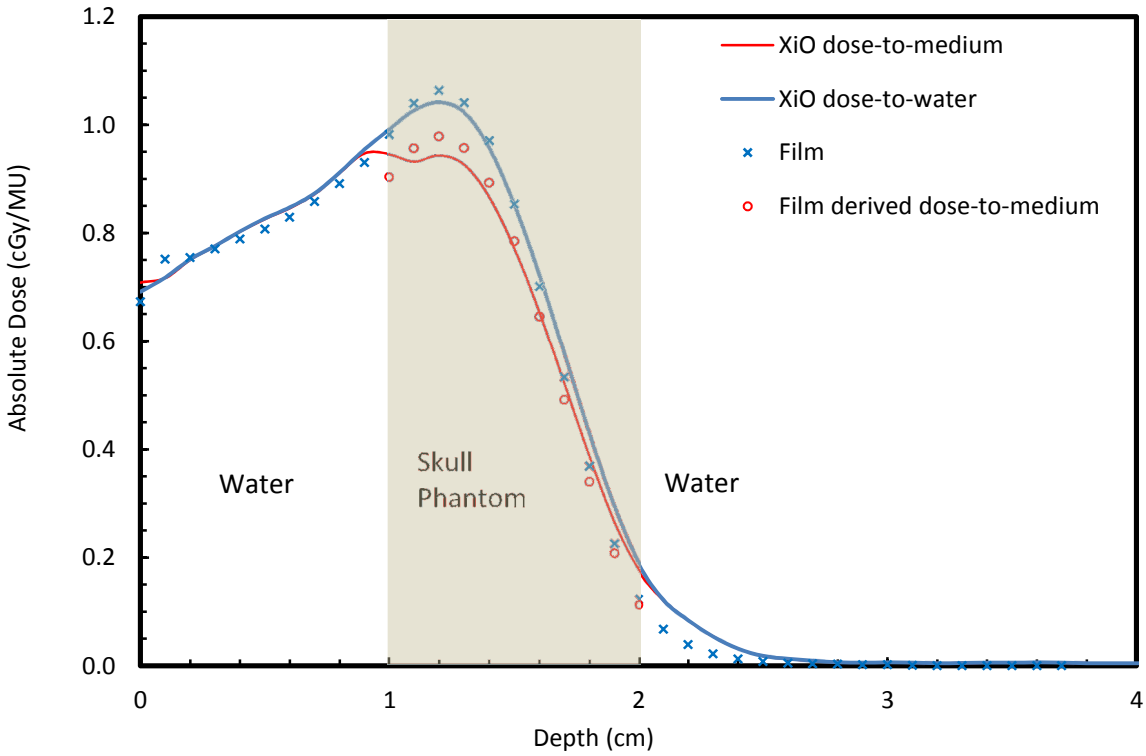

Figure 4.20 Comparison of XiO dose-to-medium, dose-to-water, film and "film derived" dose-to-medium depth doses in the skull phantom for a 6 MeV 6 x 6 cm^2 field at 100 cm SSD.

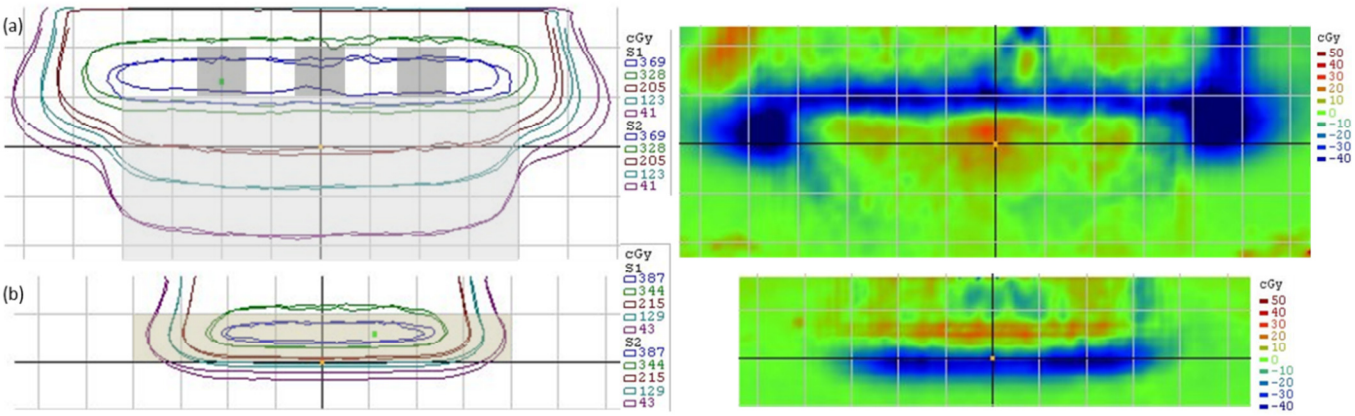

Figure 4.21 Comparison of 2-D dose distributions (left) and dose difference maps (right) for film and XiO dose-to-water for (a) rib and lung phantom (shaded blocks) irradiated with a 6 MeV, 10 × 10 cm^2 field at 100 cm SSD, and (b) skull phantom (shaded block) irradiated with 6 MeV, 6 × 6 cm^2 field at 100 cm SSD. Blue represents film is lower than calculated XiO dose and red represents film is higher than calculated XiO dose. Grid size is 1 x 1 cm^2.

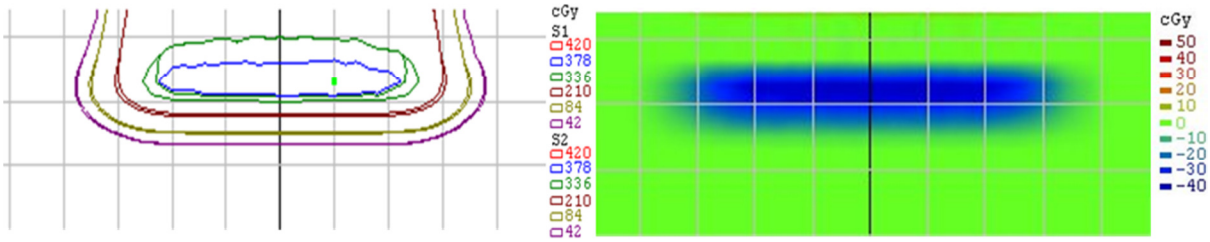

Figure 4.22 Comparison of calculated 2D dose distribution (left) and dose difference map (right) for XiO dose-to-water and XiO dose-to-medium in the skull phantom for a 6 MeV 6 x 6 cm^2 field at 100 cm SSD. Blue indicates the XiO dose-to-medium is lower than XiO dose-to-water. Grid size is 1 x 1 cm^2.

4.7 Measurement summary

A summary of the comparison metrics between calculated XiO and measured EBT3 film for all fields are shown in Table 4.1. Gamma analysis was performed for all fields using gamma pass criteria of 2% or 2 mm for standard fields and 3% or 3 mm for the oblique, circular and inhomogeneity fields. The gamma criteria align with recommendations stated in TRS 430 (IAEA, 2004). The dose difference at D_{max} was observed to be within ±2% for standard fields, ±8.9% for oblique fields, ±4.7% for circular fields and ±3.2% for inhomogeneity measurements. Overall, the distance to agreement (DTA) at depths of R_{90} and R_{50} were within 2 mm with the largest difference observed in the inhomogeneity measurements. The radiological width (RW_{50}) of the profile at the depth of D_{max} agreed to less than 1.6 mm with the largest error observed at extended SSD measurements.

Table 4.1 Comparison of EBT3 film to XiO for all measured fields.

Measurement (Gamma criteria)	SSD (cm)	Applicator (cm^2)	Setup	Energy (MeV)	Gamma passing rate (%)	D_{max} Dose difference (%)	R_{90} DTA (mm)	R_{50} DTA (mm)	RW_{50} difference (mm)
Standard Fields	105	6x6	0°	6	96.4	-2.0	0.1	0.7	1.6
(2%, 2 mm)				12	93.6	0.3	0.1	0.0	1.3
				18	94.4	-0.9	0.3	0.4	1.3
	100	10x10	0°	6	99.7	-0.6	0.1	0.3	0.5
				12	96.2	-0.8	0.6	0.3	1.1
				18	85.6	-1.7	1.2	0.0	1.5
Oblique Fields	105	6x6	25°	6	100.0	-0.7	0.8	0.1	0.9
(3%, 3 mm)				12	99.5	1.1	0.6	0.8	0.6
				18	97.3	1.2	1.2	0.2	0.8
			45°	6	90.4	-8.9	0.3	0.6	0.9
				12	94.9	-5.0	0.6	0.5	1.1
				18	97.1	-3.3	1.2	0.6	0.2
Circular Fields	100	6x6	2 cm	6	99.2	-0.2	0.4	0.3	0.6
(3%, 3 mm)			3 cm	6	98.4	4.0	0.6	0.1	0.5
				12	92.8	4.7	0.3	1.1	0.4
				18	98.1	2.5	0.0	0.1	0.8
			6 cm	12	99.6	-2.5	0.6	0.8	1.0
				18	87.6	2.2	0.0	1.3	0.4
Inhomogeneity	100	10x10	Rib/lung	6	99.1	-6.6	2.0	1.3	1.2
(3%, 3 mm)		6x6	Skull	6	98.1	2.1	0.0	0.3	0.0

DISCUSSION

5.1 Film method

This study has resulted in the development of a method for high resolution 2D film measurement in a portable water phantom. Electron beam parameters such as R_{90}, R_{50} and RW_{50} can be determined accurately with this method. If an ionisation chamber is used, the depth ionisation must be converted to depth dose as recommended by TRS 398 (IAEA, 2000). This conversion is required in electron beams because the water to air stopping-power ratios changes rapidly due to the differences in energy spectra with depth (IAEA, 2000). The conversion is not necessary with radiochromic films because the stopping power ratio between water and film is close to 1 and is less sensitive to changing electron spectrum.

The film measurement method described in this study has its benefits over conventional ionisation chambers and other types of array detectors. When compared to ionisation chambers, films offer a relatively higher 2-D spatial resolution and can be used in high dose gradient regions. Ionisation chambers have a fixed collecting volume for cylindrical chambers and fixed separation for plane parallel chambers which limits the resolution. When scanned with a flatbed scanner, films can provide sub-millimetre spatial resolution.

The presence of ionisation chambers during measurements perturbs the beam and to account for these perturbations, corrections like cavity, displacement, side wall and central electrode as described in TRS398 (IAEA, 2000) are required. Other factors that affect ionisation chamber measurements in electron beams include stem and cable effects, chamber polarity, ion recombination and chamber depth offset correction. Films on the other hand are very thin and cause minimal perturbation.

The charge collected in an ionisation chamber of any type depends upon the electron fluence in the active volume of the chamber. For normal incident beams, the electron fluence across the chamber is uniform with minimal perturbation. However, ionisation chambers tend to over-respond at depth for beams which are obliquely incident. This is due to increased scatter in the sidewall of the chamber into the active volume (Gerbi and Khan, 1997). This is illustrated in figure 5.1 which

shows the path of the electrons passing through the chamber side wall for an obliquely incident beam. For obliquely incident beam measurements with films, the over-response in dose is not seen. The difference in stopping power ratios between air and water for ionisation chambers is not relevant for film. The difference in stopping power between film and water is negligible therefore the over-response in dose is not seen in films.

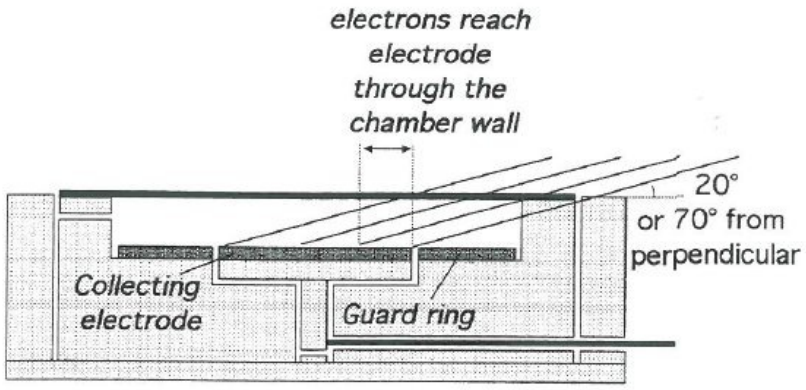

Figure 5.1 Diagram illustrating the electron path passing through the chamber side wall resulting in an increase in scatter contribution. Figure reproduced from (Ostwald, 1998).

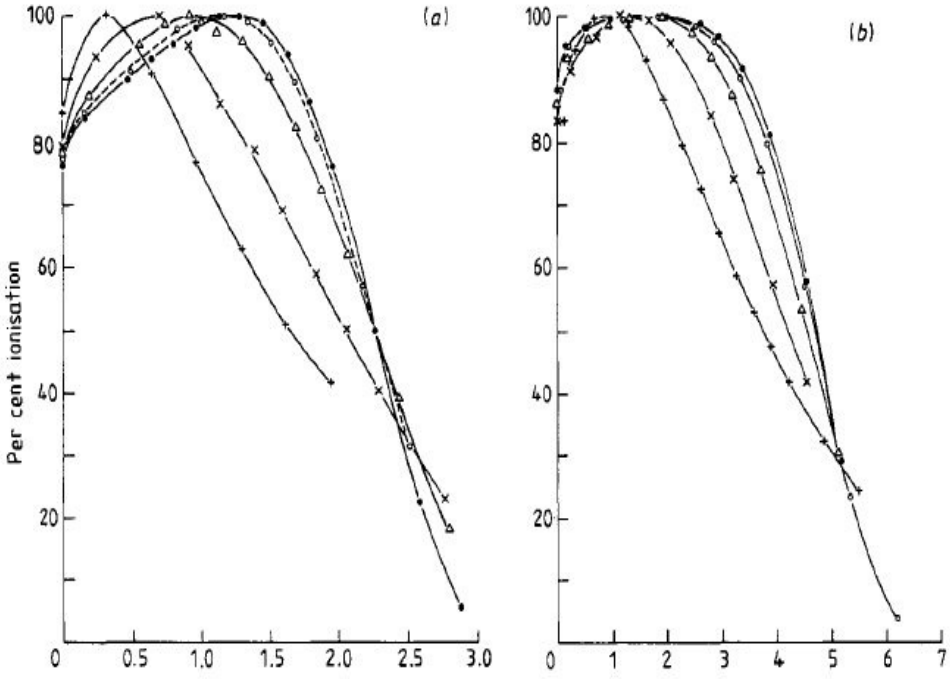

Figure 5.2 Depth ionisation curves for (a) 6 MeV and (b) 12 MeV for a 6 x 6 cm^2 field. Depth ionisation is measured along the central axis of the beam at 0, 15, 30, 45 and 60°. Figure reproduced from (Biggs, 1984).

The dose increase due to beam obliquity for small fields was investigated by Biggs (Biggs, 1984) using a thin window, parallel-plate ionisation chamber (SHM Nuclear Corporation, Sunnyvale, CA). Figure 5.2 shows measured depth ionisation curves taken along the beam axis for energies of 6 and 12 MeV at 0°, 15°, 30°, 45° and 60°. The plot displays an increase in surface dose as the beam angle increases for the 6 MeV curve. Similar differences were observed in this study. Figure 5.3 shows the EBT3 film measured depth dose curve for (a) 6MeV and (b) 12 MeV electron beam with 6 x 6 cm^2 field, 105cm SSD at beam angles of 0°, 25° and 45°. The depth dose curve is taken normal to the water surface and was normalised to D_{max} to provide a relative comparison to the data presented by Biggs (Biggs, 1984). Biggs' data shows an increase of less than 5% of the surface dose for the 6 MeV beam when the angle of incidence is varied from 0° to 60°, as measured with a parallel-plate ionisation chamber. However, for the 6 MeV beam measured in this study, surface doses measured by EBT3 film shows an increase of up to 9% when the angle of incidence is varied from 0 to 45°.

The problems with the use of parallel plate ionisation chambers for measuring surface doses for obliquely incident electron beams has been discussed above (Biggs, 1984; Ostwald and Kron, 1996). The film method used in this work is not subject the geometry issues that affect ionisation chambers and therefore may provide a better reference for validating XiO calculated data. Film has been shown to agree to within 3% with both ionisation chamber and XiO for normally incident beams and would be expected to measure dose for other geometries with the same degree accuracy.

Closer inspection of the data used in this work shows that XiO predicts an increase in surface dose of 11% as the beam angle increases from 0° to 45° for the 6 MeV beam. This agrees well with the increase in surface dose measured with film. However, the XiO surface doses are higher than film for the most oblique angles, as will be discussed in section 5.2.

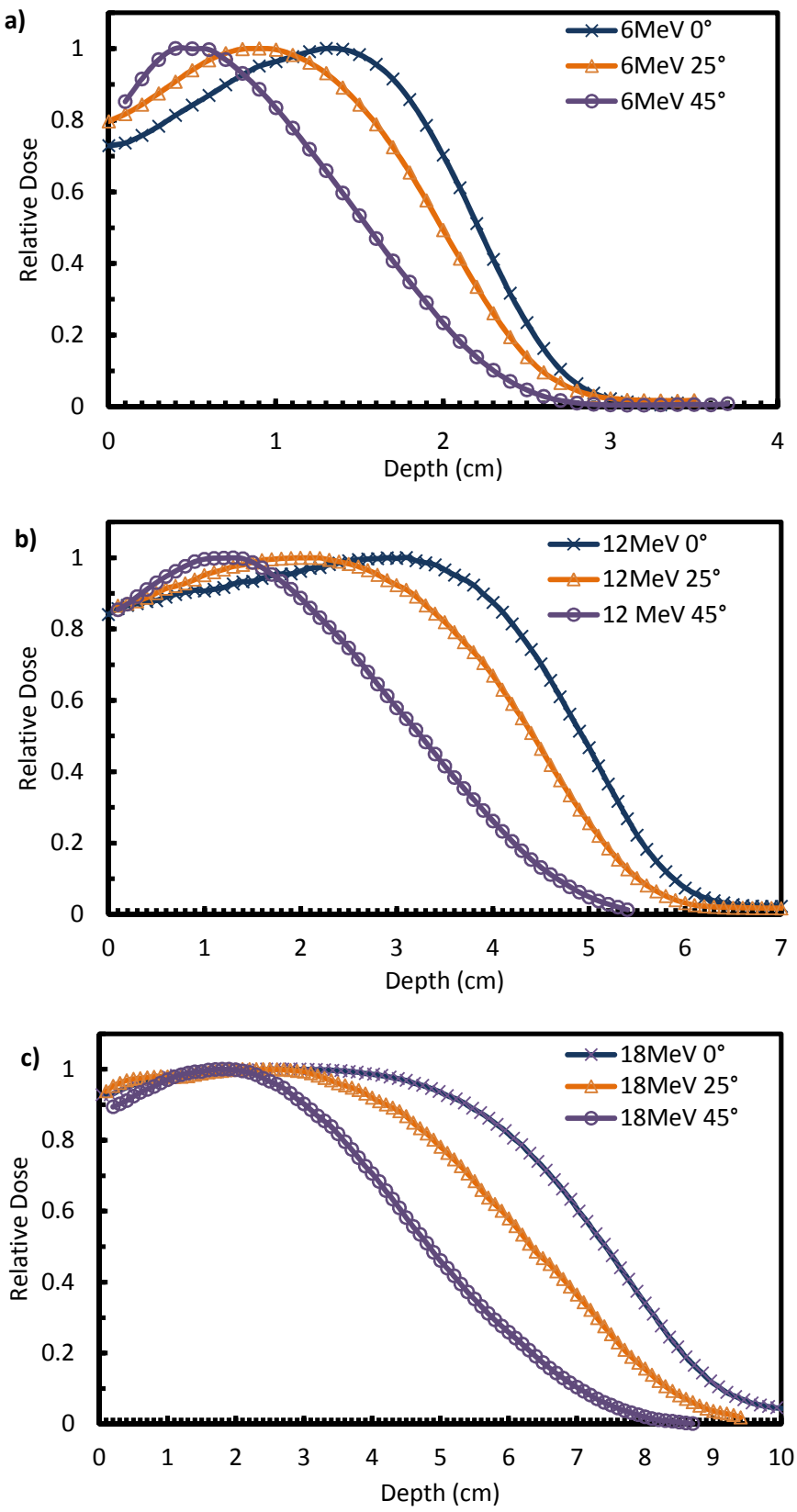

Figure 5.3 EBT3 film measured depth dose curve normalised to D_{max} for (a) 6 MeV, (b) 12 MeV and (c) 18 MeV electron beam with 6 x 6cm^2 field, 105cm SSD at beam angles of 0°, 25° and 45°.

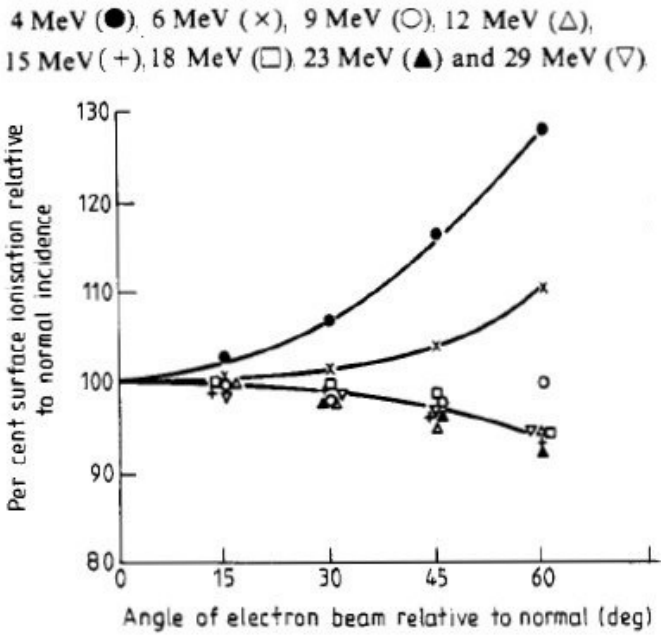

Figure 5.4 Variation of percent surface ionisation with angle of incidence of the electron beam. Figure reproduced from (Biggs, 1984).

Figure 5.4 shows the variation of surface ionisation with angle of incidence measured by Biggs (Biggs, 1984) using a parallel-plate ionisation chamber for different energies. The reported results state that the surface ionisation increase relatively as oblique incident angle increases for electron energies below 9 MeV. For 9 and 12 MeV, the difference is very minimal and at energies above 12 MeV, surface dose decreases slightly with increasing beam angle. The increase in surface dose with beam angle for the lower energies and slight decrease in surface dose at the higher energies is also seen with data measured by EBT3 film as shown in figure 5.3.

Conventional dosimetry equipment, such as Farmer ionisation chambers and plane-parallel chambers, are not suitable for use in small electron field measurements due to the loss of lateral electronic equilibrium and partial volume irradiation effects (Podgorsak, 2005). Radiation detectors introduced into small fields usually perturb the level of disequilibrium which affects the accuracy of dose determination (Das *et al.*, 2008b). With a large variety of radiation detectors, the choice of a suitable detector for small field dosimetry could be a challenging task. Although radiation detectors such as diodes, TLDs and MOSFETs have their advantages in small field dosimetry, radiochromic film could provide superior

advantages through its characteristics. Radiochromic film is able to provide the highest spatial resolution, absolute dosimetry and planar dose validation at the same time. Radiochromic films, Gafchromic® in particular, have previously been limited to relative dosimetry (McLaughlin *et al.*, 1994), but this study demonstrated that absolute dosimetry with the newer version of Gafchromic® EBT3 film is possible.

Although film dosimetry provides a huge advantage over conventional dosimetry equipment for non-standard field measurements, it has some weaknesses. Absolute dosimetry with radiochromic films requires post-exposure timing. To ensure accurate results, calibration and measurement films must be scanned at known times after exposure (Lewis, 2012). The orientation of the film must be noted especially for calibration films where the films are cut into smaller pieces. During the scanning process, the orientation of the film must be consistent for all scans. Differences of up to 9% are seen when comparing portrait and landscape scanning orientations (Andres *et al.*, 2010). In this work, the films' orientation was marked so that they can be consistently placed on the scanner bed. All films were placed in the centre of the scanner bed to minimise scanner non-uniformity effects.

This study demonstrated that accurate absolute dosimetry is possible with radiochromic film using a commercial flatbed scanner. However, care must be taken to minimise any inherent errors that may arise from either film and/or the scanner. Dose calibration films have to be done in conjunction with the measurement film to properly characterise the conversion from optical density to absolute dose. This is done by determining the linear accelerator output and the known dose is delivered to each calibration film. The absolute dose accuracy of radiochromic film when compared to ionisation chambers has been previously reported to be within 2% - 4% (Chung *et al.*, 2010). This study shows similar results where the agreement between EBT3 film and PPC05 absolute depth dose was within 3%.

The excellent agreement between film and ionisation chamber measurements for a number of standard fields, gives confidence in the accuracy of the film method. It has allowed the validation of the XiO eMC algorithm to be extended to include more complex field geometries. These include inhomogeneous geometries typical of those found in patients requiring electron therapy.

5.2 Comparison of EBT3 film and XiO eMC

In order to speed up the calculation times, eMC applies several simplifications and approximations to the electron transport algorithm. The main approximations are the reduction of the number of histories and average number of electron steps per history, the exclusion of photon contribution during simulation, the approximations for the Bremsstrahlung, Møller cross sections and treatment of delta rays, and the simplified multiple scattering distribution (Kawrakow *et al.*, 1996). Among the approximations made, the Bremsstrahlung approximations, the treatment of delta rays and the simplified multiple scattering could potentially explain observed differences between XiO calculated dose and film for the fields investigated in this work. In addition to the uncertainties in XiO, the uncertainties in film dosimetry such as the film response, changes to electron spectrum and some angular dependence of the film response could be a contributing factor to these observed differences.

The simplification of Bremsstrahlung photon modelling in the linear accelerator introduces errors in the calculation but at energies used for radiation therapy, the contribution of Bremsstrahlung to the dose deposited in the patient is small and only significant for higher energy beams in the low dose tail at large depths. There are low energy X-ray contaminations produced by the electron scattering foil in the linear accelerator that reach the patient surface and also contribute to dose in the patient. For an accurate dose calculation, a full simulation of every incident electron should be performed. However, this can be computationally time consuming, so approximations are made to speed up the process. One such approximation in XiO eMC is that the photon background is extracted from a measured dose distribution in a water phantom, and then it is added to the eMC calculated dose distributions as a constant contribution. This approximation is valid for standard beam field size and geometry, but with complex treatment geometries, the photon background contribution may vary and is not as accurate.

Delta rays are secondary electrons created by energy transfer to the atomic electron. In the eMC model, the production of delta rays is modelled using an approximation of the Møller cross section which utilises the cut-off energy, rejecting

delta rays below an energy threshold. In the build-up region, where the electron energy is at its highest, the assumption that delta rays deposit their dose where they are created has a small or negligible effect. This is apparent as the dose calculated by XiO near the surface agrees very well with film for normally incident beams.

Beyond D_{max}, the agreement between EBT3 film and XiO eMC was 2% or 2 mm for standard fields and 3% and 3 mm for the oblique, small and fields with inhomogeneities. Beyond Dmax, the central axis depth dose profiles show good agreement between measured and calculated doses of less than 3%/2 mm in all cases. The 2D isodose distributions show that the largest difference between measured and calculated dose is seen for the low isodose lines. This can be seen in figures 4.11, 4.13, 4.16, 4.17 and 4.18 where majority of the differences fall at the field edge. Of all the energies used in this study, 18 MeV was found to have the poorest agreement between EBT3 film and XiO eMC for the standard fields. Here differences of up to 3% are seen in the region between 3 and 5 cm depth, as shown in figure 4.10 (a). This data is shown again in figure 5.5 where it can be seen that the difference is within the measurement uncertainty of ±3% (2σ).

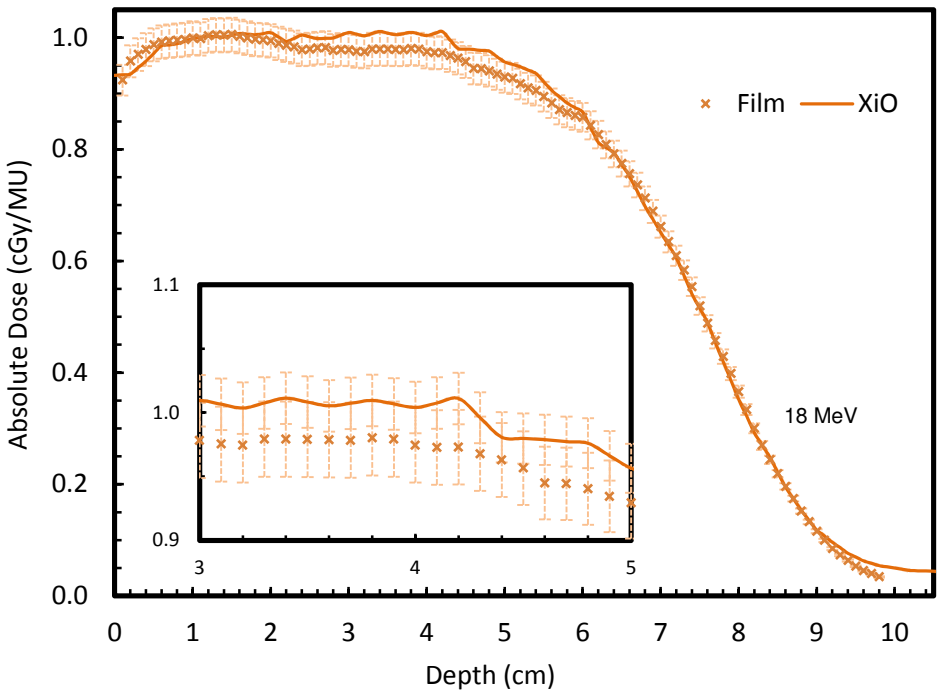

Figure 5.5 Comparison of EBT3 film and XiO eMC depth doses for 18 MeV electron beam for 10 x 10 cm^2 field, 100 cm SSD. The region between 3 and 5 cm depth is shown in the insert figure. Error bars are ±3% (2σ) for film and ±2% (2σ) for XiO.

In the dose difference maps, the blue regions indicate EBT3 film measurements are lower than XiO eMC and red regions indicate that EBT3 films are higher than XiO eMC. During the comparisons, an automatic registration was performed which was, if necessary, followed by a manual match of up to 1 mm, so that the highest gamma passing rate was achieved. If the red or blue regions appear on opposite sides of the measurement, this generally indicates that there may be an alignment error, shifts of 1 mm in the X direction was performed to ensure that the best match is obtained. The difference seen at the field edges is a result of the steepness of the field edge gradient and the SNC Patient software limitation which allows a minimum shift of ±1 mm and this also contributed to the lateral asymmetry. Nevertheless, the discrepancies between EBT3 film and XiO eMC are still within the acceptance criteria based on the IAEA TRS 430 report (IAEA, 2004).

For oblique fields, the DTA for measured and calculated central axis depth doses is less than 1.2 mm at depths beyond $D_{max.}$ The largest difference of 8.9% is seen in the build-up region for the 6 MeV 45° beam as shown in Figure 4.13 (b). Figure 5.6 shows the comparison of EBT3 film and XiO for this 6 MeV beam again but with error bars showing the uncertainty for both measured and calculated dose. Beyond 0.7 cm depth EBT3 film and XiO eMC agree to better than ±3 % i.e. within the expected uncertainties. However, differences of up to 8.9% are seen from the surface to 0.7 cm depth which are outside the expected uncertainties and may indicate a limitation of the XiO model.

For small fields, the DTA between measured and calculated central axis depth doses is less than 1 mm beyond D_{max}. For 12 and 18 MeV, differences of up to 5% are seen from the surface up to D_{max} for the 3 cm fields as shown in Figure 4.15. The difference in the first few millimetres is likely due to calculation grid size effects as the XiO dose is constant over this region. The difference from 0.3 cm up to D_{max} is due the limitations of XiO eMC modelling small field sizes, resulting from the use of pre-calculated kernels as discussed in Section 2.4.3. Because of these inaccuracies, the model has not been released for clinical use at field sizes less 6 cm diameter. For the 6 cm field, large differences are seen for 18 MeV near the surface as shown in Figure 4.14. Figure 5.7 shows this data again comparing XiO eMC and EBT3 film, with error bars showing the uncertainty for both measured and calculated dose. Beyond 1

cm depth, XiO eMC and EBT3 film agree to better than 3% i.e. within the expected uncertainties. However, larger differences are seen from the surface to 1.0 cm depth which are outside the expected uncertainties and may indicate a limitation of the XiO model.

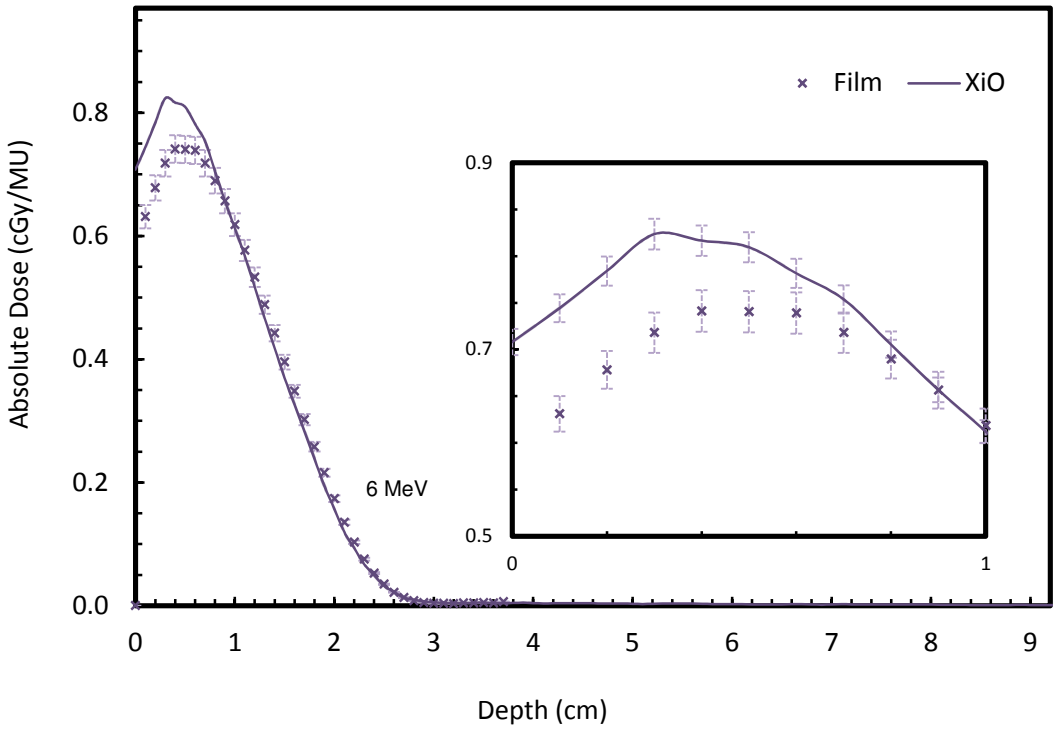

Figure 5.6 Comparison of film and XiO depth doses for 18 MeV electron beam with 6 x 6 cm^2 field, 105 cm SSD at 45° incident beam angle. The region from the surface to 1 cm depth is shown in the insert figure. Error bars are ±3% (2σ) for film and ±2% (2σ) for XiO.

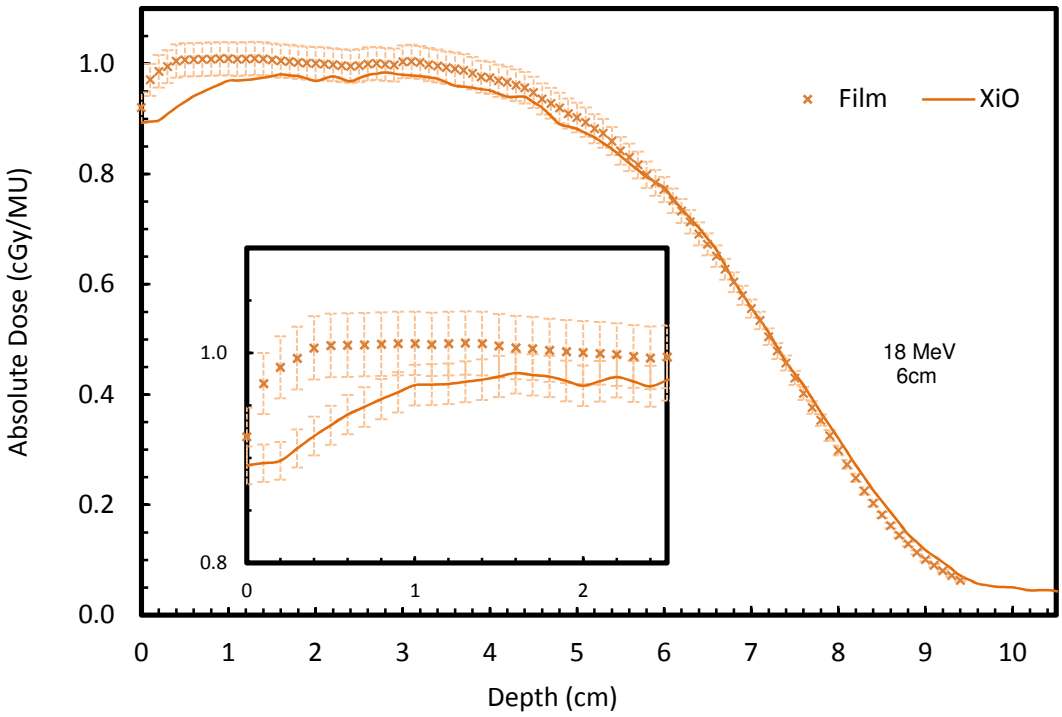

Figure 5.7 Comparison of film and XiO depth doses for 18 MeV electron beam using 6 cm diameter circular field at 100 cm SSD. The region between the surface and 2.5 cm depth is shown in the insert figure. Error bars are ±3% (2σ) for film and ±2% (2σ) for XiO.

The largest differences between EBT3 film and XiO eMC occur in the build-up region for both obliquely incident and small field beams. A possible explanation for this observation is that whilst the approximations used for multiple scattering are adequate to predict dose for standard beam configurations, they may be insufficient to accurately predict dose in more complex geometries. For obliquely incident beams, wide angle scatter would result in electrons "escaping" from the phantom. Failure to account for these "lost" electrons would mean that the dose deposited in the phantom would be overestimated by the model and the calculated dose would be expected to be higher than the measured dose. This is what was observed in this work. Similarly, for small, normal incidence beams, large angle scatter would contribute to dose closer to the surface of the phantom. If this is not modelled by XiO, the calculated dose in this region would be lower than the measured dose. XiO eMC uses precomputed EGSnrc (Kawrakow *et al.*, 2002) kernels to model the applicator cut-outs. The dose differences at shallow depth for both obliquely

incident and small field beams may be a contribution of approximations used in modelling scatter from the applicator cut-out.

Comparison of EBT3 film and ionisation chamber for standard fields showed excellent agreement, indicating that the EBT3 film response to the broadly varying electron spectrum has a minimal effect on the measurement. Following on from this, the film response would be expected to be similarly accurate for electron spectral variations in non-standard fields, and inhomogeneous media. Whereas the XiO eMC model needs to predict changes not only in electron energy, but also the effect of oblique incidence, large angle scatter and calculation of dose in heterogeneous media. As described above, Monte Carlo is subject to deficiencies when predicting dose in more complex geometries whereas EBT3 film only has to deal with the changing electron spectrum. Hence, the observed differences for non-standard fields and inhomogeneous media are more likely to represent XiO eMC underestimating the measured EBT3 film doses.

In figure 4.19, the central axis depth dose profile is up to 6.6% lower than XiO within the rib. This can also be seen in the isodose lines near central axis in the 2D dose comparison in Figure 4.20 (a). The agreement between measured and calculated isodose lines in the outer ribs is significantly better than at central axis. The reasons for this difference may be related to the difficulty in setting up the phantom and a lack of adhesion of the rib and lung phantom to the film at central axis. The depth dose profiles through the outer ribs show better agreement than at central axis. Figure 5.8 (a) shows the same comparison as figure 4.19 at 2 cm off beam central axis in the cross-plane direction. The film measurement here shows better agreement with XiO than on central axis. At 1 cm beyond the rib, in the lung, the difference between XiO eMC and EBT3 film is less than 1%. To compare film to XiO in the rib, the film derived dose-to-medium is compared to XiO dose-to-medium as outlined in section 3.10.4. This data is shown in Figure 5.8 (b) with error bars showing the uncertainty in both measured and calculated data. Differences of up 10% are seen within the rib which is outside the expected uncertainties even when taking into account the added uncertainty of the film dose conversion. This result may indicate a limitation in the XiO modelling or the approximations made in the film conversion. Or it may be a result of the difficulty in setting up the phantom. At 1

cm beyond the rib, in the lung, differences between film and XiO are within the expected uncertainties.

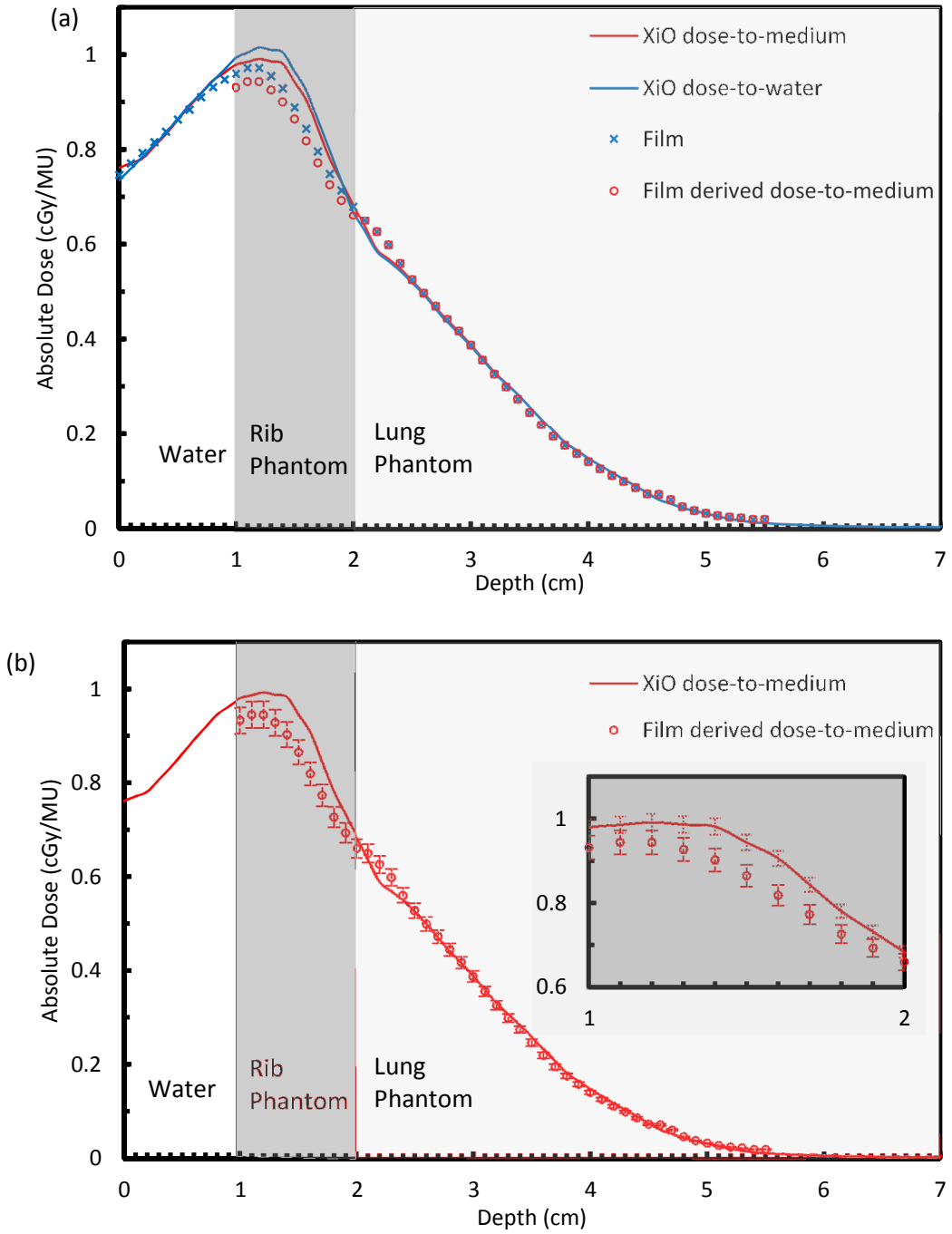

Figure 5.8 (a) Comparison of XiO dose-to-medium, XiO dose-to-water, film and film derived dose-to-medium depth doses in the rib and lung phantom for a 6 MeV 10 x 10 cm^2 field at 100 cm SSD. Depth dose profiles are taken at 2 cm off beam central axis. XiO dose-to-medium and film derived dose-to-medium comparison with error bars are shown in (b). The insert figure shows the region between 1 and 2 cm depth.

Figure 4.20 shows that dose to film agrees with XiO dose-to-water to within the measurement and calculation uncertainties for the skull phantom. Figures 4.19 and 4.20 both show that as density increases, a larger disparity is observed between the calculated dose-to-water and dose-to-medium. Calculated dose-to-medium is lower than dose-to-water for bone, as expected as mass collision stopping power for bone is less than equivalent density water (refer to section 5.3 for detailed explanation).

The XiO eMC dose-to-medium depth dose curve would be expected to have the same value as the XiO eMC dose-to-water depth dose in the water region before and beyond the interfaces of the skull phantom. As seen in figure 4.20, the XiO doses agree very closely in this region. The small discrepancy between the XiO dose-to-medium and dose-to-water curves near the proximal bone interface is likely due to the limited spatial resolution of the calculation grid size and interpolated values when plotting the data points. In figure 4.20, XiO eMC calculated doses were seen to be higher than the film measured and derived doses in the region beyond the skull. The reason for this discrepancy was investigated further.

This measurement was repeated recently on the new linear accelerator which is matched to the one used in this work. The recent measurement (figure 5.9 (a)) shows much better agreement between EBT3 film and XiO eMC in and beyond the region of the skull. In addition, the recent measurement shows the EBT3 film doses are higher than the XiO eMC doses in the Bremsstrahlung tail which is consistent with the results in figure 4.6 as discussed in 4.3.1 above. Figure 5.9 (b) shows only the film derived dose-to-medium and XiO dose-to-medium with error bars, and that the differences between EBT3 film and XiO eMC are within the expected uncertainties.

Initially only one measurement was done for each of the inhomogeneous set-ups, due to difficulty of positioning of the film and phantom materials in the water phantom. However, these measurements should have been repeated at the time to establish the reproducibility of the set-up.

The XiO eMC conversion from dose-to-medium to dose-to-water is not accurately calculated, as discussed below, so a meaningful comparison of XiO eMC with EBT3 film is not currently possible for the inhomogeneous set-ups.

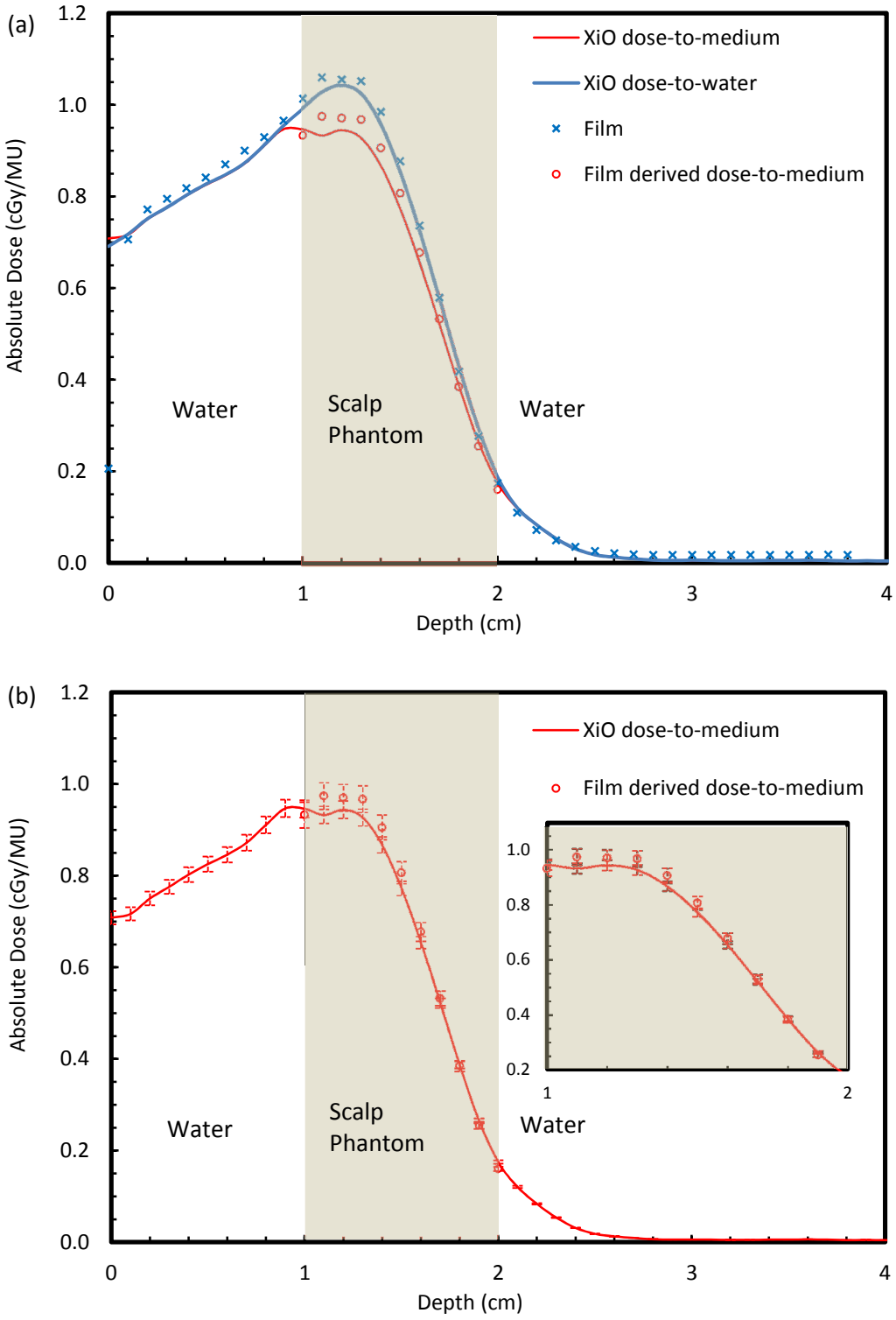

Figure 5.9 (a) Comparison of XiO dose-to-medium, XiO dose-to-water, film and film derived dose-to-medium depth doses in the skull phantom for a 6 MeV 10 x 10 cm^2 field at 100 cm SSD. Depth dose profiles are taken at beam central axis. XiO dose-to-medium and film derived dose-to-medium comparison with error bars are shown in (b). The insert figure shows the region between 1 and 2 cm depth.

5.3 Dose-to-water vs Dose-to-medium

Monte Carlo (MC) based treatment planning systems (TPS) are often based on simpler models than those implemented in general MC codes, but still provide a better dose distribution than those obtained using traditional analytical algorithms. Traditional dose calculation algorithms have always assumed that patient tissues can be treated as water-like, so tissues with high densities, such as bone, are modelled as high density water. Conversely, tissues such as lung are modelled as low density water. In XiO eMC, the density information is extracted from Computed Tomography (CT) scans by using the Hounsfield (HU) numbers to look up the electron density (ED) on a voxel by voxel basis.

The Monte Carlo dose calculation algorithm is based on the actual elemental composition of tissues, which takes in to account differences in absorption properties. A CT scan is used to determine electron densities of each voxel and assign material compositions to that voxel based on its HU. Unlike conventional dose calculation algorithms that use water with different electron density to account for the effect of patient heterogeneous anatomy, Monte Carlo calculates the energy deposition in different tissue types and reports dose to medium.

The AAPM Task Group 105 recommended that Monte Carlo results should allow conversion between dose-to-medium and dose-to-water, based on Bragg-Gray cavity theory (Chetty *et al.*, 2007). The reason for the conversion is to provide a comparison for MC algorithms with conventional dose-to-water algorithm (Siebers *et al.*, 2000). The conversion from dose-to-medium to dose-to-water or vice-versa, involves multiplying the energy deposited by primary and secondary electrons for each electron energy step by the ratio of restricted mass collision stopping powers of water to local medium for the current energy of the electron (Siebers *et al.*, 2000). Figure 5.10 shows the mass collision stopping power as a function of tissue density for different electron beam energies. The mass collisional stopping power ratios show that dose to bone is lower when calculated as dose to medium, and similarly dose to lung is slightly higher, than when calculated as dose to equivalent density water.

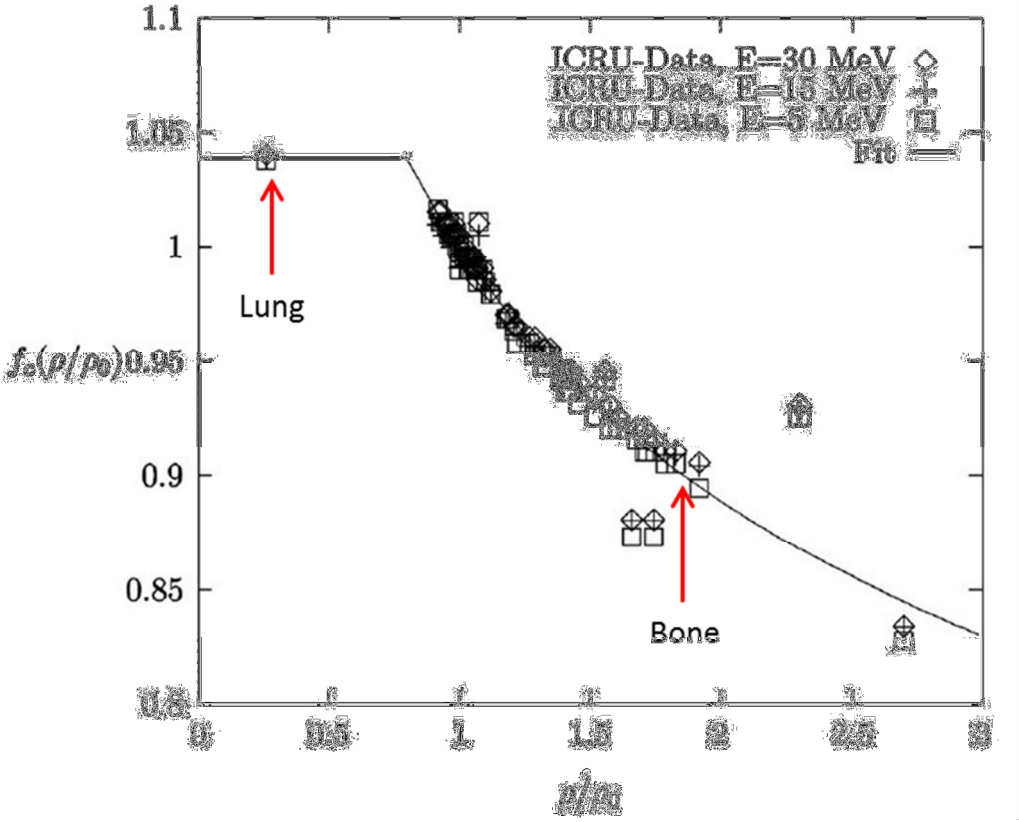

Figure 5.10 Mass collision stopping power divided by the mass collision stopping power of water as a function of density normalised to water. A comparison fit of the function to the ICRU data for body tissues for electron energies of 5, 15 and 30 MeV is shown. Figure reproduced from (Kawrakow *et al.*, 1996).

The conversion from dose-to-medium to dose-to-water has been investigated by a number of authors and the magnitude of the differences between dose-to-medium and converted dose-to-water in published reports are 1% for soft tissue and 10% for cortical bone (Siebers *et al.*, 2000). The differences between the two methods are shown in figure 4.22 and have clearly been shown in other publications (Dogan *et al.*, 2006; Knoos *et al.*, 2006; Ma *et al.*, 1999) which use the same method for converting from dose-to-medium to dose-to-water. Figure 5.11 shows a clinical example comparing dose-to-medium and dose-to-medium converted to dose-to-water for an electron chest-wall patient plan. The top image shows the dose distribution for dose-to-medium and middle image shows converted dose-to-water. The bottom image shows difference between dose-to-medium and converted dose-to-water. It becomes obvious that dose in bone appears to be lower (blue regions)

and dose in lung appears to be higher (red regions) when dose-to-medium is compared to converted dose-to-water.

The implementation of dose-to-medium may result in a change in clinical practice as the calculated dose per MU may differ significantly from that calculated using more traditional methods. Care must be taken to understand the impact of changing to a Monte Carlo algorithm and to quantify the potential impact on delivered dose to the patient. Any changes in clinical practice, i.e. treatment MU, must be discussed with radiation oncologists prior to treatment. Based on figure 5.11, if beam reference point in bone, and dose to medium is used to calculate dose, the monitor unit could be as much as 10% higher than what would have been used in traditional algorithms.

In this project, some comparisons were done in water where differences between dose-to-medium and dose-to-water are insignificant. However, when inhomogeneities are introduced, both dose-to-medium and converted dose-to-water calculations were used for comparison. There are two possible options to simulate both film and the inhomogeneous media. The first option is to create a phantom in XiO with a 280 μm thick slab with a relative electron density of 1 to simulate EBT3 film. However, it is not possible to calculate dose for a 280 μm grid size. The other option, which is used in this project, is to create a phantom with bone and surrounding water and calculate both dose-to-medium and dose-to-water for comparison with film, taking into account that dose-to-water overestimates the dose because of the limitation on converting dose-to-medium back to dose-to-water, as discussed below.

Current commercial Monte Carlo algorithms do not calculate the conversion from dose-to-medium to dose-to-water accurately. The algorithm does not re-calculate the dose distribution via Monte Carlo using water as the medium. The conversion employs methods that utilise stopping power ratios and ignore differences in fluence for water-like and tissue-like media (Andreo, 2015). To demonstrate the issue, a water phantom was created in XiO and the dose at D_{max} was calculated using a 10 x 10 cm^2 field at 100 cm SSD for 6, 12, and 18 MeV. The entire phantom was forced to varying electron density and re-calculated. The result, as can be seen in Figure 5.12, is the converted dose-to-water will be overestimated

for tissues with a density greater than water. In soft tissues, ignoring the fluence correction is not significant.

Given that Monte Carlo calculations are determining dose-to-medium, there are two possibilities when comparing film measurements to XiO eMC calculations. One can compare film-derived dose-to-medium directly with XiO dose-to-medium. For water phantom measurements, the medium is water and this comparison is valid. For other densities, which are translated by XiO into a selection of different media, this is more difficult as film is calibrated as dose-to-water (where heterogeneous media is simply scaled by density). The other alternative would be to convert dose-to-medium as calculated using Monte Carlo to dose-to-water. Most planning systems allow this. Unfortunately, this process is affected by significant uncertainties and a recent article by Andreo, P. (Andreo, 2015) discusses these in great depth. The journal ends with the recommendation that these conversions should be avoided. The present thesis follows this rationale and compares dose-to-medium calculated with the EBT3 film rather than to compare EBT3 film to XiO eMC's dose-to-water which has not been validated. The uncertainties with either method of conversion, XiO dose-to-medium to dose-to-water, or film dose-to-water to dose-to-medium, are both subject to significant approximations. It is understood that the conversion method used here is an approximation, but it is believed that it serves as a useful and somewhat qualitative validation of XiO eMC dose-to-medium in heterogeneous regions, in the absence of full Monte Carlo simulation.

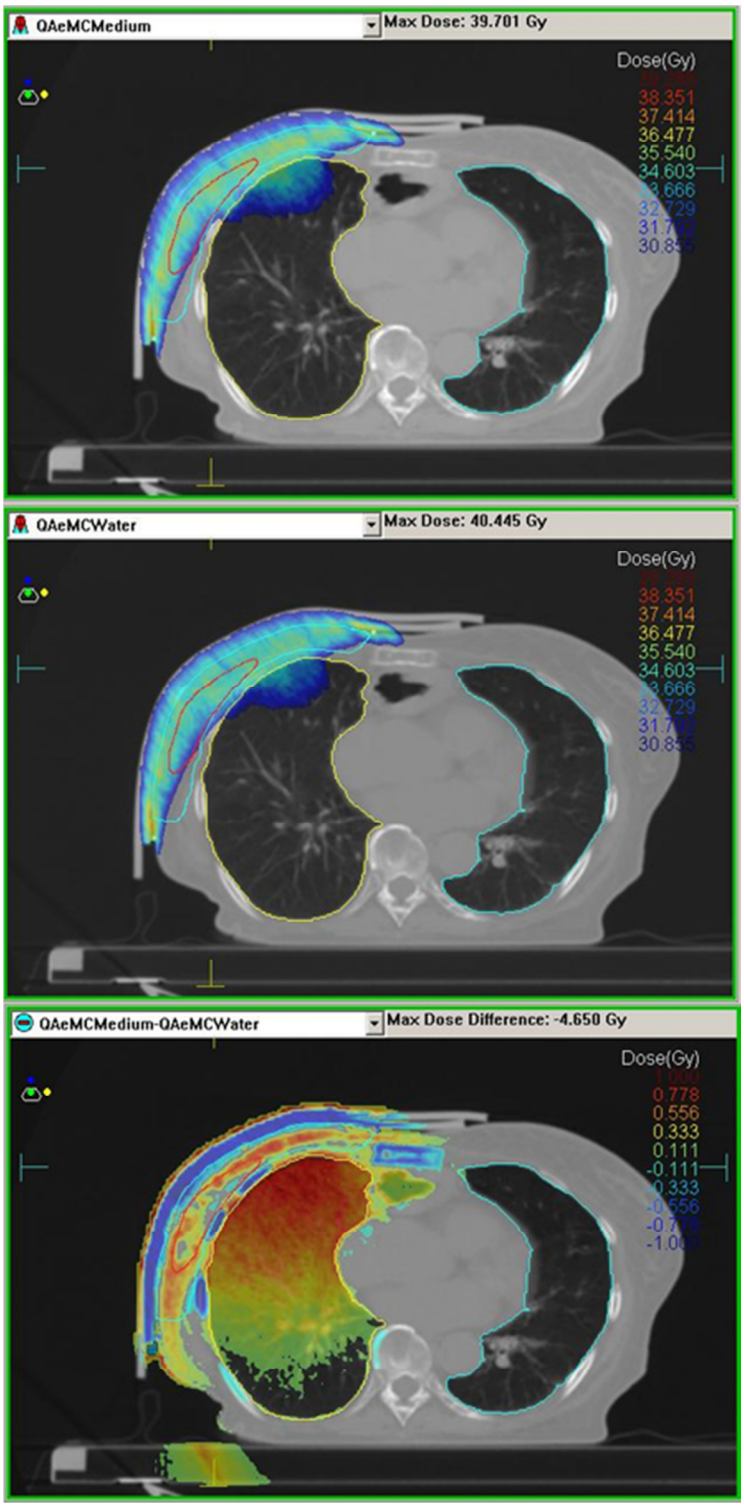

Figure 5.11 XiO eMC chest-wall plan showing 2D colourwash isodose distribution of calculated dose-to-medium (top) and converted dose-to-water (middle). The difference between dose-to-medium and dose-to-water is shown at the bottom image.

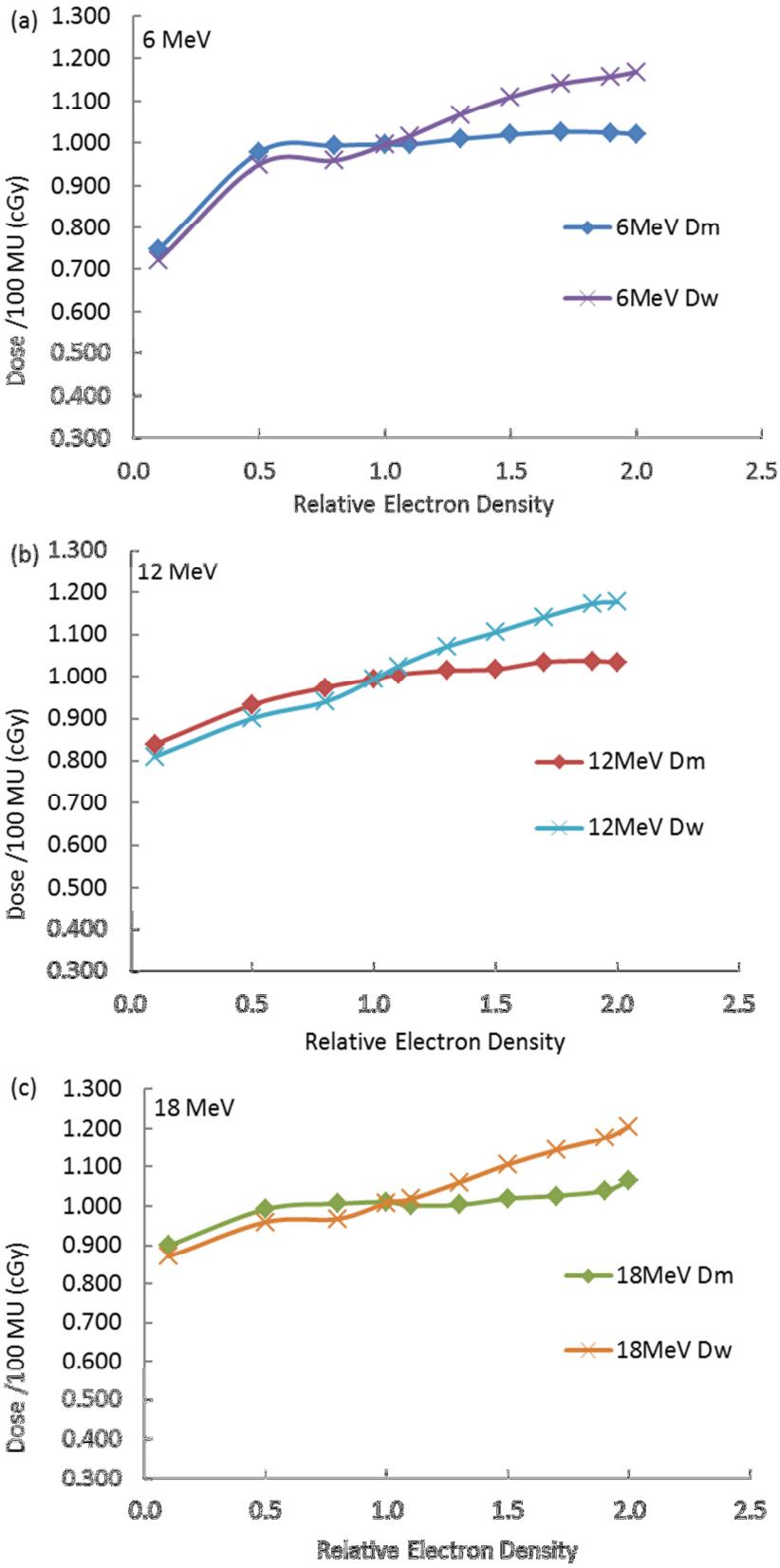

Figure 5.12 Comparison of dose per monitor unit with different electron densities between XiO dose-to-medium and XiO converted dose-to-water for a) 6MeV, b) 12 MeV and c) 18 MeV.

CONCLUSION

6.1 Summary

This thesis reports on the evaluation of XiO electron Monte Carlo dose calculation algorithm using radiochromic films vertically submerged in a water phantom. Measurements were performed for energies of 6, 12 and 18 MeV for various standard fields and complex treatment-like geometries such as beam obliquity, small field sizes and tissue inhomogeneities. The films were calibrated to provide absolute dose per monitor unit for direct comparison with XiO electron Monte Carlo dose distribution. The SNC Patient software was used to compare the overall 2D dose distribution and the differences were quantified by gamma analysis and DTA tools. The uncertainties associated with the film measurement method were analysed and the total uncertainty was found to be ±3% (2σ).

Beyond D_{max}, XiO eMC and EBT3 film agree within the calculation and measurement uncertainties i.e. ± 3% or ± 2 mm for all standard, oblique and circular fields for measurements in water. Differences of up to 9% occur close to the surface for the oblique and circular fields. For the inhomogeneous media, agreement between XiO eMC and EBT3 film was also within the calculation and measurement uncertainties for the water and lung like regions. Within the rib phantom, XiO eMC is up to 10% higher than EBT3 film. By contrast, the agreement between XiO eMC and EBT3 film within the denser skull phantom is within the expected uncertainties.

The limitations of film dosimetry have been discussed and the differences in dose between XiO eMC and EBT3 film could be due to deficiencies in either the eMC algorithm or in the film methods. However, it has been acknowledged by the manufacturer (Elekta) that it is very difficult to model the scatter of low energy electrons accurately. As low energy electrons will deposit their energy at shallow depths, we would therefore expect the accuracy of XiO eMC to be poorer at shallow depths. The EBT3 film results that show poorer agreement with XiO eMC at shallow depths are therefore not unexpected (J. Satterthwaite 2016, personal communication, 19 November) and are more likely to indicate a deficiency with XiO eMC rather than EBT3 film.

Validation of the XiO eMC algorithm for non-standard fields and inhomogeneous materials has been made possible by the development of a novel method for EBT3 film dosimetry. This study has resulted in the development of a method for high resolution 2D film measurements in a portable water phantom. The excellent agreement between film and ionisation chamber measurements for a number of standard field, gives confidence in the accuracy of the film method. It has allowed the validation of the XiO eMC algorithm to be extended to include more complex field geometries. These include inhomogeneous geometries typical of those found in patient requiring electron therapy. The method is not restricted to electron treatments and could be used for other situations where accurate, high resolution measurements are required, for example validation of small photon fields used for stereotactic and stereotactic ablative body radiotherapy (SABR) treatments.

6.2 Clinical recommendations

In this research, potential areas of concern are raised and clinically specific recommendations were made.

The increase in surface dose as a result of highly oblique beam angles may be clinically significant. The doses to the skin may be overestimated by the treatment planning system. However, treatments with highly oblique angles are rarely given to patients but may be unavoidable in regions with sharp skin contour changes.

XiO eMC calculations and measurements for small field sizes were investigated and eMC algorithm can accurately predict depth doses and isodose distributions for field sizes as small as 3.0 cm diameter for the lower beam energies and 6.0 cm for 12 MeV and above. If a diameter of less than 3 cm is used, output factor, depth dose and isodose distribution should be measured.

Due to the dose difference in the build-up region, the placement of the beam weight point should be taken into consideration. The beam weight point should be defined at the nominal D_{max} for each beam energy, away from air cavities, bone and metal interfaces, where the dose is more accurately defined.

This work also highlights the potential for significantly changing the actual dose delivered to patients if dose to medium is calculated rather than dose to water. Dose

to medium is inherently calculated by Monte Carlo and is believed by some (Liu *et al.*, 2002; Ma and Li, 2011) to have more clinical relevance than historically used dose-to-water. The conversion from dose-to-medium to dose-to-water is not accurate in most treatment planning systems (Andreo, 2015) and can introduce additional uncertainty. This however has very little impact for most water-like tissues such as muscle and lung.

The difference between dose to water and dose to medium calculations for the inhomogeneous geometries is an important issue. There is still debate in the medical physics community about which of these methods is most appropriate (Liu *et al.*, 2002; Ma and Li, 2011). Users need to be aware of these differences if dose-to-medium is used for patient calculations. For example, if the dose was prescribed to a point within the skull, the treatment MUs would be approximately 10% higher using dose to medium compared to dose to water. This could result in a clinically significant change to the dose being delivered to the patient. The most recent recommendations, ICRU 71 (ICRU, 2004), advise that dose variations within the target volume of an electron treatment should be less than ±10%.

6.3 Scope and limitations

The evaluation of XiO eMC calculations was performed using radiochromic film measurements for 6, 12, and 18 MeV beams. The calibration curves were generated in SNC Patient software using the red channel for doses ranging from 10 cGy to 600 cGy. Due to film variation between different boxes, the calibration curve is limited to the batch it is from. Each time a new EBT3 film box is used, a new calibration curve will have to be established.

The eMC module in XiO treatment planning system uses a beam model based on water tank measurements. The models were generated for a Varian 21iX linear accelerator. Simulations were performed for various beam irradiation setups in a water phantom. The eMC algorithm calculates dose in a voxel at a resolution of 0.2 x 0.2 x 0.2 cm^3. The mean relative statistical uncertainty of 1% was used during simulations. Ideally a 0.5% uncertainty was the preferred choice but the calculation times were extensive due to hardware limitations of the computers used.

The film absolute dosimetry method developed in this project show excellent agreement between eMC calculations and measurements. Most standard field measurements obtained a 3%/2 mm agreement with eMC calculations. Agreement of 3%/2 mm was seen between measurement and calculations for the 25° oblique fields. However, at the 45° oblique beam angle, some discrepancies are observed at the field edges and this could possibly be a result of slight differences between gantry angles during film irradiation. Similar differences at the field edges were observed for the small field sizes. This is a result of small differences in the field size diameter between measurement and calculation.

This project has showed that 2D dose plane validation is possible with non-standard measurement conditions including inhomogeneous media. Obtaining doses at the build-up region, surface and media interfaces are possible with this measurement method. Further investigation of the build-up region should be performed by a full Monte Carlo simulation as a baseline for comparison, to establish whether limitations of the XiO beam modelling are responsible for the differences between XiO eMC and EBT3 film in this region.

6.4 Future work

The method described in this work is not only limited to electron beam radiotherapy but could be extended to other treatment modalities such as Superficial X-Ray Therapy (SXRT) and Brachytherapy. SXRT uses kilovoltage x-ray beams in the range of 40 – 300 kV to treat superficial tumours. Due to the limitations of ionisation chambers, depth-dose curves for kilovoltage x-ray beams are difficult to measure especially near the surface. The film method described in this project could be used to measure depth dose curves in regions where ionisation chambers lack accuracy.

A preliminary study has been undertaken to compare planned and measured skin doses for breast radiation therapy using radiochromic film. Skin reaction is the primary acute toxicity experienced by patients undergoing breast radiation therapy. Based on this study, treatment planning systems do not provide an accurate estimate of surface dose delivery especially for curved structures. The aim of this study is to determine the accuracy in calculating skin doses for breast cancer patient

utilising an IMRT Head & Torso Freepoint phantom (CIRS, Norfolk, VA). The results of this study will be the subject of a future publication.

In preparation for the move of Peter MacCallum Cancer Centre to the new Victorian Comprehensive Cancer Centre in Parkville, the method described in this work was employed to re-commission the Varian Eclipse™ electron Monte Carlo algorithm for the new TrueBeam™ linear accelerators. A new and improved film water tank is currently being constructed and will be used for this commissioning project. The Parkville commissioning project provides an opportunity to compare film measurements with two different treatment planning systems (XiO and Eclipse).

REFERENCES

Andreo P 1991 Monte Carlo techniques in medical radiation physics *Physics in medicine and biology* **36** 861-920

Andreo P 2015 Dose to 'water-like' media or dose to tissue in MV photons radiotherapy treatment planning: still a matter of debate *Physics in medicine and biology* **60** 309-37

Andres C, del Castillo A, Tortosa R, Alonso D and Barquero R 2010 A comprehensive study of the Gafchromic EBT2 radiochromic film. A comparison with EBT *Medical physics* **37** 6271-8

Arjomandy B, Tailor R, Anand A, Sahoo N, Gillin M, Prado K and Vicic M 2010 Energy dependence and dose response of Gafchromic EBT2 film over a wide range of photon, electron, and proton beam energies *Medical physics* **37** 1942-7

Arjomandy B, Tailor R, Zhao L and Devic S 2012 EBT2 film as a depth-dose measurement tool for radiotherapy beams over a wide range of energies and modalities *Medical physics* **39** 912-21

Aubry J F, Bouchard H, Bessieres I and Lacroix F 2011 Validation of an electron Monte Carlo dose calculation algorithm in the presence of heterogeneities using EGSnrc and radiochromic film measurements *Journal of applied clinical medical physics / American College of Medical Physics* **12** 3392

Bielajew A F and Rogers D W 1992 A standard timing benchmark for EGS4 Monte Carlo calculations *Medical physics* **19** 303-4

Biggs P J 1984 The effect of beam angulation on central axis per cent depth dose for 4-29 MeV electrons *Physics in medicine and biology* **29** 1089-96

Butson E, Alnawaf H, Yu P K and Butson M 2011 Scanner uniformity improvements for radiochromic film analysis with matt reflectance backing *Australasian physical & engineering sciences in medicine / supported by the Australasian College of Physical Scientists in Medicine and the Australasian Association of Physical Sciences in Medicine* **34** 401-7

Casanova Borca V, Pasquino M, Russo G, Grosso P, Cante D, Sciacero P, Girelli G, La Porta M R and Tofani S 2013 Dosimetric characterization and use of GAFCHROMIC EBT3 film for IMRT dose verification *Journal of applied clinical medical physics / American College of Medical Physics* **14** 4111

Chetty I J, Curran B, Cygler J E, DeMarco J J, Ezzell G, Faddegon B A, Kawrakow I, Keall P J, Liu H, Ma C M, Rogers D W, Seuntjens J, Sheikh-Bagheri D and Siebers J V 2007 Report of the AAPM Task Group No. 105: Issues associated with clinical implementation of Monte Carlo-based photon and electron external beam treatment planning *Medical physics* **34** 4818-53

Chung H, Lynch B and Samant S 2010 High-precision GAFCHROMIC EBT film-based absolute clinical dosimetry using a standard flatbed scanner without the use of a scanner non-uniformity correction *Journal of applied clinical medical physics / American College of Medical Physics* **11** 3112

Cygler J E, Battista J J, Scrimger J W, Mah E and Antolak J 1987 Electron dose distributions in experimental phantoms: a comparison with 2D pencil beam calculations *Physics in medicine and biology* **32** 1073-86

Cygler J E, Daskalov G M, Chan G H and Ding G X 2004 Evaluation of the first commercial Monte Carlo dose calculation engine for electron beam treatment planning *Medical physics* **31** 142-53

Das I J, Cheng C W, Watts R J, Ahnesjo A, Gibbons J, Li X A, Lowenstein J, Mitra R K, Simon W E, Zhu T C and AAPM T G o t T P C o t 2008a Accelerator beam data commissioning equipment and procedures: report of the TG-106 of the Therapy Physics Committee of the AAPM *Medical physics* **35** 4186-215

Das I J, Ding G X and Ahnesjo A 2008b Small fields: nonequilibrium radiation dosimetry *Medical physics* **35** 206-15

Devic S, Seuntjens J, Hegyi G, Podgorsak E B, Soares C G, Kirov A S, Ali I, Williamson J F and Elizondo A 2004 Dosimetric properties of improved GafChromic films for seven different digitizers *Medical physics* **31** 2392-401

Devic S, Seuntjens J, Sham E, Podgorsak E B, Schmidtlein C R, Kirov A S and Soares C G 2005 Precise radiochromic film dosimetry using a flat-bed document scanner *Medical physics* **32** 2245-53

Devic S, Tomic N, Aldelaijan S, Deblois F, Seuntjens J, Chan M F and Lewis D 2012 Linearization of dose-response curve of the radiochromic film dosimetry system *Medical physics* **39** 4850-7

Devic S, Wang Y Z, Tomic N and Podgorsak E B 2006 Sensitivity of linear CCD array based film scanners used for film dosimetry *Medical physics* **33** 3993-6

Ding G X, Duggan D M, Coffey C W, Shokrani P and Cygler J E 2006 First macro Monte Carlo based commercial dose calculation module for electron beam treatment planning--new issues for clinical consideration *Physics in medicine and biology* **51** 2781-99

Ding G X and Rogers D W 1996 Mean energy, energy-range relationships and depth-scaling factors for clinical electron beams *Medical physics* **23** 361-76

Dogan N, Siebers J V and Keall P J 2006 Clinical comparison of head and neck and prostate IMRT plans using absorbed dose to medium and absorbed dose to water *Physics in medicine and biology* **51** 4967-80

Doucet R, Olivares M, DeBlois F, Podgorsak E B, Kawrakow I and Seuntjens J 2003 Comparison of measured and Monte Carlo calculated dose distributions in inhomogeneous phantoms in clinical electron beams *Physics in medicine and biology* **48** 2339-54

Edimo P, Kwato Njock M G and Vynckier S 2013 Validation of XiO Electron Monte Carlo-based calculations by measurements in a homogeneous phantom and by EGSnrc calculations in a heterogeneous phantom *Physica medica : PM : an international journal devoted to the applications of physics to medicine and biology : official journal of the Italian Association of Biomedical Physics* **29** 631-8

Ekstrand K E and Dixon R L 1982 The problem of obliquely incident beams in electron-beam treatment planning *Medical physics* **9** 276-8

ELEKTA 2010 Electron Monte Carlo Algorithm. In: *Volume III of III XiO Training Guide*

Ezzell G A, Burmeister J W, Dogan N, LoSasso T J, Mechalakos J G, Mihailidis D, Molineu A, Palta J R, Ramsey C R, Salter B J, Shi J, Xia P, Yue N J and Xiao Y 2009 IMRT commissioning: multiple institution planning and dosimetry comparisons, a report from AAPM Task Group 119 *Medical physics* **36** 5359-73

Ferreira B C, Lopes M C and Capela M 2009 Evaluation of an Epson flatbed scanner to read Gafchromic EBT films for radiation dosimetry *Physics in medicine and biology* **54** 1073-85
Fippel M 1999 Fast Monte Carlo dose calculation for photon beams based on the VMC electron algorithm *Medical physics* **26** 1466-75
Fraass B, Doppke K, Hunt M, Kutcher G, Starkschall G, Stern R and Van Dyke J 1998 American Association of Physicists in Medicine Radiation Therapy Committee Task Group 53: quality assurance for clinical radiotherapy treatment planning *Medical physics* **25** 1773-829
Gerbi B J, Antolak J A, Deibel F C, Followill D S, Herman M G, Higgins P D, Huq M S, Mihailidis D N, Yorke E D, Hogstrom K R and Khan F M 2009 Recommendations for clinical electron beam dosimetry: supplement to the recommendations of Task Group 25 *Medical physics* **36** 3239-79
Gerbi B J and Khan F M 1997 Plane-parallel ionization chamber response in the buildup region of obliquely incident photon beams *Medical physics* **24** 873-8
Hogstrom K R 1985 Evaluation of electron pencil beam dose calculation *Medical physics* **12** 554
Hogstrom K R, Mills M D and Almond P R 1981 Electron beam dose calculations *Physics in medicine and biology* **26** 445-59
Hu Y A, Song H, Chen Z, Zhou S and Yin F F 2008 Evaluation of an electron Monte Carlo dose calculation algorithm for electron beam *Journal of applied clinical medical physics / American College of Medical Physics* **9** 2720
Hussein M, Rowshanfarzad P, Ebert M A, Nisbet A and Clark C H 2013 A comparison of the gamma index analysis in various commercial IMRT/VMAT QA systems *Radiotherapy and oncology : journal of the European Society for Therapeutic Radiology and Oncology* **109** 370-6
IAEA 2000 Absorbed dose determination in external beam radiotherapy: an international code of practice for dosimetry based on standards of absorbed dose to water. In: *Technical Report Series No. 398,* (Vienna: International Atomic Energy Agency)
IAEA 2004 Commissioning and quality assurance of computerized planning systems for radiation treatment of cancer. In: *Technical Report Series No. 430,* (Vienna: International Atomic Energy Agency)
ICRU 1984a Radiation Dosimetry: Electron Beams with Energies Between 1 and 50 MeV. In: *ICRU-Report 35*: International Commission on Radiation Units and Measurements)
ICRU 1992 Photon, Electron, Proton and Neutron Interaction Data for Body Tissues. In: *ICRU-Report 46*: International Commission on Radiation Units and Measurements)
ICRU 2004 Prescribing, recording, and reporting electron beam therapy. In: *ICRU Report No. 71,* (USA: International Commission on Radiation Units and Measurements)
Jiang S B, Kapur A and Ma C M 2000 Electron beam modeling and commissioning for Monte Carlo treatment planning *Medical physics* **27** 180-91
Kawrakow I 1997 Improved modeling of multiple scattering in the Voxel Monte Carlo model *Medical physics* **24** 505-17

Kawrakow I, Fippel M and Friedrich K 1996 3D electron dose calculation using a Voxel based Monte Carlo algorithm (VMC) *Medical physics* **23** 445-57
Kawrakow I, Mainegra-Hing E, Rogers D W O, Tessier F and Walters B R B 2002 The EGSnrc Code System: Monte Carlo Simulation of Electron and Photon Transport. (Ottawa, Canada
Keall P J and Hoban P W 1996 Super-Monte Carlo: a 3-D electron beam dose calculation algorithm *Medical physics* **23** 2023-34
Khan F M 2003 *The Physics of Radiation Therapy*: Lippincott Williams & Wilkins)
Khan F M 2010 *The Physics of Radiation Therapy*: Lippincott Williams & Wilkins)
Khan F M, Deibel F C and Soleimani-Meigooni A 1985 Obliquity correction for electron beams *Medical physics* **12** 749-53
Khan F M, Doppke K P, Hogstrom K R, Kutcher G J, Nath R, Prasad S C, Purdy J A, Rozenfeld M and Werner B L 1991 Clinical electron-beam dosimetry: report of AAPM Radiation Therapy Committee Task Group No. 25 *Medical physics* **18** 73-109
Klein E E, Hanley J, Bayouth J, Yin F F, Simon W, Dresser S, Serago C, Aguirre F, Ma L, Arjomandy B, Liu C, Sandin C, Holmes T and Task Group A A o P i M 2009 Task Group 142 report: quality assurance of medical accelerators *Medical physics* **36** 4197-212
Klevenhagen S C 1993 *Physics and Dosimetry of Therapy Electron Beams* (Madison: Medical Physics Publishing)
Knoos T, Wieslander E, Cozzi L, Brink C, Fogliata A, Albers D, Nystrom H and Lassen S 2006 Comparison of dose calculation algorithms for treatment planning in external photon beam therapy for clinical situations *Physics in medicine and biology* **51** 5785-807
Krumeich F 2015 Elastic Scattering of Electrons by Atoms. (http://www.microscopy.ethz.ch/elast.htm: ETH Zurich)
Landau L 1944 On the Energy Loss of Fast Particles by Ionization *J.Phys. (USSR)* **8: 201**
Lewis D F 2012 Practical Guide to Radiochromic Film EBT2 and EBT3. Advanced Materials Group, Ashland Specialty Ingredients)
Liu H H, Keall P and Hendee W R 2002 Dm rather than Dw should be used in Monte Carlo treatment planning *Medical physics* **29** 922-4
Low D A, Harms W B, Mutic S and Purdy J A 1998 A technique for the quantitative evaluation of dose distributions *Medical physics* **25** 656-61
Ma C M, Faddegon B A, Rogers D W and Mackie T R 1997 Accurate characterization of Monte Carlo calculated electron beams for radiotherapy *Medical physics* **24** 401-16
Ma C M and Li J 2011 Dose specification for radiation therapy: dose to water or dose to medium? *Physics in medicine and biology* **56** 3073-89
Ma C M, Li J S, Pawlicki T, Jiang S B, Deng J, Lee M C, Koumrian T, Luxton M and Brain S 2002 A Monte Carlo dose calculation tool for radiotherapy treatment planning *Physics in medicine and biology* **47** 1671-89
Ma C M, Mok E, Kapur A, Pawlicki T, Findley D, Brain S, Forster K and Boyer A L 1999 Clinical implementation of a Monte Carlo treatment planning system *Medical physics* **26** 2133-43

Mah E, Antolak J, Scrimger J W and Battista J J 1989 Experimental evaluation of a 2D and 3D electron pencil beam algorithm *Physics in medicine and biology* **34** 1179

Mayles W P M, Lake R, McKenzie A, Macaulay E M, Morgan H M, Jordan T J and Powley S K 1999 Physics aspects of quality control in radiotherapy. In: *Report 81,* (York: IPEM)

McLaughlin W L, Soares C G, Sayeg J A, McCullough E C, Kline R W, Wu A and Maitz A H 1994 The use of a radiochromic detector for the determination of stereotactic radiosurgery dose characteristicsa) *Medical physics* **21** 379-88

Menegotti L, Delana A and Martignano A 2008 Radiochromic film dosimetry with flatbed scanners: a fast and accurate method for dose calibration and uniformity correction with single film exposure *Medical physics* **35** 3078-85

NCS 1996 Quality control of medical linear accelerators; current practice and minimum requirements. In: *NCS Report 9,* (Delft: Netherlands Commission on Radiation Dosimetry)

Nelson W R, Hirayama H and Rogers D W 1985 The EGS4 code system SLAC report 265 *Stanford Linear Accelerator Institute*

Neuenschwander H, Mackie T R and Reckwerdt P J 1995 MMC--a high-performance Monte Carlo code for electron beam treatment planning *Physics in medicine and biology* **40** 543-74

Niroomand-Rad A, Blackwell C R, Coursey B M, Gall K P, Galvin J M, McLaughlin W L, Meigooni A S, Nath R, Rodgers J E and Soares C G 1998 Radiochromic film dosimetry: recommendations of AAPM Radiation Therapy Committee Task Group 55. American Association of Physicists in Medicine *Medical physics* **25** 2093-115

O'Reilly D, Smit C J and du Plessis F C 2013 Extraction of electron beam dose parameters from EBT2 film data scored in a mini phantom *Australasian physical & engineering sciences in medicine / supported by the Australasian College of Physical Scientists in Medicine and the Australasian Association of Physical Sciences in Medicine*

Ostwald P M 1998 Determination of the Dose Distribution of Therapeutic Electrons at Interfaces. In: *Department of Physics*: University of Newcastle)

Ostwald P M and Kron T 1996 Surface dose measurements for highly oblique electron beams *Medical physics* **23** 1413-20

Paelinck L, De Neve W and De Wagter C 2007 Precautions and strategies in using a commercial flatbed scanner for radiochromic film dosimetry *Physics in medicine and biology* **52** 231-42

Paul J M, Koch R F and Philip P C 1985 AAPM Task Group 21 protocol: dosimetric evaluation *Medical physics* **12** 424-30

Podgorsak E B 2005 *Radiation Oncology Physics: A Handbook for Teachers and Students* (Vienna: IAEA)

Podgorsak E B 2010 *Radiation Physics for Medical Physicists*: Springer)

Poppinga D, Schoenfeld A A, Doerner K J, Blanck O, Harder D and Poppe B 2014 A new correction method serving to eliminate the parabola effect of flatbed scanners used in radiochromic film dosimetry *Medical physics* **41** 021707

Reinhardt S, Hillbrand M, Wilkens J J and Assmann W 2012 Comparison of Gafchromic EBT2 and EBT3 films for clinical photon and proton beams *Medical physics* **39** 5257-62

Reynaert N, van der Marck S, Schaart D, van der Zee W, Tomsej M, van Vliet-Vroegindeweij C, Jansen J, Coghe M, De Wagter C and Heijmen B 2006 Monte Carlo Treatment Planning: An Introduction *NEDERLANDSE COMMISSIE VOOR STRALINGSDOSIMETRIE* **Report 16 of the Netherlands Commission on Radiation Dosimetry**

Rogers D W 1991 The role of Monte Carlo simulation of electron transport in radiation dosimetry *International journal of radiation applications and instrumentation. Part A, Applied radiation and isotopes* **42** 965-74

Rogers D W and Mohan R 2000 Questions for comparison of clinical Monte Carlo codes. In: *The Use of Computers in Radiotherapy, XIIIth International Conference,* (Heidelberg: Springer-Verlag) pp 120-2

Saw C B, Loper A, Komanduri K, Combine T, Huq S and Scicutella C 2005 Determination of CT-to-density conversion relationship for image-based treatment planning systems *Medical dosimetry : official journal of the American Association of Medical Dosimetrists* **30** 145-8

Schoenfeld A A, Poppinga D, Harder D, Doerner K J and Poppe B 2014 The artefacts of radiochromic film dosimetry with flatbed scanners and their causation by light scattering from radiation-induced polymers *Physics in medicine and biology* **59** 3575-97

Seltzer S M 1988 An Overview of ETRAN Monte Carlo Methods Monte Carlo Transport of Electrons and Photons. (New York: Plenum) pp 153-82

Shiu A S and Hogstrom K R 1991 Pencil-beam redefinition algorithm for electron dose distributions *Medical physics* **18** 7-18

Siebers J V, Keall P J, Nahum A E and Mohan R 2000 Converting absorbed dose to medium to absorbed dose to water for Monte Carlo based photon beam dose calculations *Physics in medicine and biology* **45** 983-95

Sorriaux J, Kacperek A, Rossomme S, Lee J A, Bertrand D, Vynckier S and Sterpin E 2012 Evaluation of Gafchromic EBT3 films characteristics in therapy photon, electron and proton beams *Physica medica : PM : an international journal devoted to the applications of physics to medicine and biology : official journal of the Italian Association of Biomedical Physics*

Sorriaux J, Kacperek A, Rossomme S, Lee J A, Bertrand D, Vynckier S and Sterpin E 2013 Evaluation of Gafchromic(R) EBT3 films characteristics in therapy photon, electron and proton beams *Physica medica : PM : an international journal devoted to the applications of physics to medicine and biology : official journal of the Italian Association of Biomedical Physics* **29** 599-606

Stern R L, Heaton R, Fraser M W, Goddu S M, Kirby T H, Lam K L, Molineu A, Zhu T C and Group A T 2011 Verification of monitor unit calculations for non-IMRT clinical radiotherapy: report of AAPM Task Group 114 *Medical physics* **38** 504-30

Su F C, Liu Y, Stathakis S, Shi C, Esquivel C and Papanikolaou N 2007 Dosimetry characteristics of GAFCHROMIC EBT film responding to therapeutic electron beams *Applied radiation and isotopes : including data, instrumentation and methods for use in agriculture, industry and medicine* **65** 1187-92

Suchowerska N, Hoban P, Butson M, Davison A and Metcalfe P 2001 Directional dependence in film dosimetry: radiographic and radiochromic film *Physics in medicine and biology* **46** 1391-7

Ulin K and Sternick E S 1989 An isodose shift technique for obliquely incident electron beams *Medical physics* **16** 905-10

van Battum L J, Huizenga H, Verdaasdonk R M and Heukelom S 2016 How flatbed scanners upset accurate film dosimetry *Physics in medicine and biology* **61** 625-49

Van Dyk J, Barnett R B, Cygler J E and Shragge P C 1993 Commissioning and quality assurance of treatment planning computers *International journal of radiation oncology, biology, physics* **26** 261-73

Vandervoort E J, Tchistiakova E, La Russa D J and Cygler J E 2014 Evaluation of a new commercial Monte Carlo dose calculation algorithm for electron beams *Medical physics* **41** 021711

Venselaar J, Welleweerd H and Mijnheer B 2001 Tolerances for the accuracy of photon beam dose calculations of treatment planning systems *Radiotherapy and oncology : journal of the European Society for Therapeutic Radiology and Oncology* **60** 191-201

Williams J R and Thwaites D I 2000 *Radiotherapy Physics: in Practice* (Oxford: Oxford University Press)

Xu Z, Walsh S E, Telivala T P, Meek A G and Yang G 2009 Evaluation of the eclipse electron Monte Carlo dose calculation for small fields *Journal of applied clinical medical physics / American College of Medical Physics* **10** 2834

Zhang S, Liengsawangwong P, Lindsay P, Prado K, Sun T L, Steadham R, Wang X, Salehpour M and Gillin M 2009 Clinical implementation of electron energy changes of varian linear accelerators *Journal of applied clinical medical physics / American College of Medical Physics* **10** 2978

APPENDIX A

XiO® Electron Monte Carlo

Beam Data Collection List

The XiO Electron Monte Carlo algorithm supports current accelerator and applicator designs from Elekta, Siemens, and Varian. Users wishing to commission the algorithm for other treatment hardware should contact CMS physics support.

I. Collimation Geometry

A. For every combination of energy and applicator, record:
   1. the setting of the *X*-jaws;
   2. the setting of the *Y*-jaws.

B. For patient-specific applicator inserts (cutouts), record:
   1. the material composition and density (e.g., cerrobend, 9.76 g/cm^3);
   2. the thickness (e.g., 1.4 cm);
   3. the distance from the nominal source position of the accelerator to the lower surface of the cutout (e.g., 95.0 cm);
   4. whether the sides of the cutout aperture are parallel to the beam axis or divergent from the nominal source point of the accelerator.

II. Scanning Measurements in Water

The following water tank measurements must be performed independently for every electron energy.

A. Water tank measurements at 100 cm source-to-surface distance (SSD):
   1. For every applicator:
      a. Depth dose profile:[1] Scan upwards along the central axis to the water surface, beginning at a depth 5–10 cm beyond the practical range (R_p).[2,3] Use a depth increment of no more than 1 mm.
      b. Lateral profiles:[4] Scan along the *X*-axis or the *Y*-axis or both.[5] Choose a set of depths sufficient to represent the entire dose distribution; a suggested minimum set of depths is 0.5 cm, d_{max}, d_{90}, d_{80}, d_{50}, d_{20}, and $R_p + 2$ cm, where d_{max} is the depth of maximum dose and d_P is the depth, beyond d_{max},

---

[1] Prior to beam modeling, depth ionization curves must be converted to depth dose curves. Both the raw data and the processed data should be made available to the person modeling the beam.

[2] For accurate beam modeling, it is important that the water level be consistent and correct for all depth dose scans. One millimeter of evaporation from the surface of the water tank can appear as a 0.2-MeV increase in the energy of the beam.

[3] For a beam of nominal energy *N* MeV, $N \leq 10$, a suitable initial scan depth is $(N/2 + 5)$ cm (e.g., 8 cm for a 6-MeV beam); for $N \geq 10$, a suitable initial scan depth is *N* cm (e.g., 20 cm for a 20-MeV beam).

[4] Prior to beam modeling, lateral profiles should be first smoothed (using a gradient-preserving filter), then centered, then made symmetric. Both the raw data and the processed data should be made available to the person modeling the beam.

[5] If the radiation field is elongated in one direction (e.g., for a 6x10 cm applicator), gather a complete set of scans along both axes. If the field is square, gather a complete set of scans along one axis. Even for a square field, however, it is a good idea to scan at d_{max} along the perpendicular axis, to verify that the *X*- and *Y*-profiles are similar in shape.

ELEKTA
CMS SOFTWARE

LSSXIO0005 / 1.0 / 5/30/2009

at which the dose falls off to *P*% of maximum.[6] If possible, scan to 6–8 cm outside the field edge. Use a scan increment of no more than 2 mm.

2. For a mid-size applicator (14x14 cm or 15x15 cm) with a centered square cutout field measuring 5x5 cm at isocenter:[7]
   a. Depth dose profile, as in 1.a
   b. Lateral profiles, as in 1.b
3. For a field with no applicator in place and with the jaws open to 40x40 cm:[8]
   a. Depth dose profile, as in 1.a
   b. Lateral profiles, as in 1.b. Scan to a minimum distance of 21 cm from the central axis (1 cm beyond the edge of the radiation field).

B. Water tank measurements at extended SSD (110 to 115 cm):[9]
   1. For every applicator: Repeat steps A.1.a and A.1.b at extended SSD.
   2. For a mid-size applicator (14x14 cm or 15x15 cm) with a centered 5x5 cm cutout field: Repeat steps A.2.a and A.2.b at extended SSD.

III. Non-Scanning Measurements in Water

For each electron energy, choose a single reference depth (d_{ref}) at or near the depth of maximum dose for the large cones (14x14 cm and larger). Determine and record the ratio cGy/MU at d_{ref} for every field and SSD listed in section II.[10, 11]

[6] If d_{max} is 2 cm or greater, it is a good idea to include at least one additional scan in the depth range between 0.5 cm and d_{max}.

[7] For example, if the lower surface of the cutout is 95 cm from the nominal source point of the accelerator, then the cutout aperture should measure 4.75x4.75 cm at the bottom. The aperture size is always defined at the bottom, regardless of whether the aperture sides are parallel or divergent.

[8] If the jaws do not open to 40x40 cm, open them as far as possible, record the field size, and proceed with the measurements as described below.

[9] Choose the extended SSD based on practice in the clinic. An extended SSD of 110 cm is recommended if the same data set will be used to model the accelerator for the XiO Electron Pencil Beam algorithm.

[10] These ratios are typically determined by taking a series of relative output measurements under conditions of constant temperature and pressure, then referencing the relative measurements to the absolute calibration conditions. Both the raw data and the processed data should be made available to the person modeling the beam.

[11] It is necessary to measure and record the absolute cGy/MU ratio at some point on the central axis of every field. It is not strictly required that the measurement point be at the same depth (d_{ref}) for all fields. Note, however, that a stopping power correction must be applied when comparing ionization chamber measurements made at different depths.

APPENDIX B

XiO Electron Monte Carlo Beam Modeling Report

SETUP INFORMATION	
Case Identifier:	shrtc12e_10x10_econe_1000x
Nominal Applicator Size:	10.0 × 10.0 cm
Cutout Aperture Size:	N/A
Source-to-Surface Distance:	100.0 cm
OCR Scan Angle:	0.0 degrees (crossline)
MEASURED DATA	
Name of PDD file:	pr1000.100.100
Name of OCR file:	ocrr.1000.0.100.100
Measured data multiplied by:	1.0
COMPUTED DATA	
Name of Dose Plane File:	shrtc12e_10x10_econe_1000x.xz0
Computed Data is Multiplied by:	1.0
Median Filter Range:	3.0 mm
X-shift of Computed Data:	0.0 mm
Z-shift of Computed Data:	0.0 mm
ANALYSIS PARAMETERS	
Reporting Threshold:	5.0% of maximum dose
Type of Error Envelope:	Van Dyk
Max Dose Difference:	2.0% of maximum dose
Max Distance to Agreement:	2.0 mm
1-D NUMERICAL RESULTS	
RMS Difference:	0.8687 cGy
With respect to 1-D Error Envelope:	
Mean $\|\delta\|$:	0.2021
Points Failing:	0.81% (8 of 990 points)
With respect to 2-D Error Envelope:	
Mean $\|\delta\|$:	0.1529
Points Failing:	0.51% (5 of 990 points)
2-D NUMERICAL RESULTS	
RMS Difference:	1.3412 cGy
Mean $\|\delta\|$:	0.2194
Pixels Failing:	2.60% (74 of 2841 pixels)

The first few images below compare computed dose to measured dose for all user-supplied profiles, beginning with the depth dose profile. The final image shows a comparison of the computed 2-D dose distribution to a 2-D dose distribution interpolated from the measured profiles. The reported 2-D error is a combination of systematic error in the computed dose, statistical error in the computed dose, and interpolation error in the "measured" dose.